

Copyright

By

Robert Lee Calhoun, Jr.

2007

**The Dissertation Committee for Robert Lee Calhoun, Jr., certifies that this is the
approved version of the following dissertation:**

**Electrochemistry and Electrogenenerated Chemiluminescence of $\text{Ru}(\text{phen})_2\text{dppz}(\text{BF}_4)_2$
both Free and Intercalated into DNA**

Committee:

Allen J. Bard, Supervisor

Keith Stevenson

Richard Crooks

John McDevitt

Brian Korgel

**Electrochemistry and Electrogenated Chemiluminescence of Ru(phen)₂dppz(BF₄)₂
both Free and Intercalated into DNA**

by

Robert Lee Calhoun, Jr., B.S.; M.S.

Dissertation

Presented to the Faculty of the Graduate School of

The University of Texas at Austin

in Partial Fulfillment

of the Requirements

for the Degree of

Doctor of Philosophy

The University of Texas at Austin

May 2007

To Alice Ann

Acknowledgements

The author wishes to thank Dr. Allen J. Bard for his tireless patience and guidance for the past 4 years.

Thanks are also due to a host of others at the University of Texas who, through their knowledge, encouragement, and discussion made this publication possible. They are, Dr. Bob LeSeur, Dr. Masoud A. Mehrgardi, Simone Zanarini, The Anslyn Group, Dr. Frank Fan, and Dr. Norman Hackerman.

Outside the UT family are Dr. Jimmy Mills, Auburn University, Dr. Bill Durham, University of Arkansas, and Dr. Alice Ann Calhoun.

Finally, financial support has come from the United States Naval Academy, the Robert A. Welch Foundation, and the National Science Foundation.

My time at the University of Texas has been under the auspices of the Navy's Permanent Military Professor program.

**Electrochemistry and Electrogenenerated Chemiluminescence of Ru(phen)₂dppz(BF₄)₂
both Free and Intercalated into DNA**

Publication No. _____

Robert Lee Calhoun, Jr., Ph.D.

The University of Texas at Austin, 2007

Supervisor: Allen J. Bard

Ruthenium (II) bisphenanthroline dipyridophenazine, Ru(phen)₂dppz²⁺, exhibits first oxidation and reduction voltammetric responses which correlate well with the UV-vis spectroscopy and are typical to the compound class. The complex proves energy sufficient for electrogenerated chemiluminescence (ECL), and does so in aqueous media with co-reactants, also similar to its phenanthroline and bipyridine analogues. However, this behavior is curious since this compound's aqueous photoluminescence (PL) is undetectable but exhibits 'light switch' behavior upon intercalation into both calf thymus DNA and other polynucleotides in that the PL greatly increases. The ECL of both the free and intercalated complex is presented as well as scanning electrochemical

microscopy (SECM) studies to understand the complex's kinetic behavior in water upon oxidation. In an effort to understand the SECM results, the program COMSOL Multiphysics is used to model the EC' (catalytic) following reaction. The simulation results are validated using the ferrocyanide/cysteine system, which is known to exhibit the EC' mechanism.

Table of Contents

| | |
|--|----|
| Chapter 1 Introduction | 1 |
| <i>The Structure of the DNA Helix</i> | 1 |
| <i>Various Roles of Intercalators</i> | 3 |
| <i>Ru(phen)₂dppz²⁺ as an Intercalator</i> | 6 |
| <i>Metal Complex Based Electrogenerated Chemiluminescence (ECL)</i> | 8 |
| <i>ECL vs. PL</i> | 11 |
| <i>Scanning Electrochemical Microscopy (SECM)</i> | 12 |
| <i>Goals</i> | 15 |
| Chapter 2 Experimental | 20 |
| <i>Synthesis and Materials</i> | 20 |
| <i>Mass Spectrometry</i> | 23 |
| <i>UV-Vis and Fluorescence Measurements</i> | 23 |
| <i>Electrochemical Measurements</i> | 24 |
| <i>Light Measurements with DNA</i> | 24 |
| <i>Scanning Electrochemical Microscopy</i> | 26 |
| Chapter 3 Electrochemistry of Ru(phen) ₂ dppz ²⁺ | 29 |
| <i>Diffusion Coefficients</i> | 29 |
| <i>Digital Simulation</i> | 29 |
| <i>Behavior Beyond the First Reduction Wave</i> | 33 |
| <i>Determination of Standard Potentials</i> | 34 |
| <i>Analysis of Derived Potentials</i> | 36 |
| Chapter 4 Spectroscopy | 40 |
| <i>Free Complex</i> | 40 |
| <i>Correlation of Spectroscopy to Electrochemistry</i> | 44 |
| <i>DNA Intercalated Complex</i> | 47 |
| <i>Determination of the Binding Constant</i> | 48 |
| Chapter 5 ECL of the Unbound Complex | 54 |
| <i>Characteristics of the ECL</i> | 54 |
| <i>ECL and the Impurity</i> | 60 |
| <i>The Role of Tripropylamine</i> | 65 |
| <i>Oxalate Results</i> | 67 |
| Chapter 6 ECL with Polynucleotides | 70 |
| <i>Pulsed Amperometric Detection (PAD)</i> | 70 |
| <i>Use of EDTA Buffer</i> | 72 |
| <i>Fitting ECL with Polynucleotides Data</i> | 76 |
| Chapter 7 SECM | 81 |
| <i>Strategy</i> | 82 |
| <i>Normalization of the Current</i> | 85 |
| <i>Free Complex Results</i> | 86 |
| <i>Addition of DNA</i> | 89 |
| <i>Kinetic Estimates</i> | 92 |
| <i>Ru(III) and Ru(II) Binding Differences</i> | 94 |
| Chapter 8 Digital Simulation | 96 |

| | |
|--|-----|
| <i>Multiphysics</i> | 96 |
| <i>Boundary Conditions</i> | 98 |
| <i>Voltammetric Results</i> | 99 |
| <i>Approach Curves</i> | 102 |
| <i>EC' Modeling</i> | 102 |
| <i>Evaluating Multiphysics Using Known EC_i Data</i> | 111 |
| <i>Fitting of Experimental Data to EC' Predictions</i> | 113 |
| Chapter 9 Simulation Validation | 117 |
| <i>Voltammetry</i> | 118 |
| <i>Experimental and Predicted EC' Approach Curves</i> | 121 |
| Chapter 10 Conclusion..... | 125 |
| Appendix A..... | 129 |
| Appendix B | 130 |
| Bibliography | 138 |
| Vita..... | 142 |

Table of Figures

| | |
|--|----|
| Figure 1-1. At left, the components of DNA, some of the basic nomenclature, and how they bond together. At right is the resulting macromolecule that results when complementary bases (A and T shown) hydrogen bond. Reprinted with permission of the authors..... | 2 |
| Figure 1-2. Schematic depiction of the various excited states of $\text{Ru(phen)}_2\text{dppz}^{2+}$. The step at left is metal ligand charge transfer (MLCT) which occurs after absorption of the photon. Used with permission of the author..... | 7 |
| Figure 1-3. A schematic of major groove binding of $\text{Ru(phen)}_2\text{dppz}^{2+}$ | 9 |
| Figure 1-4. Positive and negative feedback approach curves for a tip $\text{RG} = 1.5$. Larger RG values make the curves turn less sharply in the area from $L = 2$ to $L = 1$ | 14 |
| Figure 1-5. A schematic representation of a SECM experiment is shown, outlining various parameters and possible events occurring in the course of an experiment. | 17 |
| Figure 3-1. Cyclic voltammetry at 300 mV/s of 1mM lab synthesized $\text{Ru(phen)}_2\text{dppz(BF}_4)_2$ (pink and orange traces) and commercially available $\text{Ru(phen)}_3\text{Cl}_2$ (blue trace). Experiment conducted in a helium drybox at a Pt electrode in acetonitrile with 0.1 M tetrabutylhexammoniumfluorophosphate (TBAPF_6) as the electrolyte. The Ag wire quasi-reference electrode (QRE) was calibrated at the end by adding trisphen and was found to be 7 mV positive of SCE. | 30 |
| Figure 3-2. A scan rate study in the helium drybox used to determine the diffusion coefficients for the oxidized and reduced specie in acetonitrile. The reduction side proved to be more precise though both sets of data extrapolate to near zero. | 31 |
| Figure 3-3. Examples of digital simulations of cyclic voltammetry at 1 V/s carried out using DigiElch. Close agreement with the experimental data verifies Nernstian behavior of the 1+ and 3+ states of the complex as well as the experimentally determined diffusion coefficients. Similar simulations were done for all scan rates shown in Figure 3-2 with only minor deviations at 10 V/s. | 32 |
| Figure 3-4. Aqueous, air saturated cyclic voltammetry at 100 mV/s and two different pH's. The poor solubility prevents seeing any meaningful electrochemistry. While an oxidation peak was visible using differential pulse voltammetry, the precision was poor in conducting a pulse width study..... | 37 |
| Figure 4-1. The UV-visible absorbance spectrum (top) of the lab synthesized $\text{Ru(phen)}_2\text{dppz(BF}_4)_2$ in 0.1M phosphate buffer, pH 7.5. The peaks at 375 and 440 nm were both explored to determine an extinction coefficient (bottom) with deviations of only 3%. | 41 |

| | |
|---|----|
| Figure 4-2. A comparison between equimolar solutions of the lab-synthesized compound in phosphate buffer and acetonitrile to demonstrate the light-switch behavior. An aqueous buffer solution of commercial trisphen at similar concentration is shown to highlight the red-shift that accompanies the substitution of the dppz ligand. | 42 |
| Figure 4-3. The fluorescence intensity at 617 nm over a range of concentrations of commercial reference ruthenium complexes and the lab-synthesized $\text{Ru(phen)}_2\text{dppz(BF}_4)_2$ all in phosphate buffer, pH 7.5. The extremely low emission from the dppz-modified complex is a small trisphen impurity that persisted despite a column chromatography purification step. It is interesting to note all exhibit significant intra-filter effects over large concentration changes. | 43 |
| Figure 4-4. $\text{Ru(phen)}_2\text{dppz}^{2+}$ emission in water arising from the addition of acetonitrile. Concentration is 100 μM and the peak is red-shifted from the pure acetonitrile peak. | 46 |
| Figure 4-5. An MS/MS experiment with a quadrupole ion trap mass spectrometer equipped with an electrospray ionization source. The spectra shown represent an average of 20 microscans. The bottom scan represents the initial fraction from the chromatography column and the top a fraction taken later. There was no clear separation during the purification step. All experiments come from complex precipitated from the second fraction. The mass to charge peak at 372.2 is the doubly charged, intact cation $\text{Ru(phen)}_2\text{dppz}^{2+}$. Note the very small amount of trisphen present. | 49 |
| Figure 4-6. To emphasize the low grade emission is from a trisphen impurity, calf thymus DNA is titrated into a solution of the lab-synthesized $\text{Ru(phen)}_2\text{dppz(BF}_4)_2$. Note how the addition of DNA causes the emission to shift from the trisphen characteristic wavelength to that of the dppz modified complex in acetonitrile. | 50 |
| Figure 4-7. Two parameter (binding constant and binding site size) fit of fluorescence data with two different polynucleotide types. | 52 |
| Figure 5-1. The ECL intensity of equimolar amounts of complex with two different co-reactants at a Pt disk electrode. Note the intensity with oxalate has been multiplied by 10. Scan rate was 200 mV/s. | 55 |
| Figure 5-2. Comparison of the ECL of common ruthenium based complexes and $\text{Ru(phen)}_2\text{dppz}^{2+}$. Reaction conditions were 0.1 M PBS and tripropylamine, pH 7.5, at a Pt disk electrode. | 56 |
| Figure 5-3. The ECL spectrum of $\text{Ru(phen)}_2\text{dppz(BF}_4)_2$ with tripropylamine as co-reactant in phosphate buffer, pH 7.5. The response with no tripropylamine (green) has been included as the blank. The noise spikes are gamma ray background. | 58 |

| | |
|---|----|
| Figure 5-4. A calibration curve of the peak ECL intensity of Ru(phen) ₂ dppz(BF ₄) ₂ in the indicated solvent conditions. The peak PMT current produced was taken from triplicate measurements (run in separate solutions) of a single anodic sweep as seen in Figure 5-1. The electrode was polished with 0.5 micron alumina slurry and sonicated in ethanol for 5 minutes between each run. The Pt electrode had an area of 0.013 cm ² | 59 |
| Figure 5-5. Two separate ECL experiments run under the same conditions. The blue trace is the lab-synthesized 0.1 mM Ru(phen) ₂ dppz(BF ₄) ₂ and the magenta trace is commercial trisphen ECL at 1% of the concentration. This shows conclusively that even a 1% trisphen impurity can only account for 10% of the light produced and thus the rest must come from the dppz modified complex. | 62 |
| Figure 5-6. The fluorescence of equimolar solutions of commercial trisphen in the indicated solvents. Interestingly, this complex emits more intensely in water..... | 63 |
| Figure 5-7. Fluorescence in water of various component related to the study. Note that merely adding tripropylamine to the solvent does not induce the light switch effect. | 64 |
| Figure 5-8. Stern-Volmer plot showing quenching of the fluorescence of Ru(phen) ₂ dppz(BF ₄) ₂ by tripropylamine. | 66 |
| Figure 6-1. Faradaic and photomultiplier response using pulsed amperometric detection (PAD) for ECL of Ru(phen) ₂ dppz(BF ₄) ₂ with tripropylamine. The blue trace is without polynucleotide present and the orange trace is after addition of 20-mer poly dA-dT. R = [base pairs] / [Ru]..... | 71 |
| Figure 6-2. A comparison of ECL intensity in an EDTA/Tris buffer compared to phosphate buffer, showing the effective quenching of ECL. Both are at pH 7.5. | 73 |
| Figure 6-3. Using the PAD profile to unravel the effects of the EDTA/Tris buffer on ECL performance. The blue trace is Ru(phen) ₂ dppz(BF ₄) ₂ with Tris only, the magenta trace after tripropylamine addition, and the green trace upon further addition of EDTA. | 75 |
| Figure 6-4. Two parameter fitting (ECL efficiency bound and free) of the ECL data with increasing base pair to Ru ratios. While the use of 20-mer improved the performance over calf thymus, neither show the light switch effect seen in PL experiments..... | 79 |
| Figure 7-1. Poor (top) and good (bottom) negative feedback approach curve using dissolved oxygen reduction as the tip-generated electrode reaction. The orange traces are the steady state tip current and the other traces are various theoretical responses based on the RG of the tip..... | 83 |

Figure 7-2. Uncorrected Pt substrate current at various L values for the 26 μm Pt tip. Conditions were air saturated, those indicated, and the substrate held at 0.35 V. Note the displacement of the baseline based on distance and the tailing off cathodic background current at the beginning of the sweep. Sweeps shown are the third of three consecutive and represent the reproducible data. 87

Figure 7-3. 0.115 mM $\text{Ru(phen)}_2\text{dppz}^{3+/2+}$ tip and substrate behaviour at a 26 μm diameter Pt UME tip above 1 cm glassy carbon (top) and 1mm Pt disk (bottom) substrates. The tip was brought to the distance indicated and additions of 20-mer dAdT were made resulting in the R values indicated. Background oxidative current was subtracted. 88

Figure 7-4. Substrate current response of a tip-generation, substrate collection (TGSC) experiment in both air saturated and degassed solutions. The current is normalized to the calculated tip current at far distances e.g. $i_{t,\infty}$ and denoted I'S. Both are similar results although the background current is less in the degassed experiment allowing positioning of the substrate potential closer to the E° to confirm the substrate is collecting the species of interest. 91

Figure 8-1. Graphical display of the concentration profile of Ru^{2+} during an SECM experiment. The legend at right connects color to concentration value. 97

Figure 8-2. A COMSOL Multiphysics® generated SECM cyclic voltammetry TGSC experiment. The blue trace is the tip CV for an electroactive species whose E° is 1.2 V and the magenta trace is the substrate response while poised at 1V. While the steady state current values generated agree well with previously established theory and practice, the ability to produce a smooth voltammogram varied with substrate-tip separation. ... 100

Figure 8-3. Simulated steady state tip and substrate current normalized to the tip current at far distance from the substrate ($i_{t,\infty}$). The points labeled 'Theory' come from Eq. 8-9. 101

Figure 8-4. Simulated tip and substrate current at 3 μm separation with the substrate potential set at 1.0 V. The tip current is catalytically enhanced at faster following reaction rate constants. Note the anodic current at the substrate due to the significant back reaction rate at the given potential (Eq. 8-6). At fast, following reaction rate constants (kfol), this current is also catalyzed and becomes the significant contributor to substrate response. Scan rate is 50 mV/s. 104

Figure 8-5. Simulated substrate responses at progressively smaller substrate potentials. Note the diminishing anodic pulse at early times. The tip current is shown for reference and shows the near unity collection efficiency at the 3 μm distance. Scan rate is 50 mV/s. 106

| | |
|--|-----|
| Figure 8-6. Simulated substrate and tip currents with the substrate potential moved negative to 0.6 V. While the steady state tip current magnitudes are unchanged from Figure 8-4, note the anodic pulse is absent. | 107 |
| Figure 8-7. Simulated tip current at large tip-substrate separation ($i_{t,\infty}$) showing the catalytic effect of the following reaction. | 108 |
| Figure 8-8. The effect of the following reaction on collection efficiency at the substrate. As the reaction proceeds at faster rates, less Ru^{3+} survives the trip to the substrate for conversion back to Ru^{2+} for a given distance. For each k_{fol} , there is a distance at which this is overcome, but it is closer as the rate increases. | 109 |
| Figure 8-9. Simulated normalized current vs. distance data for the tip and substrate for various k_{fol} . For comparison, the unperturbed, normalized tip current curve from the previous model is shown. | 110 |
| Figure 8-10. Comparison of current model to results for an $\text{E}_\text{r}\text{C}_\text{i}$ mechanism to previously published and validated by experimental data by Unwin et al., using Mirkin's dimensionless kinetic parameter κ | 112 |
| Figure 8-11. Fitting of experimental data to Multiphysics' pseudo first order EC' predictions of normalized substrate current. The data of the free complex agrees well with a rate constant of 10 s^{-1} . The data with 20-mer poly dA-dT added shows a rate constant for that process in excess of 100 s^{-1} | 114 |
| Figure 8-12. A comparison of Multiphysics' predictions for the substrate (top) and tip (bottom) responses for both EC' and EC_i (denoted 'ir') following reaction mechanisms. For the substrate, there is very little difference except at very small tip/substrate separations. | 115 |
| Figure 9-1. Cyclic voltammograms for the various components in the ferrocyanide/cysteine system in a 0.1 M borate, 0.5M KCl buffer at pH 10. Scan rate was 50 mV/s. | 119 |
| Figure 9-2. A comparison of Multiphysics' simulation of steady state UME tip current and experimental results. The experimental current values are an average of CV and chronoamperometry. | 120 |
| Figure 9-3. Typical tip and substrate responses using the ferro/ferrocyanide couple in a TGSC approach. Approach speed was $0.5 \mu\text{m/s}$ | 122 |
| Figure 9-4. Experimental and simulated approach data under the conditions indicated. The rate constant for the second order reaction used the published value at the indicated pH of $8000 \text{ M}^{-1}\text{s}^{-1}$ | 123 |

Chapter 1 Introduction

It is an understatement to say the ability for substances to interact directly and discreetly with the DNA helix has become a prized capability in the half century since DNA's structure was elucidated. One class of compounds that have this capability is known as intercalators¹ and has been shown to be an excellent tool for all manner of DNA study, modification, and inhibition. To understand how these compounds interact with DNA, a review of the helical structure is in order.

The Structure of the DNA Helix

The DNA helical structure is the result of three basic parts: the phosphate backbone, the attached five carbon sugars, and the opposing, nitrogen containing organic bases that are attached to each sugar. Figure 1-1 is a good illustration of the micro and macro structure.^{2,3} The right handed helix, also known as the B form, results because the bases are rotated out of the plane of the backbone when they hydrogen bond to the complementary base on the other side. A subtle feature to note from the graphic on the right side of Figure 1-1 is that the two backbones run in opposite directions to one another – termed antiparallel.⁴ This is why one backbone ends in a 5' hydroxyl group and the other with a 3' group. Also, quarternary features known as grooves occur as labeled on the far right side of Figure 1-1. What is not shown explicitly in the discussed graphics is the charge resident on the phosphate linkages. Since these linkages are based on PO_4^{2-} groups, the backbone is negatively charged along its entire length. This feature not only ensures the helix's solubility in water of what is otherwise a very large, organic

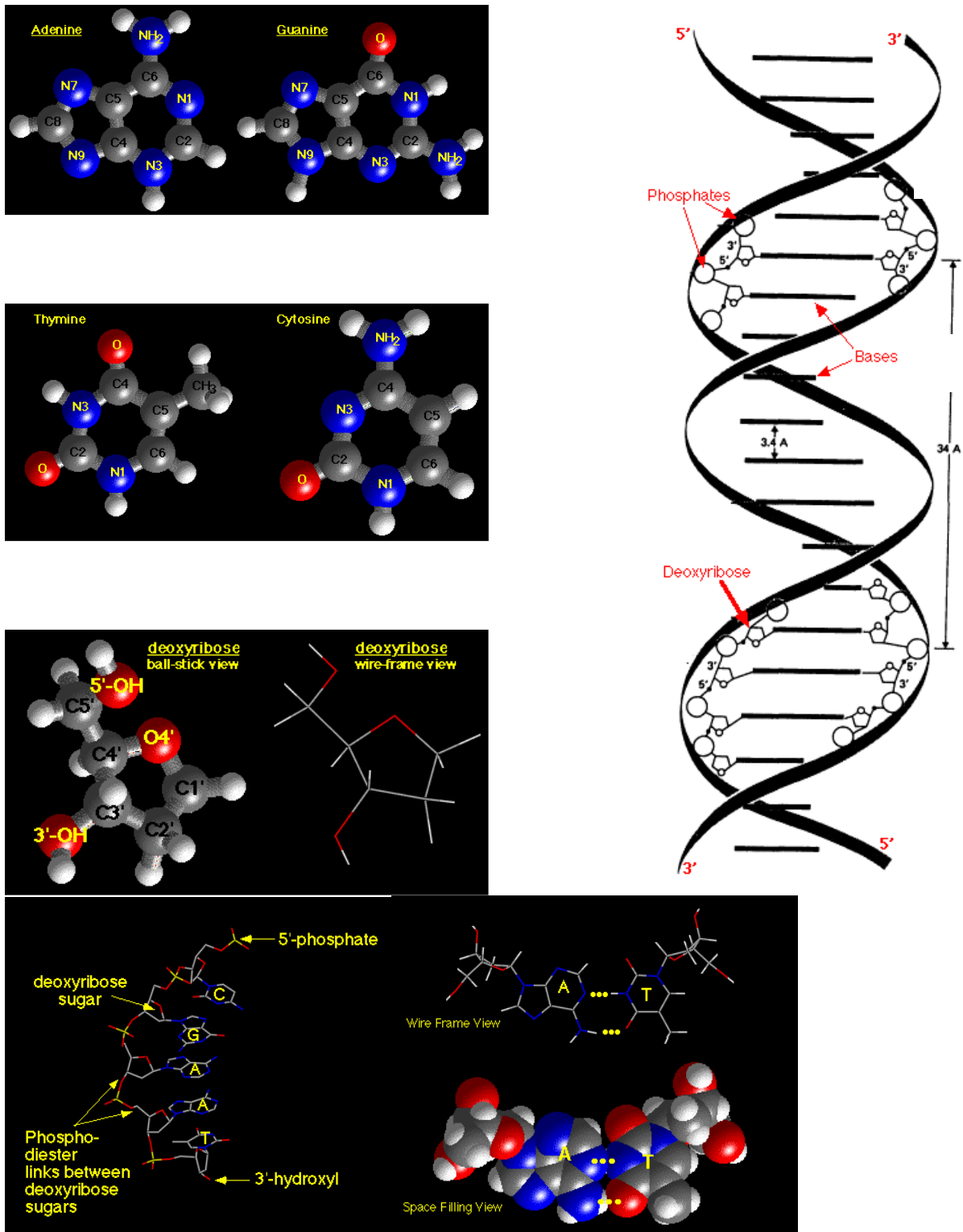


Figure 1-1. At left, the components of DNA, some of the basic nomenclature, and how they bond together. At right is the resulting macromolecule that results when complementary bases (A and T shown) hydrogen bond. Reprinted with permission of the authors.

molecule, but also has implications for the binding of intercalators as will be discussed later.

Various Roles of Intercalators

A cursory review of the literature finds that intercalator interactions fall into several broad categories. Intercalators have been used to study the charge transport mechanism up and down the DNA chain as well as reduction/oxidation chemistry with other molecules. Two examples are Mitoxantrone and a similar anthraquinone derivative which were used to study the effects of radiation damage to the DNA helix through base pair degradation.⁵ These molecules are both intercalators and electrophiles and thus will capture electrons ejected upon ionization by γ -rays and X-rays. The study used electron paramagnetic resonance (EPR) to see the extent of conversion of the intercalators to the anion radical. Similarly, an absorbance study used a ruthenium complex (only slightly different than that used in the current study) tethered to the end of a 20-mer oligomer which ensured intercalation into a specific part of the helix.⁶ Since the intercalator was an electron acceptor whose absorbance changed when reduced, and the base pair known to donate electrons upon irradiation resided at the other end of the oligomer, charge transport down the chain was measured.

Intercalators may also act as nucleases, cleaving DNA helices at specific sites. Fitzsimmons et al. designed such a nuclease using a rhodium-bipyridine (bpy) complex mated to a Zn bearing polypeptide. The Rh complex binds in the major groove, serving to put the peptide in close enough proximity so that it hydrolyzes the phosphate backbone of the helix.⁷ A more specific cleavage at abasic sites (sites where a heterocyclic base

has been removed from the helix) was obtained by Berthet et al. by using an acridine-based intercalator linked to an adenine through a polyamide chain.⁸ The intercalator brought the cleaving moiety in close proximity to the chain to do its work. The adenine provided the specificity by its inclusion into the abasic site.

Intercalators are also exploited in schemes to sense specific interactions with the helix. One such scheme is known as fluorescent intercalator displacement (FID), which also introduces the concept of a light switch. First, the intercalator compound's photoluminescence (PL) increases upon binding to DNA – the switch 'on' as indicated by emission of good intensity. But, upon addition of a different compound, a protein or drug whose binding to DNA is being investigated, the intercalator is displaced and the PL decreases significantly – the switch is 'off'. Charged heterocycles, such as ethidium bromide and thiazole orange, have been used in this manner.⁹ Another sensing scheme involves attaching thiolated single stranded (ss) DNA to a gold surface through the strong Au-S bond which formed a self assembled monolayer (SAM). The single strands are comprised of the complementary bases of a target single strand. Then a solution of various single strands (to include target strands) is incubated and an intercalator based on anthraquinone added.¹⁰ Only the target strands hybridize to the double helix and thus bind the intercalator. Since the intercalator is electroactive, peaks are seen upon cyclic voltammetry, the height of which indicates how much binding occurs. Glassy carbon electrodes have also been shown amenable to this scheme by forming a film using double stranded (ds) DNA and alginate.¹¹ In this case, ethidium bromide works as the intercalator-sensor since it is also electroactive.

Because of their binding ability to DNA, intercalators are studied with great intensity as anti-cancer agents, since the uncontrolled cell growth associated with these diseases requires instructions from the DNA. As has been shown, the specificity of the intercalator interactions with DNA helices make them obvious targets of study since they may inhibit these instructions required for abnormal cell growth by binding to helix. Brana et al. wrote a good review of various non-metal containing aromatic compounds emphasizing the planar nature of most intercalators.¹² They linked drug efficacy to the compound's ability to inhibit, "...molecular recognition and function of DNA binding proteins, (e.g., *polimerases* and *topoisomerases*).” While a more recent review demonstrates that much more is known after four years of research in terms of specific sites of DNA strand scission and covers a broader spectrum of compounds, the conclusion that drug interaction is closely linked to inhibition of “Topos” remains the same.¹³

Finally, intercalators may serve as flags or markers of DNA both in general or for specific base sites. The ethidium bromide PL light switch mechanism mentioned above has been shown to be more pronounced when used in the attachment of non thiol modified DNA to gold nanoparticles.¹⁴ Schatzschneider et al. used a tethered Rh-bpy complex that strongly (80%) preferred base pair mismatch sites¹⁵ and Petitjean et al. (from the same group) did similar work with a cis-Pt complex.¹⁶ Maruyama, et al., used an intercalating dye, SYBR Green I to accomplish the same thing since its PL changed significantly (20%) when intercalated into a mismatch site while residing inside a reverse micelle.¹⁷ In addition, a dimer of the ruthenium complex used in the present study was

used to show differing behaviors upon intercalation based on the chiral permutations of the two metal centers.¹⁸

Ru(phen)₂dppz²⁺ as an Intercalator

As previously discussed, some intercalators are platonic family metal-polypyridinal complexes, termed metallointercalators.¹⁹ One of the most studied over the past decade is the compound family Ru(L)₂dppz²⁺ (where L is phen = 1,10 phenanthroline, or bpy = bipyridine and dppz = dipyrldophenazine) because of its ability to intercalate with large binding constants ($> 10^6 \text{ M}^{-1}$) ensuring a strong interaction with the helix.²⁰ Further, the phenanthroline version of the compound exhibits a much more dramatic light switch behavior in water than described previously for ethidium bromide. Whereas ethidium bromide brightens and dims with an intensity difference on the order of 50-60%, Ru(phen)₂dppz²⁺ is an on/off effect. That is, the PL efficiency when intercalated is $> 10^3$ more than the free complex and has been well documented.²¹ This behavior is due to the interesting character of the excited state. When excited, there is the initial Frank-Condon state where an electron from the metal center is excited into ligand orbitals. This is dubbed metal-ligand charge transfer (MLCT – see Figure 1-2).²² However, the charge rapidly localizes on the phenazine nitrogens of the dppz ligand. It is this state that is responsible for the strong emission of light around 620 nm in non-aqueous solvents. In aqueous media, water hydrogen bonds to the relatively negative phenazine nitrogens and a new, very poorly emissive state is formed. However, when intercalated into DNA, the nitrogens are shielded from the solvent and emission around 620 nm, like that in non-aqueous solvents, occurs. Interestingly, there is an order

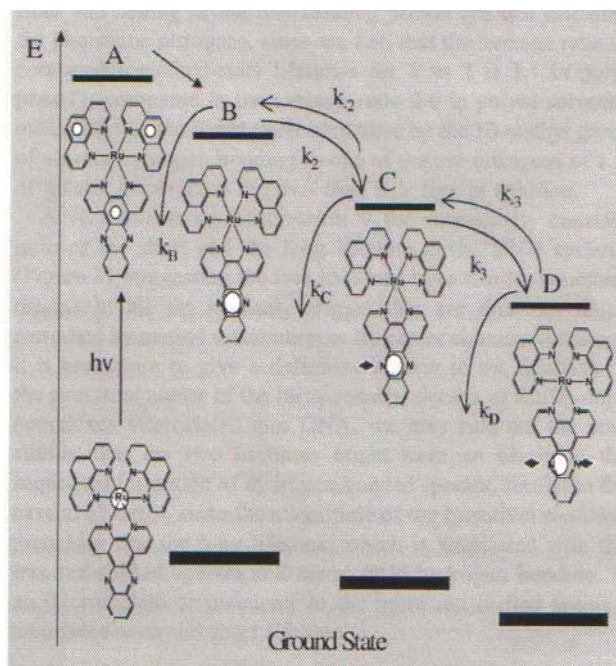


Figure 1-2. Schematic depiction of the various excited states of $\text{Ru}(\text{phen})_2\text{dppz}^{2+}$. The step at left is metal ligand charge transfer (MLCT) which occurs after absorption of the photon. Used with permission of the author.

of magnitude difference in the emission quantum yield between Δ and Λ enantiomers of the complex, even though both bind similarly by insertion between base pairs via the major groove of the B helix (see Figure 1-3). It is believed the Δ racemate are more densely intercalated onto the helix owing to the orientation of the exposed phen ligands relative to the twist of the helix. This offers more shielding from water thus producing more light.²³

Metal Complex Based Electrogenenerated Chemiluminescence (ECL)

For a longer period of time²⁴, studies of metal complexes in this ruthenium-polypyridine class have focused on their ability to undergo chemiluminescence in various solvents. This process occurs when specie chemically react in solution and light is a product. ECL is a variation on this theme in that at least one of the reacting species is generated by an electrode reaction. In short, ECL occurs upon the production of an excited state via a redox reaction of electrochemically produced specie as opposed to the use of light to make the excited state as is done in PL.²⁵ In the case of these Ru complexes, use of non-aqueous solvents allows access to the highly negative potentials required (past -1 V vs. the normal hydrogen electrode - NHE) to produce Ru(I). The experiment is thus able to produce light via fast production of the Ru(I) and Ru(III) species that react in the diffuse layer next to the electrode via the following reactions²⁶:



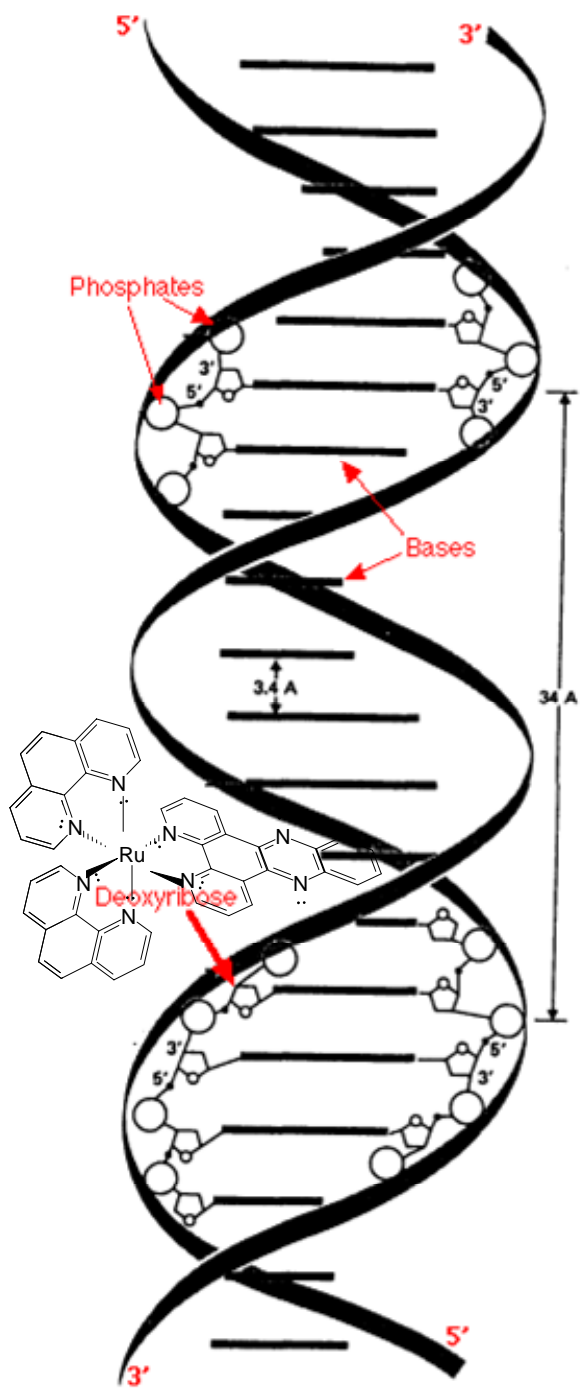


Figure 1-3. A schematic of major groove binding of $\text{Ru}(\text{phen})_2\text{dppz}^{2+}$.

where $\text{Ru(I)} \sim (\text{L})_2\text{Ru}^{\text{II}}(\text{L}^-)$, $\text{Ru(III)} \sim (\text{L})_3\text{Ru}^{\text{III}}$, and $\text{Ru(II)} \sim (\text{L})_3\text{Ru}^{\text{II}}$. $\text{Ru(II)}^* \sim (\text{L})_2\text{Ru}^{\text{III}}(\text{L}^-)$ which represents the excited state from which emission occurs. The difference between the potential where oxidation occurs (Eq.1-1) and the first reduction (Eq.1-2) represents enough energy to produce the excited state upon electron transfer and is known as the '*S-route*' since the emitting state has been found to be a singlet state.²⁷ It is also said to be energy sufficient. In thermodynamic terms, this reaction is written:

$$-\Delta G^0 = E^0(\text{Ru(III)}/\text{Ru(II)}) - E^0(\text{Ru(II)}/\text{Ru(I)}) \quad \text{Eq. 1-4}$$

and the reaction will make light if the change in free energy is greater than that of Ru(II)^* .²⁸ Early work using this method began with $\text{Ru}(\text{bpy})_3^{2+}$ ²⁹ and soon included a host of different ligands including phenanthroline.³⁰

It was discovered roughly 8 years later that ECL with ruthenium complexes could be generated in an aqueous environment as well, where only a small negative window (vs. NHE) is available due to reduction of water to hydrogen. This is accomplished by the addition of an electron donor for a species oxidized at the electrode to produce the excited state. For example, the use of oxalate follows this pathway³¹:



so the net is



where oxalate is termed the co-reactant. It seems counter-intuitive that a high energy electron donor could come from a process that is only oxidative but the CO_2 radical anion is a highly reducing species. It is the consequence of the carbon-carbon bond breaking in

oxalate.³² However, this system did not prove ideal for biological systems, since the quantum yield of the reaction proved sensitive to pH with its maximum yield around pH

5. Follow-on work by Danielson,³³ though, found that certain simple amines such as tripropylamine (TPrA) worked as well via the following pathway³⁴



which rapidly deprotonates via



to form the highly reducing amine radical which then produces the divalent excited state via:



This also proved to be pH dependent, but convenient for biological studies since the maximum efficiency occurs around pH 7.5.³⁵

ECL vs. PL

Use of the co-reactant technique has grown to an important, sought after, technology worth billions of dollars.³⁶ The popularity, and thus investment potential, centers around the analytical abilities of the technique to detect substances at very low concentrations thought to be possible bioterror agents such as anthrax and ricin. Other target substrates of interest for which ECL is used to carry out analyses include the detection of botulism, *E. coli*, salmonella, and various forms of staphylococcal. One of the key companies making commercial use of this technique has outlined these advantages.³⁷ The first advantage is the sensitivity of ECL over PL. The nature of the fluorescence experiment requires input of radiation at almost the same energy as the

target analytical signal. While most PL detectors are offset orthogonally to the input light in an effort to reduce the noise of the excitation light, there is still scattering by the solvent and analyte. This ensures a background that is much higher than that for ECL since it requires no light to produce the excited state. Secondly, since the background is less, the dynamic range is larger – in some cases a range of 10^4 . The final advantage is if there is no competing light generating reaction in the ECL experiment, only the amount of light needs to be measured, not the spectrum. This forgoes the need for complex and expensive optical components with their attendant signal losses as are required as in the PL experiment.

Scanning Electrochemical Microscopy (SECM)

It became apparent during the course of this work that, in addition to studying the ECL of the compound, kinetic information in water was desired to fully unravel $\text{Ru}(\text{phen})_2\text{dppz}^{2+}$ behavior. Scanning electrochemical microscopy (SECM) was determined to be best suited for this purpose. Basic SECM theory is outlined by Bard et al.³⁸ Briefly, a sharpened ultramicroelectrode tip is positioned above a substrate. This substrate may be either conducting or insulating, and the current response of the tip will vary in a predictable way based upon the variables of tip-substrate separation (termed d) and the ratio of the electroactive portion of the tip to its total diameter (known as RG). In order to generalize the results and make comparisons under various experimental conditions easier, the current vs. distance plot is usually rendered in dimensionless terms by normalizing the tip current to the current at far distances (dubbed $i_{t,\infty}$) and the tip/substrate separation to the electrode radius (a). Results showed that the current

response varied quite predictably with these parameters based on digital simulation. So predictably in fact, that the separation can be determined with submicron resolution if the tip positioners and software are sufficiently good.

If the substrate is non-conductive or insulating, as the tip approaches the order of a few tip radii, the electroactive species that generates current at the tip begins to be significantly blocked from diffusing to the tip and current decreases exponentially. This is termed *negative feedback*. A plot of the steady state current at the tip vs. the distance from the substrate for a single electrode is shown in Figure 1-4. If the substrate is conducting, its potential may be set to regenerate the initial species and a current feedback loop is formed that will make the current increase exponentially as it gets closer to the substrate. This is termed *positive feedback* and is also included in Figure 1-4. In general, the larger the RG, the less sharp the transition is between $L = 2$ to $L = 1$. Also, plots for insulating substrate experiments are more sensitive to RG than the response with a conducting substrate. A schematic of the experiment is shown in Figure 1-5.

Additionally, as alluded to previously, kinetic information is possible when analyzing the tip and substrate current responses at close distances. Bi et al. showed that a rate constant for a homogenous electron transfer reaction may be estimated based on the distance between the tip and the substrate.³⁹ This is done by sampling the substrate current at varying close distances and observing the collection efficiency (substrate current / tip current - CE) decrease at larger distances. The reduction in CE was due to the diffusing species being intercepted by the homogeneous reaction and therefore unable to be converted back at the substrate. Given that diffusion time may be estimated by $d^2/2D$ where D is the diffusion coefficient of the species in question, finding the nearest

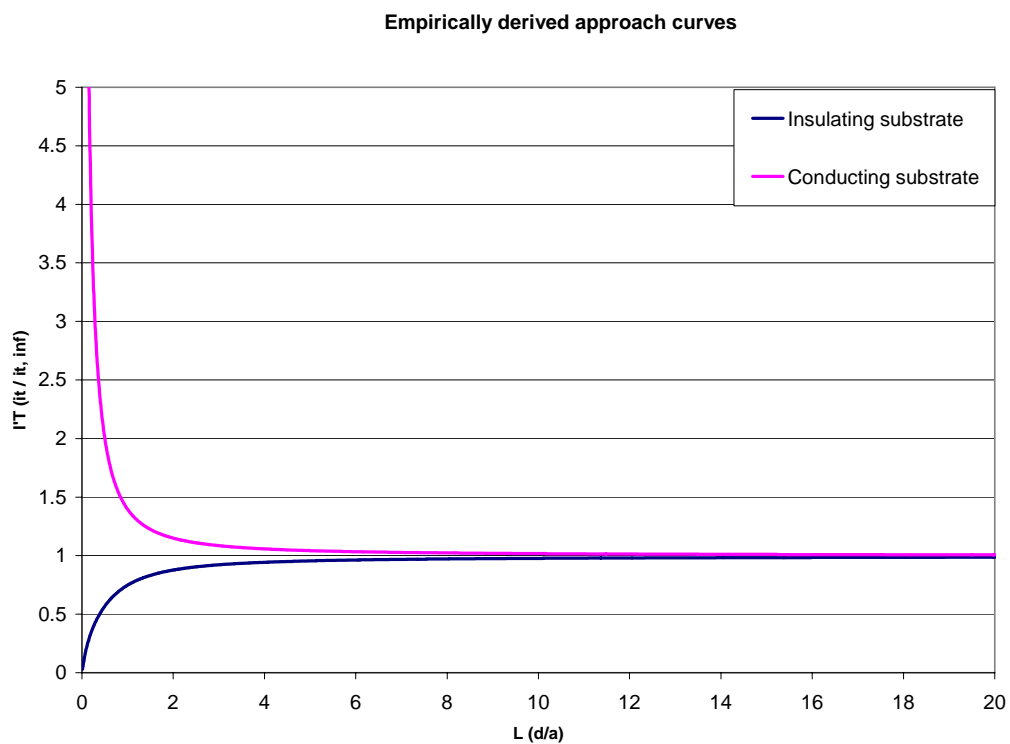


Figure 1-4. Positive and negative feedback approach curves for a tip $RG = 1.5$. Larger RG values make the curves turn less sharply in the area from $L = 2$ to $L = 1$.

distance where CE approached zero gave a time required to consume the diffusing species and, inversely, a rate constant for that reaction.

Finally, a systematic format for describing heterogeneous electron transfer reactions and homogeneous following chemical reactions was first published over 40 years ago by Testa and Reinmuth.⁴⁰ While there are eight permutations discussed in that work, the two that are germane to this work are the EC_i and the EC'. Here, E refers to the reversible electron transfer reaction that occurs at the electrode and C describes a following chemical reaction in solution. In the former, the subscript denotes that this step is irreversible. Thus,



followed by



The superscript in the second case (said 'EC prime') denotes this step is catalytic in that the original electroactive species is regenerated. Thus, after Eq. 1-12,



Goals

Thus, in Ru(phen)₂dppz²⁺, we find a proven light switch intercalator that should also undergo ECL due to its ruthenium polypyridinal composition. However, to date, very little electrochemical data and no ECL data have been published. Work done with the similar, though homoleptic, compounds of Os(bpy)₃²⁺ and Ru(phen)₃²⁺ revealed decreasing ECL intensity as DNA is added⁴¹ due to the reduced diffusion coefficient of the complex when intercalated. Our hope was that the large increase in luminescent

efficiency upon intercalation of $\text{Ru}(\text{phen})_2\text{dppz}^{2+}$ would overcome the diffusion effect and thus give an ECL light switch. Therefore, we sought to unravel the complex's chemiluminescent, electrochemical, and kinetic behavior both alone and intercalated into DNA.

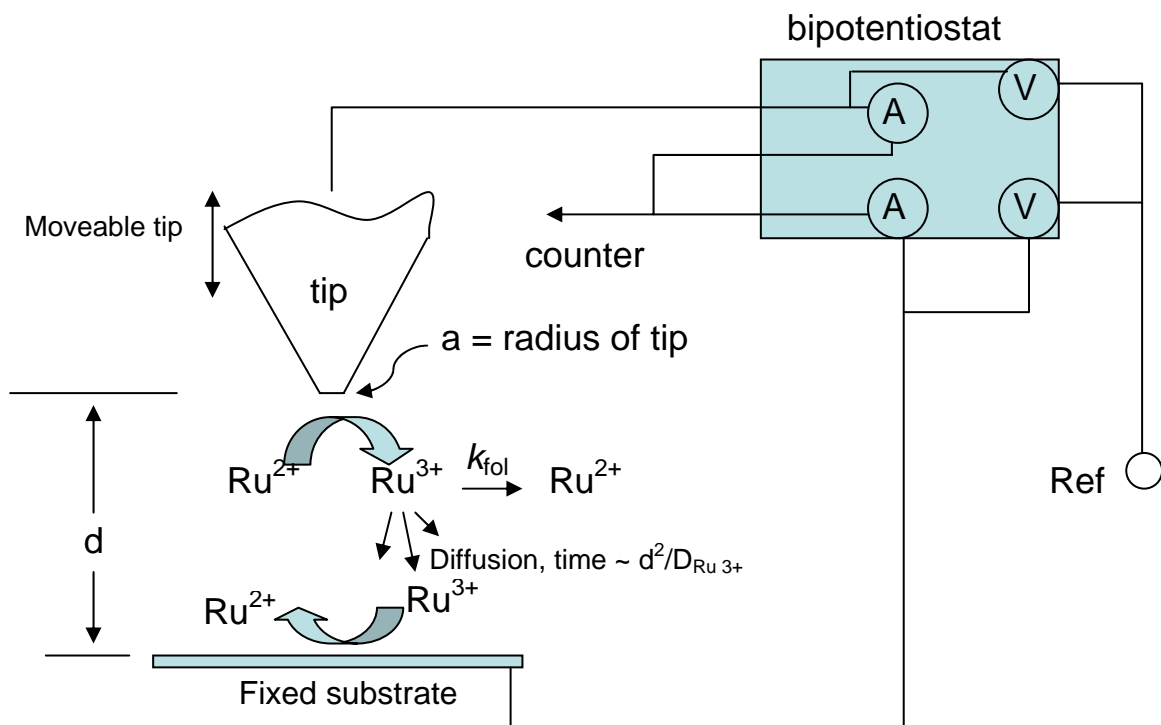


Figure 1-5. A schematic representation of a SECM experiment is shown, outlining various parameters and possible events occurring in the course of an experiment.

-
- ¹ [http://en.wikipedia.org/wiki/Intercalation_\(chemistry\)](http://en.wikipedia.org/wiki/Intercalation_(chemistry))
- ² <http://users.rcn.com/jkimball.ma.ultranet/BiologyPages/D/DoubleHelix.html>
- ³ http://www.blc.arizona.edu/Molecular_Graphics/DNA_Structure/DNA_Tutorial.HTML#Purine
- ⁴ Muench, K., *Genetic Medicine*, Elsevier, New York, 1988, p. 11.
- ⁵ Pezeshk, A., Symons, M., McClymont, J., *J. Phys. Chem.*, **1996**, *100*, 18562-18566.
- ⁶ Yoo, J., Stemp, E., Barton, J., *J. Am. Chem. Soc.*, **2003**, *125*, 6640-6641.
- ⁷ Fitzsimons, M., Barton, J., *J. Am. Chem. Soc.*, **1997**, *119*, 3379-3380.
- ⁸ Berthet, N., Constant, J., Demeunynck, P., Lhomme, J., *J. Med. Chem.*, **1997**, *40*, 3346-3352.
- ⁹ Tse, W., Boger, D., *Acc. Chem. Res.*, **2004**, *37*, 61-69.
- ¹⁰ Wong, E., Gooding, J., *Anal. Chem.*, **2003**, *75*, 3845-3852.
- ¹¹ Matsumoto, Y., Terui, N., Tanaka, S., *Eviron. Sci. Tech.*, **2006**, *40*, 4240-4244.
- ¹² Brana, M., Cacho, A., Gradillas, A., de Pascual-Teresa, B., Ramos, A., *Curr. Pharm. Des.*, **2001**, *7*, 1745-1780.
- ¹³ Martinez, R., Chacon-Garcia, L., *Curr. Med. Chem.*, **2005**, *12*, 127-151.
- ¹⁴ Wang, G., Zhang, J., Murray, R., *Anal. Chem.*, **2002**, *74*, 4320-4327.
- ¹⁵ Schatzschneider, U., Barton, J., *J. Am. Chem. Soc.*, **2004**, *126*, 8630-8631.
- ¹⁶ Petitjean, A., Barton, J., *J. Am. Chem. Soc.*, **2004**, *126*, 14728-14729.
- ¹⁷ Maruyama, T., Takata, T., Ichinose, H., Kamiya, N., Kuma, H., Hamasaki, N., Morita, H., Goto, M., *Biotechnol. Prog.*, **2005**, *21*, 575-579.
- ¹⁸ Onfelt, B., Lincoln, P., Norden, B., *J. Am. Chem. Soc.*, **2001**, *123*, 3630-3637.
- ¹⁹ Erikkila, K., Odom, D., Barton, J., *Chem. Rev.*, **1999**, *99*, 2777-2795.
- ²⁰ Delaney, S., Pascaly, M., Bhattacharya, K., Barton, J., *Inorg. Chem.*, **2002**, *41*, 1966-1974.
- ²¹ (a) Friedman, A., Chambron, J., Sauvage, J., Turro, N., Barton, J., *J. Am. Chem. Soc.*, **1990**, *112*, 4960-4962. (b) Turro, C., Bossmann, S. H., Jenkins, Y.; Barton, J.K., Turro, N.J., *J. Am. Chem. Soc.* **1995**, *117*, 9026-9032. (c) Olson, E.J.C., Hu, D.; Hormann, A., Honkman, A., Arkin, M., Stemp, E., Barton, J., Barbara, P., *J. Am. Chem. Soc.*, **1997**, *119*, 11458-11467. (d) Olofsson, J., Wilhelmsson, L. M., Lincoln, P., *J. Am. Chem. Soc.*, **2004**, *126*, 15454-15465.
- ²² Olofsson, J., Onfelt, B.; Lincoln, P., *J. Phys. Chem. A*, **2004**, *108*, 4291-4398.

-
- ²³ Hiort, C., Lincoln, P., Norden, B., *J. Am. Chem. Soc.*, **1993**, *115*, 3448-3454.
- ²⁴ Hercules, D., Lytle, F., *J. Am. Chem. Soc.*, **1966**, *88*, 4745.
- ²⁵ Velasco, J., *Electroanalysis*, **1991**, *3*, 261-271.
- ²⁶ Bard, A., Faulkner, L., *Electrochemical Methods*, John Wiley & Sons, New York, NY, 2001; p. 738.
- ²⁷ Waldemar, A., Cilento, G., *Chemical and Biological Generation of Excited States*, Academic Press, 1982; p. 193.
- ²⁸ Ibid, p. 197.
- ²⁹ Tokel, N., Bard, A., *J. Am. Chem. Soc.*, **1972**, *94*, 2862-2863.
- ³⁰ Tokel-Takvoryan, N., Hemingway, R., Bard, A., *J. Am. Chem. Soc.*, **1973**, *95*, 6582-6589.
- ³¹ Rubinstein, I., Bard, A. J., *J. Am. Chem. Soc.* **1981**, *103*, 512.
- ³² Velasco, J., *Electroanalysis*, **1991**, *3*, 261-271.
- ³³ Noffsinger, J., Danielson, N., *Anal. Chem.*, **1987**, *59*, 865-868.
- ³⁴ Miao, W., Choi, J., Bard, A., *J. Am. Chem. Soc.*, **2002**, *124*, 14478-14485.
- ³⁵ Kanoufi, F., Zu, Y., Bard, A., *J. Phys. Chem. B*, **2001**, *105*, 210-216.
- ³⁶ Bouchie, A., *Nature Biotech.*, **2003**, *21*, 958.
- ³⁷ <http://www.bioveris.com/technology/technology-why.htm>.
- ³⁸ Bard, A. J., Mirkin, M. V., *Scanning Electrochemical Microscopy*, Marcel Dekker, New York, **2001**.
- ³⁹ Bi, S., Liu, B., Fan, F., Bard, A. J., *J. Am. Chem. Soc.*, **2005**, *127*, 3690-3691.
- ⁴⁰ Testa, A., Reinmuth, W., *Anal. Chem.*, **1961**, *33*, 1320-1324.
- ⁴¹ (a) Carter, M. T., Bard, A. J., *Bioconj Chem*, **1990**, *2*, 257-263. (b) Rodriguez, M., Bard, A. J., *Anal. Chem*, **1990**, *62*, 2658-2662.

Chapter 2 Experimental

Synthesis and Materials

The required precursor to the target complex was not found to be commercially available so the synthesis of $\text{Ru}(\text{phen})_2\text{Cl}_2$ was attempted by the method of Whitten, et al. However, better yield was obtained by that outlined by Meyer.¹ To begin, 6.5 g of RuCl_3 (Sigma-Aldrich) was gently refluxed with 12.1 g of 1,10 phenanthroline (Sigma-Aldrich, St. Louis, MO, USA) (a 2:1 ligand to metal ratio) and 8.7 g of LiCl (Acros Organics, Geel, Belgium) for 8 h in 50 mL of DMF (ACROS ORGANICS, extra dry) in a three necked flask. The chemicals were used as received. Rubber septa were used on each of the two side necks and the condenser was used in the middle neck. A bath of silicon oil (Fisher Scientific, Pittsburgh, PA, USA) with a paperclip for a stirring bar was used with a stir plate for uniform heating. The flask was sunk about halfway in the bath and used a two inch Teflon® stirring bar. Several 10 mL aliquots of DMF were added over the 8 h to keep the solvent level constant.

After 8 h, the condenser was removed and the solvent reduced to about 20 mL. Upon cooling to room temperature, 150 mL of acetone (Fisher Scientific) was added to precipitate the precursor. After chilling overnight at 5°C, the dark crystals were suction filtered from a burgundy solution, rinsed with 18 M Ω water (water used in all cases is Milli-Q system, Millipore, Billerica, MA, USA) and diethyl ether (Fisher Scientific), and vacuum dried for 18 h at 100°C. Yield was 46% in ruthenium.

The dppz ligand was prepared via the method of Dickeson and Summers.² In this case, 0.61 g 1,10 – phenanthroline – 5,6 – quinine, and 0.36 g o-phenylenediamine (each

Sigma-Aldrich) were used as received. The near equimolar amounts were dissolved in 25 mL of ethanol, and the two solutions added together with a 2-inch stirbar on a stirplate. This solution was boiled until 75% of the solvent was removed. The solution turned dark brown upon heating, and like colored crystals formed upon cooling in an ice bath. The crystals were suction filtered and recast into 250 mL of 1:1 v/v water and ethanol and chilled in an ice bath in the dark overnight. The dppz product was recovered with filtration and dried at 100°C in a vacuum oven for 4 h.

The two precursors were mated together by modifying a $\text{Ru}(\text{bpy})_2\text{dppz}^{2+}$ synthesis in water under Ar .³ Specifically, 0.347 g of dppz and 0.639 g of $\text{Ru}(\text{phen})_2\text{Cl}_2$ were added to 400 mL of water. Rubber septa were used on each of the two side necks and a steady stream of argon was flowed via Tygon® tubing and a 5-inch, 18 gauge, needle through one of these necks. The needle was submerged in the solvent for the first 20 minutes of argon flow, then withdrawn to just above the liquid surface. The condenser was used in the middle neck with a rubber septum as a cap and a three-inch 20 gauge needle through the septum was used as a vent. The same silicon oil bath was used to reflux for 4.5 h. At the end of this time, the condenser was removed, and the solvent reduced to ~ 75 mL before 150 mL of additional water was added. The solution was boiled for 10 minutes in air. The resulting red solution was capped and allowed to chill overnight in the dark at 5°C. Next, the solution was filtered through a glass frit (medium) and 20 mL of a 10% solution of NaBF_4 (ACROS ORGANICS) was added. A bright orange precipitate formed. This precipitate was recast in 150 mL of ethanol and heated for 30 minutes before being cooled in an ice bath. The crystals were filtered and dried at *in vacuo* for 90 minutes at 110°C. The fine crystals were more red than orange.

Further purification was accomplished by first dissolving the crystals in 20 mL of 1:1 CH₂Cl₂:MeOH and then reducing to 10 mL with very gentle heating. This was loaded onto a 100 g alumina (Baker) column with a CH₂Cl₂ mobile phase. There was very little separation, but since the leading edge was more red than the bright orange tail fraction so it was discarded. The solvent was reduced, and the product re-crystallized with cold ethyl ether in an ice bath. Yield was 76% in Ru.

The 10% fluoro-borate solution suggested by Belser proved insufficient to displace all the chloride, and a Cl⁻/Cl₂ wave was seen upon initial electrochemical measurements. A five-fold molar excess was used with copious water washing of the solid to reduce this to an acceptable level.

All experiments used the resulting racemic mixture. Products were characterized by UV-Vis absorption in acetonitrile or ethanol (Fisher) and fluorescence in acetonitrile and water. Reference solutions of Ru(bpy)₃²⁺ and Ru(phen)₃²⁺ were made using commercial (Sigma-Aldrich, 98%) compounds.

Co-reactant solutions were prepared using tripropyl amine (TPrA - Sigma-Aldrich), sodium oxalate (Baker), and sodium monobasic and dibasic phosphate (Baker, Fisher) for the phosphate buffer system (PBS) stock. While the oxalate prep is straightforward, TPrA proved more involved. Briefly, the phosphate salt was added and the pH adjusted to < 2 with concentrated H₃PO₄ (Fisher). TPrA was added dropwise with stirring to obtain the desired concentration upon dilution. The pH was then adjusted to 7.5 by the addition of 2 M NaOH (Fisher).

Calf thymus DNA was obtained from Sigma-Aldrich and dissolved in PBS, pH 7.5, by gentle inversion over night at 5°C. The 20-mer poly dA-dT was synthesized by

Integrated DNA Technologies, Coralville, IA. The solid was dissolved to roughly 3×10^{-4} M in PBS pH 7.5, separated into five 1 mL aliquots and frozen as recommended by the manufacturer until needed. The actual concentration was determined by UV-Vis absorption at 260 nm, using an extinction coefficient of $6600 \text{ M}^{-1} \text{ cm}^{-1}$ for the CT DNA and $6300 \text{ M}^{-1} \text{ cm}^{-1}$ for the 20-mer.⁴

For the cysteine/ferrocyanide study, cysteine (free base, Sigma-Aldrich), potassium ferrocyanide (Fisher), sodium borate (Baker), and potassium chloride (Baker) were used as received. The buffer of 0.1 M borate was initially ~ pH 9.5 and was adjusted to pH 11 by adding 2 M NaOH and monitoring with a pH meter.

Mass Spectrometry

Experiments were performed on a ThermoFinnigan LCQ Duo quadrupole ion trap mass spectrometer equipped with an electrospray ionization source. The flow rate of the solutions was 5 $\mu\text{L}/\text{min}$. The lens and octapole voltages, sheath gas flow rate, capillary voltage and ion injection times were optimized for maximum intensity of the ion of interest. The capillary temperature was 200°C. The spectra shown represent an average of 20 microscans. In MS/MS experiments, the CAD energy was increased until the parent ion was ~10% of its original intensity.

UV-Vis and Fluorescence Measurements

All absorption spectra were obtained in a 1 cm quartz cell (Fisher) in acetonitrile, or buffer using a Milton Roy Spectronic 3000 while fluorescence was measured in both acetonitrile and water with a Photon Technologies Int'l (London, Ontario, Canada) fluorimeter.

Electrochemical Measurements

All aqueous potentials listed are vs. a commercial Ag/AgCl (CH Instruments, Austin, TX) reference electrode unless otherwise indicated. Working electrodes were Pt disks – one straight and one turned 90°, each $\sim 0.013 \text{ cm}^2$ which were built by the local glassblower. The counter was a Pt wire (CH Instruments) in a Teflon® capped CH Instruments glass cell. All electrodes were hand polished for two minutes in 0.5 micron alumina slurry on microcloth pads (both Buehler Ltd. Lake Bluff, IL) prior to each light generating experiment. When this arrangement did not yield reproducible results in the DNA part of the study, modifications were made as outlined below. Conventional cyclic voltammetry was conducted in a He drybox in acetonitrile (Aldrich anhydrous, 99.8%) with tetrabutylammonium hexafluorophosphate (Baker – electrochemical grade) as the electrolyte using a CHI 660 potentiostat. The digital simulations were run with DigiElch 2.0 (Institut für Anorganische und Analytische Chemie, Jena, GE). ECL experiments used an Autolab (Eco Chimie, Utrecht, the Netherlands). ECL light intensities were obtained using a PMT (Hamamatsu R4220p) coupled to a Keithly (Cleveland, OH) amplifier and merged with the voltammetric data in the Autolab software. ECL spectra were taken from a CCD camera (Princeton Instruments, Trenton, NJ) with λ calibrated against overhead fluorescent lights as described by the manufacturer (Roper Instruments, Acton, MA).

Light Measurements with DNA

Not surprisingly, studying ECL with DNA proved to be the most challenging part of the project. Initial work in an open cell with calf thymus DNA showed deviations at

times as much as 100%. A number of efforts were undertaken to alleviate this and are outlined here.

Experiments were conducted as standard additions as well as separate solutions for each R value ([base pairs] / [Ru]) studied. Since the $\text{Ru(phen)}_2\text{dppz}^{2+}$ compound has a longer fluorescence lifetime when intercalated into adenine/thymine (AT) base pairs than into guanine/cytocine (GC) according to ref 5, poly dA-dT was also studied. Also, to see if diffusion effects could be overcome, just 20-mer chains of poly dA-dT were used. A glassy carbon electrode also replaced Pt for a series of experiments. While the light produced improved due to larger electrode area, reproducibility did not. Efforts to reproducibly fix the cell cap and electrode geometry relative to the PMT by using alignment marks helped somewhat, but did not alleviate problems acceptably. The use of cleaning solutions (1 M NaOH:EtOH 1:1 and 0.5% Triton X-100) vs. hand polishing in alumina or diamond paste got the deviations down to less than 50%.

Looking for more improvement, a flow cell of 0.6 mL volume was used. This most nearly duplicated the experimental arrangement used by Carter et al. in their similar study of Ru(phen)_3^{2+} .⁵ It has two 0.045 cm² Pt disks embedded in a Lucite block with one used as the working electrode and the other as the counter. The block was screwed into a separate Lucite plate with a rubber gasket separating the two to form a chamber. Holes drilled into the block provided an inlet/outlet arrangement and 1 mm Teflon tubing was used. The Ag/AgCl reference was downstream in mated Tygon® tubing and a diagram is shown in Appendix A.

Still, this did not solve the poor reproducibility of peak light intensity measurements. Moving to a flow cell improved the speed of data collection but not data

quality initially. The final effort that proved to be the key for reproducibility was switching from cyclic voltammetry to a variation of a potential step experiment called pulsed amperometric detection or PAD.⁶ The potential profile with faradaic and PMT current in the flow cell is shown in Figure 6-1. The experiment began by first stepping the potential for 0.5 s to 1.21 V vs. Ag/AgCl – a good value for light production from CV experiments. Next, the potential was stepped to 1.7 V for 0.5 s where vigorous, visible oxygen production took place, then to -1.3 V for 4 s where similar proton reduction occurred. Such a negative potential was required due to relatively high, buffered pH. Then, the potential was stepped immediately back to 1.21 V where the light was sampled. Different permutations of this profile were explored to find the best signal to noise ratio without lingering in reduction to ensure as little degradation of the available polynucleotide as possible. Each measurement was repeated three times, then the cell was rinsed with 2 mL of buffer. The cleaning step was injection of 1 mL of the previously mentioned base/ethanolic solution, which was allowed to sit for 1 min before rinsing with 5 mL of buffer. Only then was the next sample run. There was good agreement (+/-5%) between measurements and between subsequent runs done at the same R value. Light produced was also reproducible (also 5%) on consecutive days.

Scanning Electrochemical Microscopy

A lab built, 24 μm diameter (electrochemically verified in ferrocene methanol) Pt disk electrode was prepared as previously published.⁷ It was polished to an optical RG of ~ 2 and used as the tip. Subsequent approach curves verified the RG. The Pt substrate

was the same, straight electrode mentioned above. A CH Instruments 900 bipotentiostat was used to conduct the approaches and subsequent kinetic experiments.

-
- ¹ (a) Sprintschnik, G., Sprintschnik, H., Kirsch, P. P., Whitten, D., *J. Am. Chem. Soc.*, **1977**, *99*, 4947-4954.
(b) Sullivan, B., Salmon, D., Meyer, T., *Inorg. Chem.*, **1978**, *17*, 3334-3341.
- ² Dickeson, J., Summers, L., *Aust. J. Chem.*, **1970**, *23*, 1023-1027.
- ³ (a) Amouyal, E., Homsy, A., Chambron, J., Sauvage, J., *J. Chem. Soc. Dalton Trans.*, **1990**, *6*, 1841-1844.
(b) Belser, J., *Hel. Chem. Acta*, **1980**, *63*, 1675.
- ⁴ Fasman, G., *CRC Handbook of Biochemistry and Molecular Biology*, 3rd Ed.; CRC Press: Boca Raton, FL, 1975; Nucleic Acids Vol 1, p. 590.
- ⁵ Carter, M., Bard, A., *Bioconj Chem*, **1990**, *2*, 257-263.
- ⁶(a) Johnson, D., LaCourse, W., *Anal. Chem.*, **1990**, *62*, 589A – 597A. (b) Hughes, S., Meschi, P., Johnson, D., *Anal. Chim. Acta*, **1981**, *132*, 1-10.
- ⁷ Zoski, C., *Electroanalysis*, **2002**, *14*, 1041-1051.

Chapter 3 Electrochemistry of Ru(phen)₂dppz²⁺

Diffusion Coefficients

One of the key issues for study of the ECL of a complex is the basic electrochemistry of the compound since the first oxidation and reduction waves offer insight into the energetics of the HOMO and LUMO respectively.¹ Additionally, since ECL is a solution based process, the stability of the complex in its oxidized and reduced forms may be determined. In the case of Ru(phen)₂dppz²⁺, this study focuses on the 3+ and 1+ states. Figure 3-1 displays the cyclic voltammetry for the synthesized compound in acetonitrile with that of Ru(phen)₃Cl₂. The data showed peak splitting and peak currents were consistent with a reversible, diffusion controlled process over scan rates of 0.1, 0.2, 0.5, 0.75, 1, 5, and 10 V/s. Plots of peak current vs. the square root of the scan rate for each reversible peak in the first oxidation and reduction were linear with small intercepts (Figure 3-2), and peak current error was less than 1% at each scan rate again indicating the stability of the two explored 3+ and 1+ states. When swept anodic, the results using the 0.0131 cm² Pt disk electrode yielded a diffusion coefficient of 6.3 +/- 0.6 x 10⁻⁶ cm²/s. The results were only slightly different when exploring negative potentials. The initial cathodic peak showed an average diffusion coefficient of 7.3 +/- 0.3 x 10⁻⁶ cm²/s.

Digital Simulation

While the peak splitting hovered around 75 mV at low scan rates, that figure increased linearly with the square root of the scan rate, consistent with uncompensated

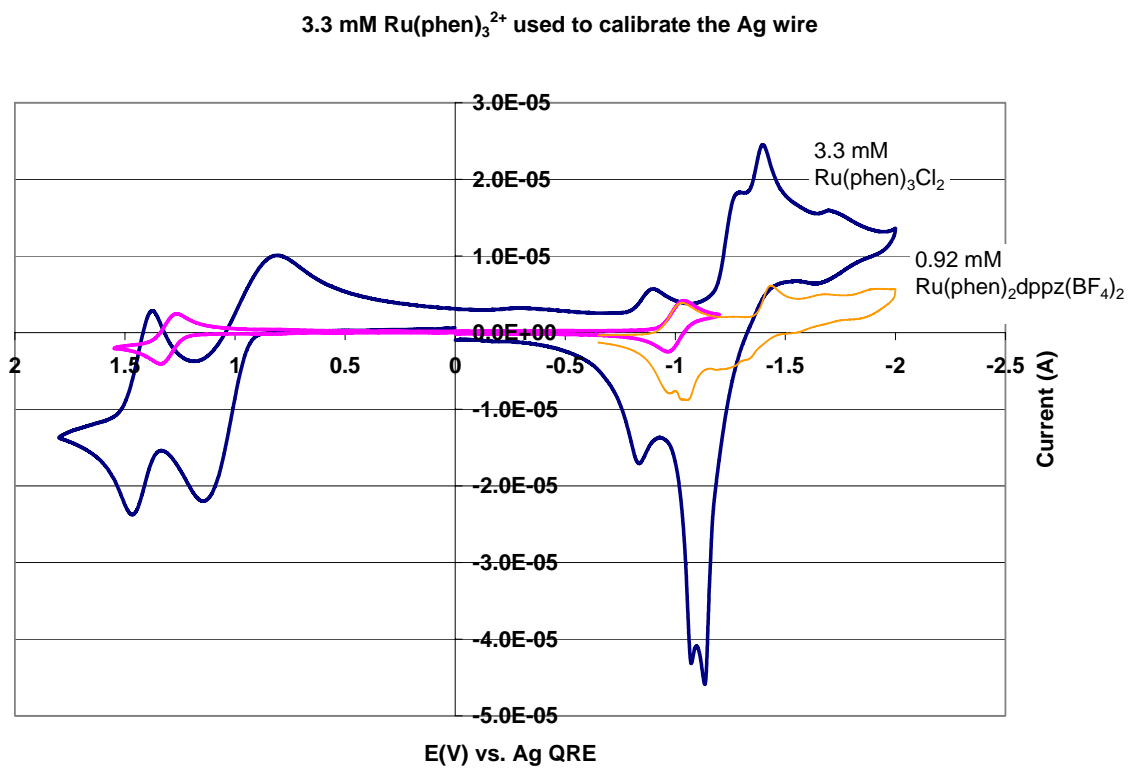


Figure 3-1. Cyclic voltammetry at 300 mV/s of 1mM lab synthesized Ru(phen)₂dppz(BF₄)₂ (pink and orange traces) and commercially available Ru(phen)₃Cl₂ (blue trace). Experiment conducted in a helium drybox at a Pt electrode in acetonitrile with 0.1 M tetrabutylhexammoniumfluorophosphate (TBAPF₆) as the electrolyte. The Ag wire quasi-reference electrode (QRE) was calibrated at the end by adding trisphen and was found to be 7 mV positive of SCE.

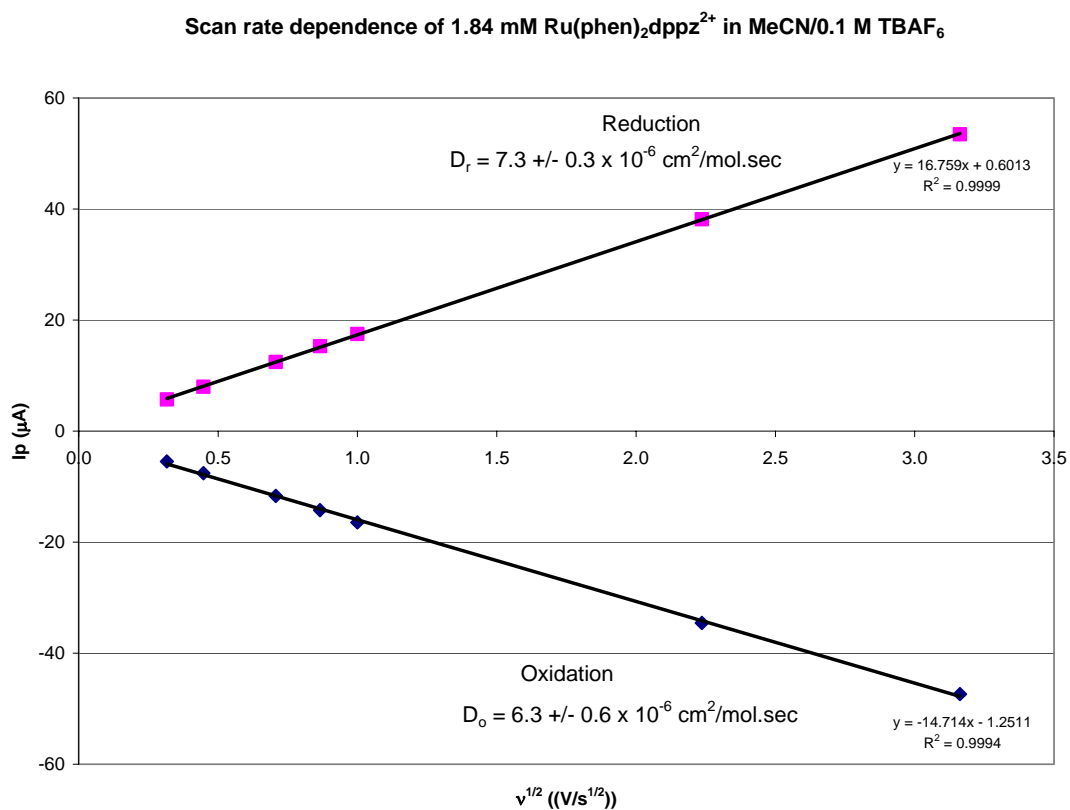


Figure 3-2. A scan rate study in the helium drybox used to determine the diffusion coefficients for the oxidized and reduced species in acetonitrile. The reduction side proved to be more precise though both sets of data extrapolate to near zero.

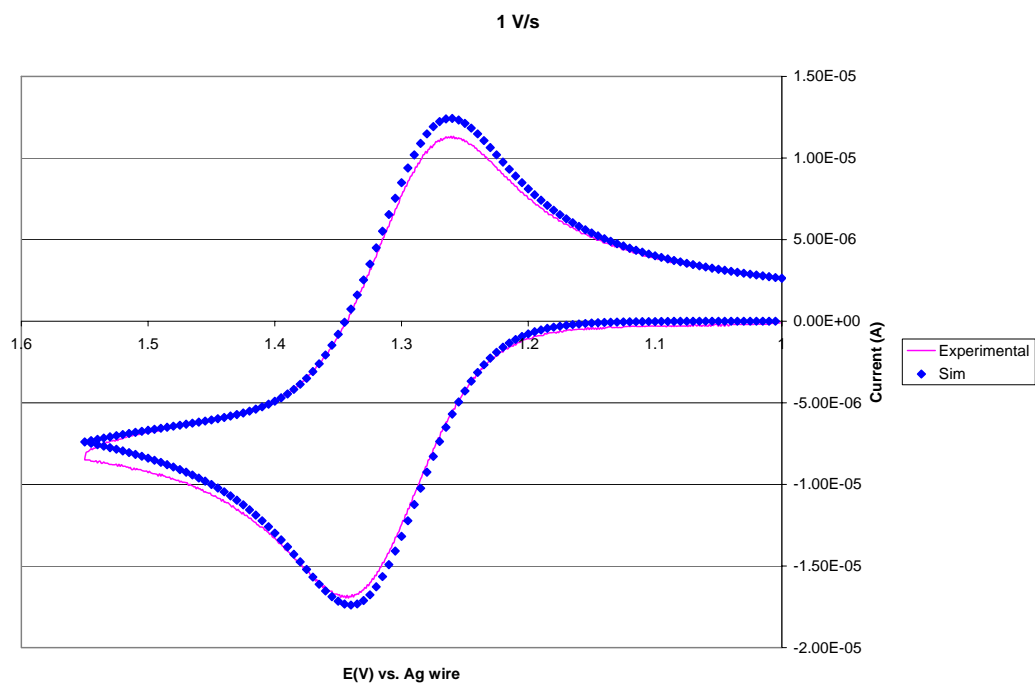
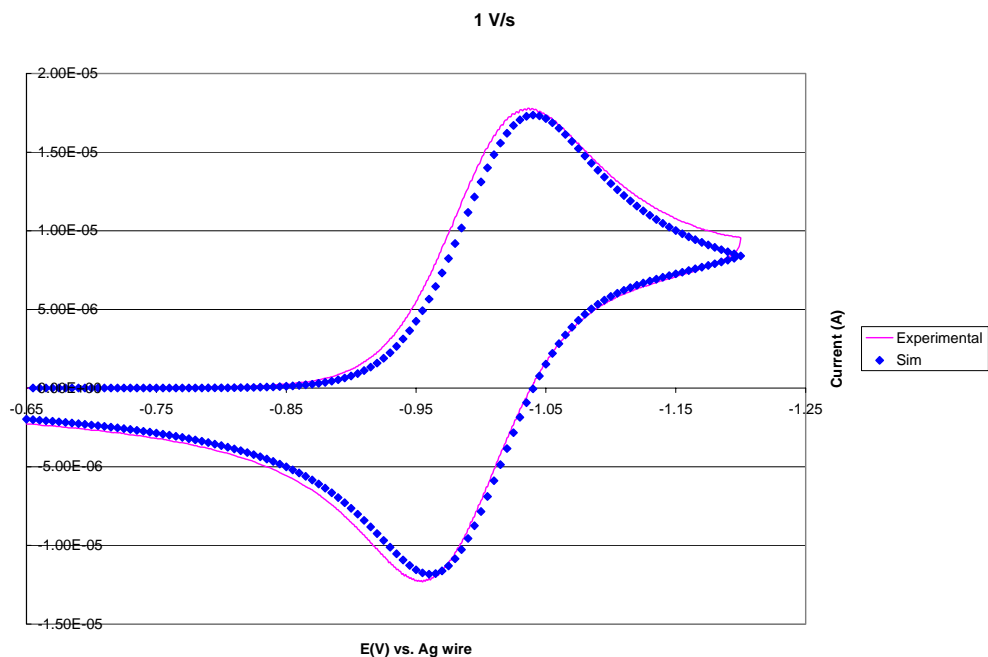


Figure 3-3. Examples of digital simulations of cyclic voltammetry at 1 V/s carried out using DigiElch. Close agreement with the experimental data verifies Nernstian behavior of the 1+ and 3+ states of the complex as well as the experimentally determined diffusion coefficients. Similar simulations were done for all scan rates shown in Figure 3-2 with only minor deviations at 10 V/s.

resistance (488Ω) in the measurement. The finding was verified by digital simulation over the entire range of scan rates studied and confirms that the heterogeneous electrode kinetics are fast. Some representative comparisons between the actual and simulated data are contained in Figure 3-3. The ratio of peak heights on the oxidation side was consistently close to unity – no more than 1.2 for the oxidation which confirmed a one electron process there. However, that is not the case for reduction as can be seen in Figure 3-1. The large, symmetric negative peak was the result of an unexplored process that occurred after the first wave. While electrons were added singly, they apparently were not removed in that manner and the symmetry of the anodic peak on reversal suggests a surface desorption very similar to $\text{Ru}(\text{phen})_3^{2+}$.² When the negative cathodic sweep was reversed just as the current fell from the first peak, a reversible wave resulted (Figure 3-1, pink trace). The magnitude of both peaks matched nicely with the oxidation side to again verify a one electron process in both cases. The peak splitting for the first reduction wave shown in Figure 3-1 was about 20 mV more than when the experiment does not venture to potentials that produce the Ru^0 and Ru^{1-} specie before sweep reversal, indicating more complex behavior past the first reduction peak.

Behavior Beyond the First Reduction Wave

To better understand this complex behavior, commercial $\text{Ru}(\text{phen})_3\text{Cl}_2$ was added *in situ* after the scan rate study was completed at a concentration greater than three times the $\text{Ru}(\text{phen})_2\text{dppz}^{2+}$ in order to avoid ambiguity. While addition of the more concentrated compound shifted the $\text{Ru}(\text{phen})_2\text{dppz}^{2+}$ reduction wave slightly positive (due to the QRE), it can be seen from Figure 3-1 that in the trisphen complex, the first electron goes to an arbitrary phenanthroline ligand. This subsequently makes it more difficult to reduce the next ligand as

Tokel et al. found in ref 2, albeit with larger peak displacement from the first wave than seen in this work. Additionally, the large symmetrical peak seen upon sweep reversal indicates that reduction to Ru(0) and further renders it insoluble, and it deposits on the electrode surface. The size of the desorption peak indicates all specie are desorbed at once on sweep reversal. As can be seen on additional orange trace in Figure 3-1, the two phenanthroline ligands in Ru(phen)₂dppz²⁺ exhibit similar behavior.

Determination of Standard Potentials

As is usually the case with non-aqueous electrochemistry, a suitable reference electrode is not always convenient to use in the confines of a drybox environment, so a silver wire is used as a ‘quasi-reference’ electrode during the experiment. The calibration of the quasi-reference is carried out at the end of the experiment *in-situ* by the addition of an electrochemically well known standard chemical. However, that turned out to not be required for this experiment because the chloride to chlorine oxidation wave provided an internal standard. Chloride was present as the counter ion in the commercial trisphen added for comparison to the complex of interest, but a difficulty arose in that the kinetics are not nernstian upon reversal, presumably because the oxidation product is a gas and some material is lost before sweeping back to reduce the Cl₂. Still, the size of the first anodic peak demonstrated it is a two electron process compared to oxidation of the metal center, which occurs immediately afterwards since the peak height of the earlier wave is twice as large. To obtain a calibration, the $E_{1/2}$ for the reversible waves in Ru(phen)₂dppz²⁺ was obtained by using the equation:

$$(E_{pa} - E_{pc}) / 2 = E_{1/2} \quad \text{Eq. 3-1}$$

The $E_{1/2}$ was then compared to the E_{pa} , and the difference found to be 35 mV, very close to the value of 28.5 mV listed by Bard for a room temperature measurement.³ From that, the $E_{1/2}$ for chloride vs. the Ag wire was determined from its E_{pa} to be 1.110 V. Since the chloride/chlorine couple is 1.117 V vs. SCE (standard calomel electrode), the Ag wire is thus determined to be 7 mV positive of SCE. This makes the first oxidation of the trisphen complex used in the experiment 1.42 V vs. SCE which is in good agreement with values from multiple sources.⁴ It then follows that the E_{ox} for $Ru(phen)_2dppz(BF_4)_2$ is 1.33 V +/- 0.1% vs. SCE (1.57 V vs. NHE) and the E_{red} -0.993 V +/- 0.1% vs. SCE (- 0.753 V vs. NHE). These results are listed with other related data in Table 3-1. The oxidation value differs somewhat from Barton's results of 1.63 V vs. SHE in DMF.⁵

Given the poor solubility of $Ru(phen)_2dppz^{2+}$ in water (<0.1 mM at pH 7.5), aqueous work showed very little electrochemistry above the background processes (see Figure 3-4). Unfortunately, at the micromolar concentrations available for this complex due to its poor solubility, this peak is hard to distinguish from the background oxidation of water that starts to take place at electrode potentials beyond 1V vs. Ag/AgCl. Attempts to see this wave via simple subtraction of a buffer only voltammogram resulted in poor results. To get at least a rough idea of the aqueous oxidation potential, differential pulse voltammetry was done in nitrate electrolyte at pH 2 where the solubility was slightly better. A consistent $E_{1/2}$ value of 1.12V vs. Ag/AgCl was found which is a slightly negative value compared to where light production occurred in ECL experiments at pH 7.5 in Chapter 5. Better aqueous data was subsequently obtained during the SECM experiments discussed in Chapter 7.

Analysis of Derived Potentials

As shown in Table 3-1, the trend imposed by the substitution of the dppz ligand onto the parent homoleptic complex is followed in the Ru(phen)_x family as with the Ru(bpy)_x family. The extent of the effect however, is more pronounced when going from Ru(phen)₃²⁺ to Ru(phen)₂dppz²⁺. Note in Table 3-1 how the oxidation potential is more negative and the reduction potential is more positive than the parent in each case but the magnitude of the difference in Ru(phen)₂dppz²⁺ is more pronounced. Additionally, the greatest effect is on the reduction side, similar to the Ru(bpy)₃²⁺ analogue, which is an indication of the energetics of the LUMO. This large decrease in the reduction potential compared to the parent, homoleptic compound was consistent with the correlations made by Baragaletti et al. in analyzing the trend in the electrochemical reduction of the free ligand and the ruthenium complex incorporating that ligand. In that work, they showed that the most common ligands studied fall along a line, with a slope near unity, on a plot of $E_{1/2}$ of the ligand vs. the $E_{1/2}$ of the first reduction in the complex. One of the two notable exceptions was the dppz ligand which showed it was much easier to reduce once complexed with the ruthenium which is the same trend shown here for Ru(phen)₂dppz²⁺.

Finally, as the reduction side of Figure 3-1 clearly shows, when comparing the first reduction wave of Ru(phen)₂dppz²⁺ to Ru(phen)₃²⁺, the LUMO in the compound of interest is based on the dppz ligand and not one of the other two phenanthroline ligands. Thus the electrochemistry agreed well with what is seen in the light induced metal-ligand charge transfer (MLCT) state that emits from the phenazine portion of the complex. That orbital is responsible for most of the negative energy difference when moving from the parent ligand.

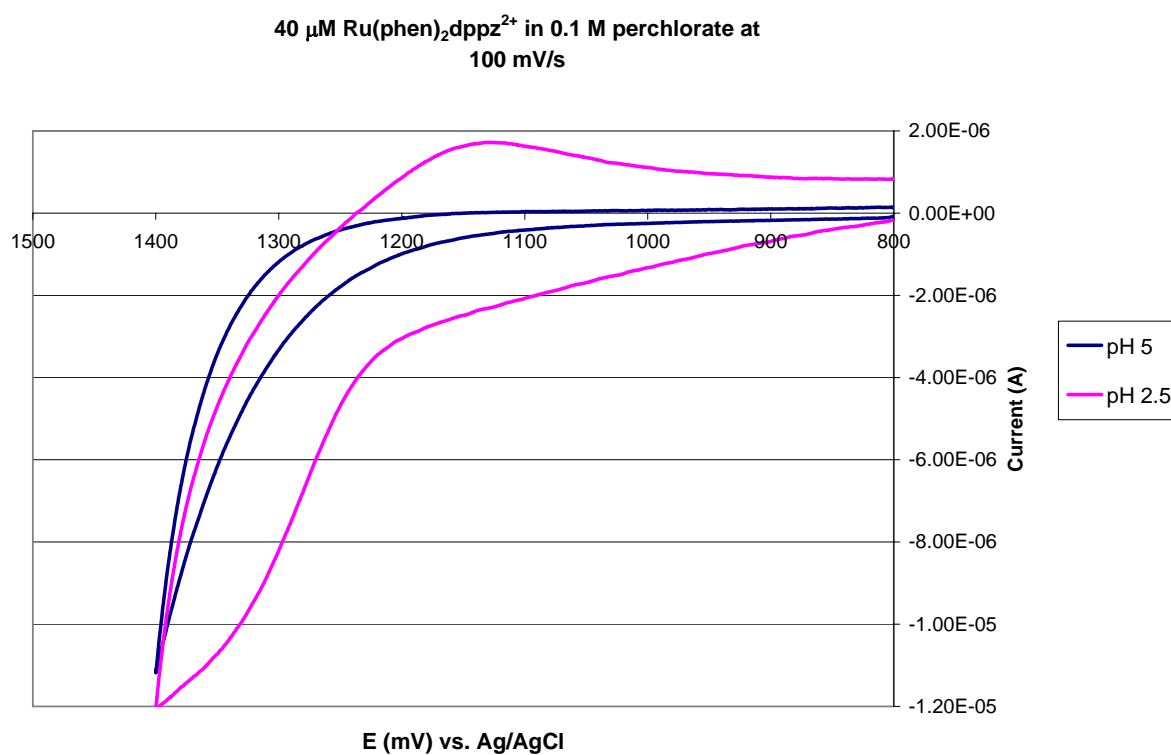


Figure 3-4. Aqueous, air saturated cyclic voltammetry at 100 mV/s and two different pH's. The poor solubility prevents seeing any meaningful electrochemistry. While an oxidation peak was visible using differential pulse voltammetry, the precision was poor in conducting a pulse width study.

| | Eox | Ered | ΔE (eV) | ΔE (eV) for dppz | References |
|----------------------------|------|--------|-----------------|--------------------------|--------------|
| Ru(bpy) ₃ | 1.29 | -1.33 | 2.62 | | 4 |
| Ru(bpy) ₂ dppz | 1.24 | -1.02 | 2.26 | -0.36 | 4 |
| Ru(phen) ₃ | 1.4 | -1.41 | 2.81 | | 2 |
| Ru(phen) ₂ dppz | 1.33 | -0.993 | 2.32 | -0.49 | Present work |

Table 3-1. Various oxidized and reduced E^0 data of related ruthenium complexes vs. SCE at Pt in 0.1 M TBAPF₆/acetonitrile.

¹ Velasco, J., *Electroanalysis*, **1991**, 3, 261-271.

² Tokel -Takvoryan, N., Hemingway, R., Bard, A., *J. Am. Chem. Soc.*, **1973**, 95, 6582-6589

³ Bard, A. J., Faulkner, L. R., *Electrochemical Methods: Fundamentals and Applications*, 2nd ed., John Wiley & Sons, New York, **2001**, p. 231.

⁴ Balzani, V., Juris, A., Barigelletti, F., Campagna, S., Belser, P., Von Zelewsky, A., *Ru(II) Polypyridine Complexes: Photophysics, Photochemistry, Electrochemistry, and Chemiluminescence*, Elsevier Science Publishers, **1988**, p. 135.

⁵ Murphy, J., Arkin, M., Ghatlia, N., Bossmann, S., Turro, N., Barton, J., *Proc. Natl. Acad. Sci. USA*, 91, 5315-5319, June 1994.

Chapter 4 Spectroscopy

Free Complex

UV-visible absorbance, fluorescence (PL), and mass spectroscopy were used to further analyze the synthesized product to ensure it was the product of interest. Figure 4-1 shows the aqueous absorbance in phosphate buffer along with a plot of absorbance vs. concentration for the two dominant peaks in the visible, 375 nm and 440 nm. Their extinction coefficients obtained from the slope of these plots are nearly identical at $19500\text{ cm}^{-1}\text{ M}^{-1} \pm 3\%$ for the former and $18150\text{ cm}^{-1}\text{ M}^{-1} \pm 3\%$ for the latter. This is slightly lower than Barton's figure of 24800 and $22300\text{ cm}^{-1}\text{ M}^{-1}$ for 372 and 439 nm respectively for their hexafluorophosphate salts in water/DMSO mixtures.¹ The higher energy peak is described as an intra-ligand charge transfer transition on the dppz ligand, and the lower peak from the MLCT described in Chapter 1.

Figure 4-2 shows a comparison between equimolar solutions of the lab-synthesized compound in phosphate buffer and acetonitrile to demonstrate the light-switch behavior. The excitation wavelength was 440 nm based on the absorbance data which also aided in comparing to other work cited which used the same excitation energy. An aqueous buffer solution of commercial trisphen at similar concentration is shown to highlight the red-shift that accompanies the substitution of the dppz ligand. Further inspection reveals an extremely low emission in the aqueous solution. Given the analytical plot of PL intensity vs. $[\text{Ru}(\text{phen})_3]^{2+}$ (Figure 4-3) the data suggests nanomolar amounts ($\sim 1\%$) of trisphen is left over from the synthesis as an impurity. The data points labeled $\text{Ru}(\text{phen})_2\text{dppz}^{2+}$ are this impurity peak and are included for comparison against the pure trisphen complex. Mass spectrometry also showed the purity to be at least 99% (Figure 4-4).²

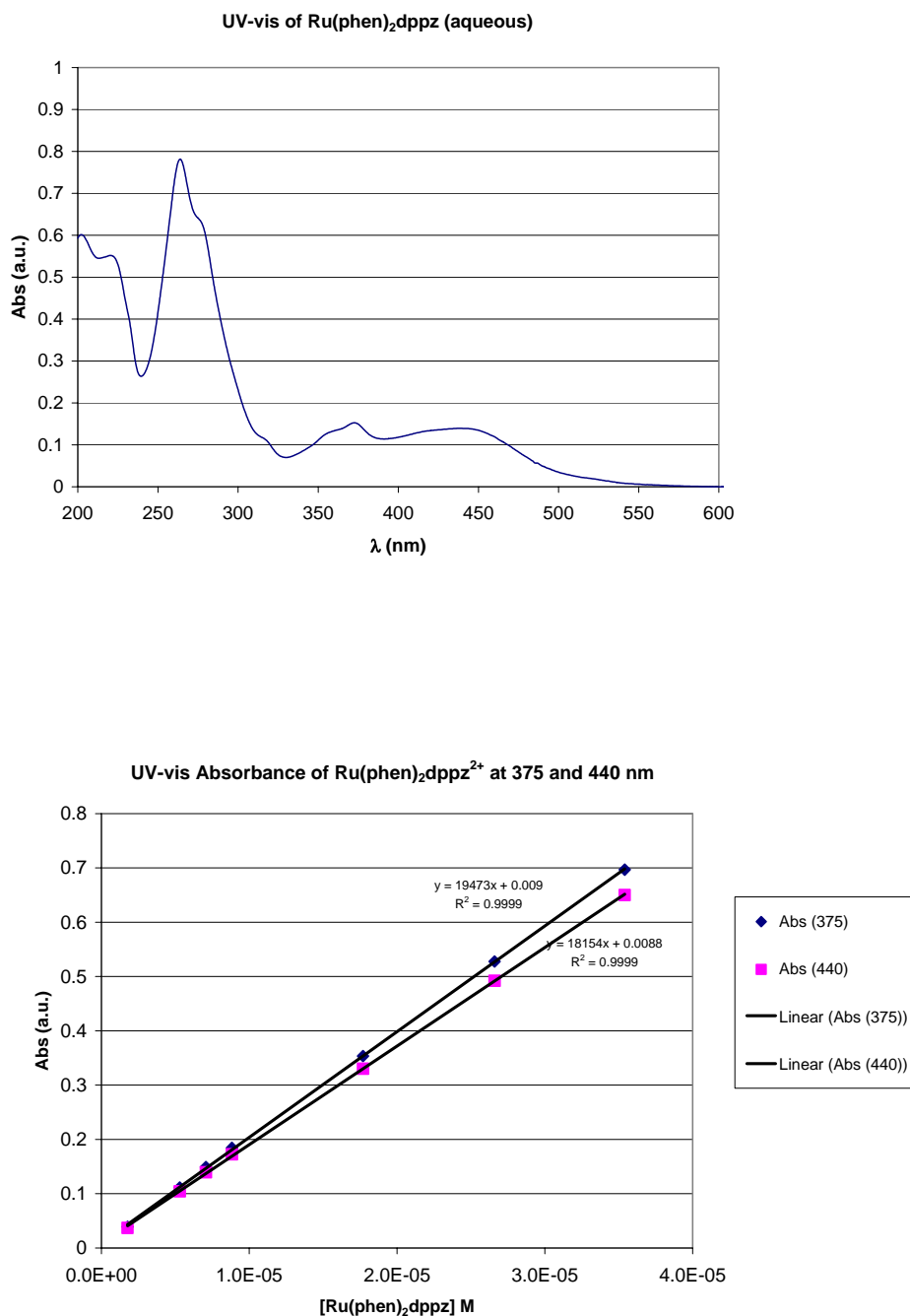


Figure 4-1. The UV-visible absorbance spectrum (top) of the lab synthesized Ru(phen)₂dppz(BF₄)₂ in 0.1M phosphate buffer, pH 7.5. The peaks at 375 and 440 nm were both explored to determine an extinction coefficient (bottom) with deviations of only 3%.

50 μM $\text{Ru}(\text{phen})_3^{2+}$ and $\text{Ru}(\text{phen})_2\text{dppz}^{2+}$ photoluminescence

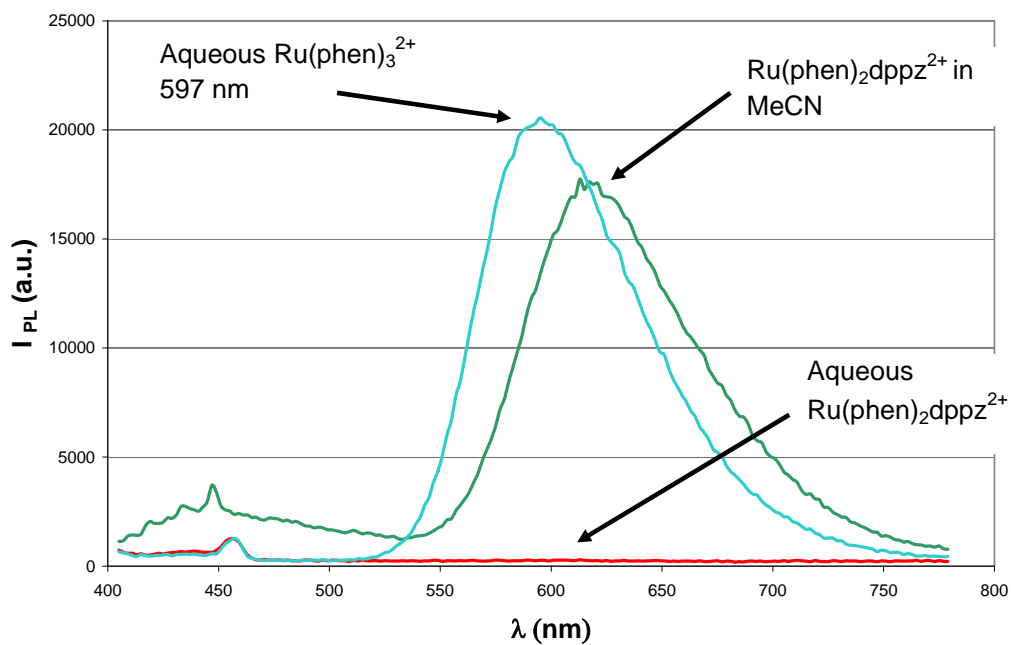


Figure 4-2. A comparison between equimolar solutions of the lab-synthesized compound in phosphate buffer and acetonitrile to demonstrate the light-switch behavior. An aqueous buffer solution of commercial trisphen at similar concentration is shown to highlight the red-shift that accompanies the substitution of the dppz ligand.

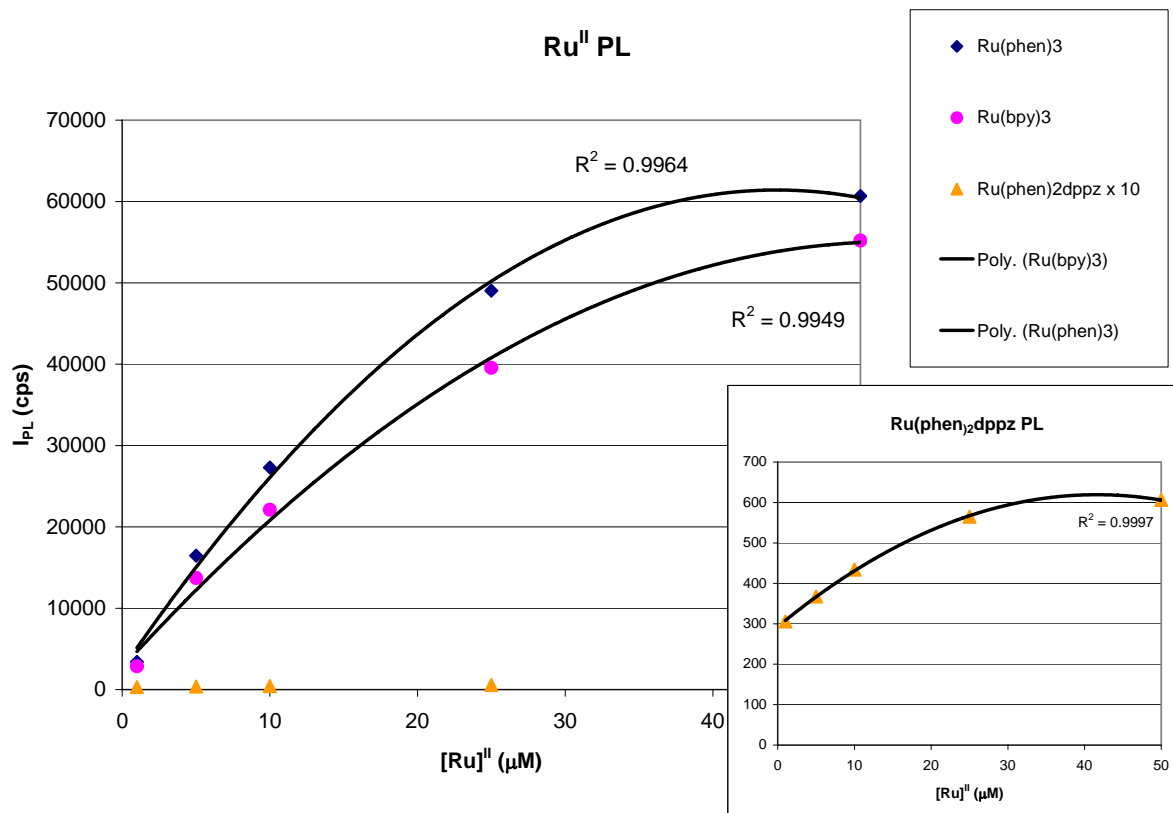


Figure 4-3. The fluorescence intensity at 617 nm over a range of concentrations of commercial reference ruthenium complexes and the lab-synthesized Ru(phen)₂dppz(BF₄)₂ all in phosphate buffer, pH 7.5. The extremely low emission from the dppz-modified complex is a small trisphen impurity that persisted despite a column chromatography purification step. It is interesting to note all exhibit significant intra-filter effects over large concentration changes.

A more detailed analysis of this impurity follows in the DNA section of this chapter. Furthermore, as was also demonstrated in ref 2, addition of acetonitrile to the solvent allows low-grade emission to occur but red-shifted from the pure acetonitrile peak. This is demonstrated in Figure 4-5. The blue trace is fluorescence of water only to establish the background. The green trace is after addition of $\text{Ru(phen)}_2\text{dppz}^{2+}$ and is not distinguishable from the background. However, the red trace showed weak emission but shifted to a peak around 650 nm with an even weaker component displayed at 800 nm.

Correlation of Spectroscopy to Electrochemistry

The potential difference between the first oxidation and first reduction of $\text{Ru(phen)}_2\text{dppz}^{2+}$ (2.3 eV) was smaller than that for Ru(bpy)_3^{2+} and Ru(phen)_3^{2+} which were about 2.6 eV and 2.8 eV respectively (see Table 4-1).³ However, since $\text{Ru(bpy)}_2\text{dppz}^{2+}$ had a potential difference of 2.3 eV^{1a} which was 0.3 eV lower than its parent Ru(bpy)_3^{2+} , there was no surprise that $\text{Ru(phen)}_2\text{dppz}^{2+}$ was lower than Ru(phen)_3^{2+} . The two families differed only in the magnitude of this measurement. This trend in the electrochemical redox difference translated to the photoluminescence data since the dppz analogue's emission peak was red shifted from the parent Ru(L)_3^{2+} complex (Table 4-1). This behavior differed from the Ru(bpy)_3^{2+} to $\text{Ru(bpy)}_2\text{dppz}^{2+}$ comparison where they each had essentially the same emission.⁵ In contrast, data for $\text{Ru(phen)}_2\text{dppz}^{2+}$, like its cousin $\text{Ru(bpy)}_2\text{dppz}^{2+}$, fell well above the plot by Barigelletti et al. of $\Delta E_{1/2}$ vs. $h\nu$ emission for families of $\text{Ru(L)}_2\text{L}'$.⁴ This indicates our synthesized product is indeed the product of interest and behaves as expected from previously published data.

| | PL emission (nm) | PL emission (eV) | Δ PL (eV) for dppz | References |
|----------------------------|------------------|------------------|---------------------------|--------------|
| Ru(bpy) ₃ | 607 | 2.06 | | 5 |
| Ru(bpy) ₂ dppz | 610 | 2.05 | -0.01 | 5 |
| Ru(phen) ₃ | 597 | 2.08 | | Present work |
| Ru(phen) ₂ dppz | 617 | 2.01 | -0.07 | Present work |

Table 4-1. Aqueous photophysical properties of selected complexes. The trisphen data was measured for this work with commercially available compound.

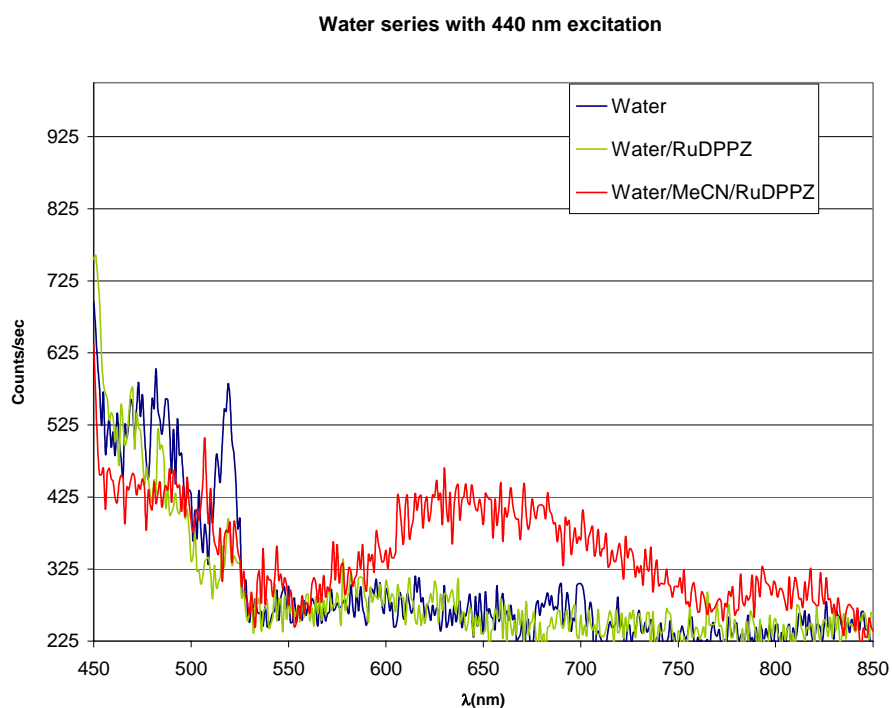


Figure 4-4. Ru(phen)₂dppz²⁺ emission in water arising from the addition of acetonitrile. Concentration is 100 μ M and the peak is red-shifted from the pure acetonitrile peak.

In general, differences between the redox and optical energies are attributed to the energy to solvate the complex, inner and outer sphere energy barriers, and the Coulombic energy required to move the charge from the center to the ligand.⁵ In this case, the similarity of the dppz ligand to the other two ligands (the phenanthroline moiety) apparently makes a difference in the observed trend.

DNA Intercalated Complex

From the beginning there was concern about impurities since the most likely one, Ru(phen)_3^{2+} , will also undergo ECL and cause confusion when determining if $\text{Ru(phen)}_2\text{dppz}^{2+}$ will exhibit light switch behavior in ECL as it does PL. The mass spectroscopic analysis (Figure 4-4) of both fractions from the chromatographic purification show there was some impurity present. Mass analysis of the small peaks in question show mostly variations of the target complex but trisphen was among those present. The most prominent peak, at a m/z of 830, is the target complex less one counter ion. However, there was a very small peak at a m/z of 740 that corresponded to trisphen in the same situation. Also, as discussed in Chapter 2, there was chloride present so the target complex with that anion was represented as the minor peak at a m/z of 780. To verify its effect in the mix, commercially available trisphen was characterized and found to emit at 595 nm. There was a very low grade emission from our synthesized product at 595 nm as seen in Figure 4-5. However, as DNA is titrated into the solution of metal complex, a peak at 617 nm grows from the background as expected and the peak at 595 nm was lost.

As discussed in two different sources (refs 2 and 8), there was little emission that occurred from $\text{Ru(phen)}_2\text{dppz}^{2+}$ in water. Since the measurable peak was beyond 700 nm, the little that is detected from our synthesized compound could not be the complex of interest. As

the MS data and ref 2 would indicate, the emission at 617 nm seen in Figure 4-4 that arises after DNA addition meant $\text{Ru}(\text{phen})_2\text{dppz}^{2+}$ was present and in good purity. Additionally, Liu et al. showed that the emission shift upon intercalation was also blue for other compounds where the dppz ligand was slightly modified.⁶ In our data, the shift upon DNA addition is red indicating the two emissions are from different species not the same one in an intercalated and non-intercalated environment. In all completely aqueous experiments, no emission was seen beyond the one broad peak at 617 nm. The consequences of this are addressed further in Chapter 5.

Determination of the Binding Constant

In order to establish a binding constant for the synthesized product, additional fluorescence studies were undertaken with the complex in two different polynucleotide solutions. Both un-sonicated calf thymus DNA and 20-mer poly dA-dT were used to show PL from the complex. Normally, the PL data would be rendered dimensionless by looking at the ratio of $I(R)/I(0)$, but $I(0)$ was buried in the background at the 1 μM concentration used which complicated the approach. This required obtaining the lamp intensity in order to plot absolute data which was done using $\text{Ru}(\text{bpy})_3^{2+}$, whose PL behavior is well characterized.⁷

Thus, the equation for the PL data is:

$$I(R) = 2.3I_0L(\epsilon_f C_f \phi_f + \epsilon_b C_b \phi_b) \quad \text{Eq. 4-1}$$

where

$$C_b = (b - \{b^2 - (2Kb^2 C_t [NP]/s)\}^{1/2}) / 2Kb \quad \text{Eq. 4-2}$$

and

$$b = 1 + Kb C_t + Kb [NP] / 2s \quad \text{Eq. 4-3}$$

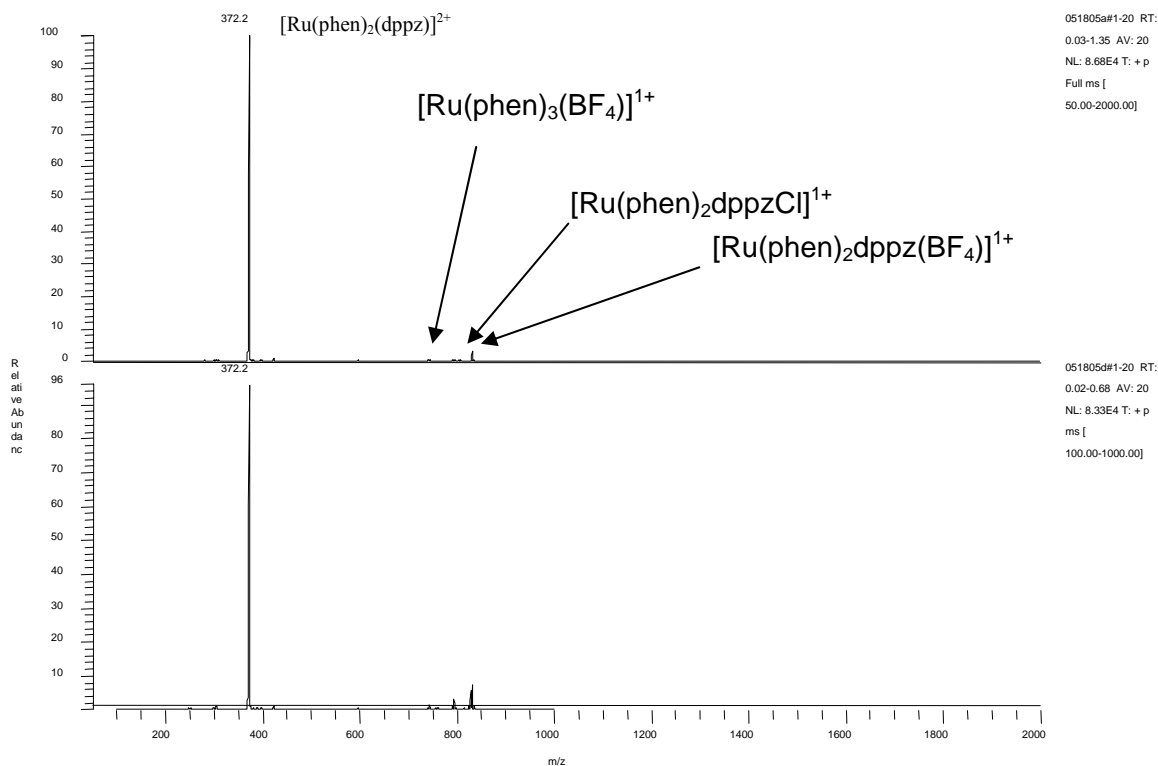


Figure 4-5. An MS/MS experiment with a quadrupole ion trap mass spectrometer equipped with an electrospray ionization source. The spectra shown represent an average of 20 microscans. The bottom scan represents the initial fraction from the chromatography column and the top a fraction taken later. There was no clear separation during the purification step. All experiments come from complex precipitated from the second fraction. The mass to charge peak at 372.2 is the doubly charged, intact cation $\text{Ru}(\text{phen})_2\text{dppz}^{2+}$. Note the very small amount of trisphen present.

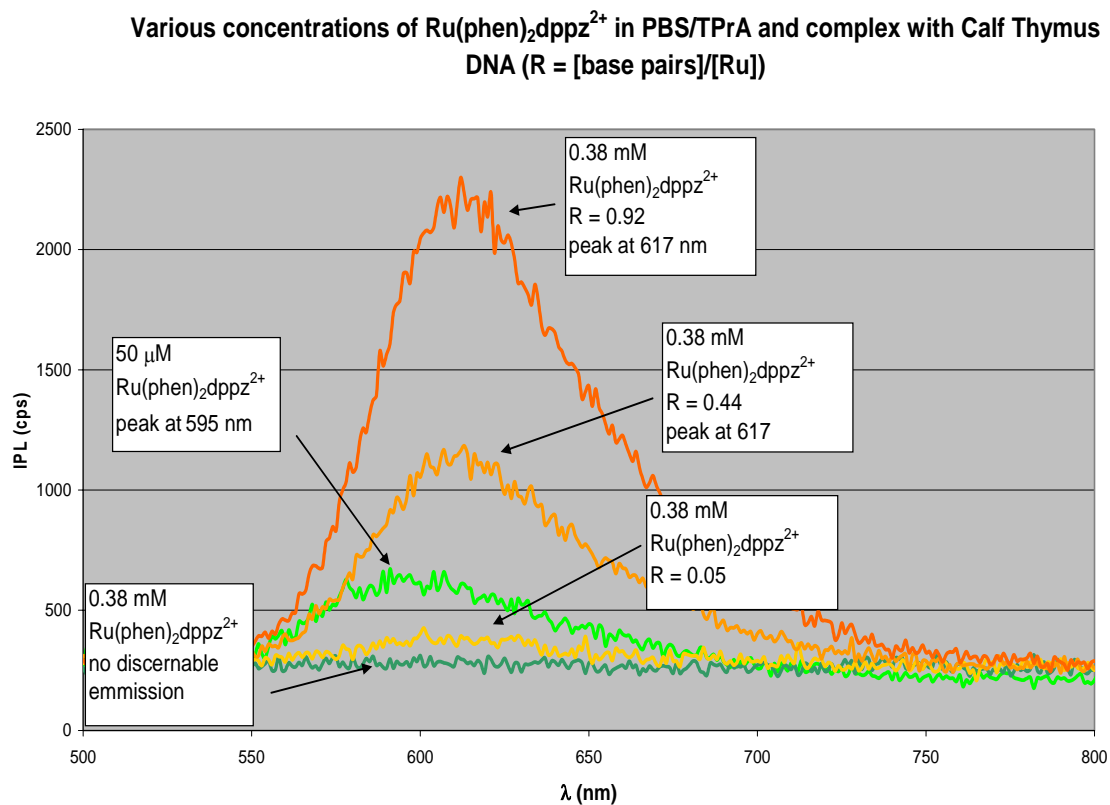
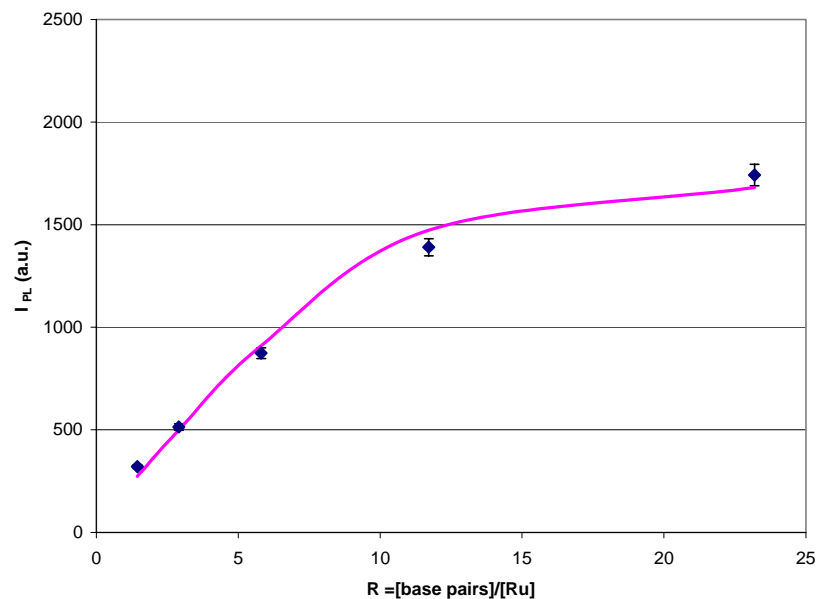


Figure 4-6. To emphasize the low grade emission is from a trisphen impurity, calf thymus DNA is titrated into a solution of the lab-synthesized $\text{Ru}(\text{phen})_2\text{dppz}(\text{BF}_4)_2$. Note how the addition of DNA causes the emission to shift from the trisphen characteristic wavelength to that of the dppz modified complex in acetonitrile.

Here, $\epsilon_{f,b}$ are the molar extinction coefficients of $\text{Ru(phen)}_2\text{dppz}^{2+}$ free and bound (intercalated) at the wavelength of excitation (440 nm) and were found to be essentially the same at $18200 \text{ M}^{-1} \text{ cm}^{-1}$. Further, $\phi_{f,b}$ are the quantum yields of the free and bound specie, determined absolutely by Olofsson et al.⁸ Since the values reported were for the separate Δ and Λ enantiomers, average values for the racemic mixture were determined to be 0.043 when bound to dA-dT, 0.04 when bound to CT DNA and 0.00093 for the free complex. Cb and Ct refer to the bound and total complex concentration and Kb the binding constant. Finally, NP refers to nucleotide phosphate concentration, which is twice the base pair concentration used in our 'R' value.

The plots of PL intensity are presented in Figure 4-6 along with the fitted curves. Good fits were obtained by using a non-linear least squares approach in Excel[®] as outlined by Harris.⁹ Kb values were $2.5 \pm 0.1 \times 10^7$ and $2.6 \pm 0.2 \times 10^6$ for CT DNA and 20-mer poly dA-dT respectively and binding site sizes (s) were 2 and 10. The magnitude of the obviously strong binding was in good agreement with that found by Barton et al. in ref 1. Of note, there was an order of magnitude difference between the two different polynucleotides. This is possibly due to the flexible conformations possible with the CT DNA vs. the relatively rigid 20-mer short chains. This binding difference was also evident in the different shapes of the two PL data curves. This difference – less intensity for the shorter helices was also seen in studies by Barton et al. on 28-mer random sequence fragments.⁸

Kb fitting of 20-mer PL data (1 μ M Ru(phen)₂dppz²⁺ in 0.1 M PBS, pH 7.5)



Kb fitting from CT DNA PL data (1 μ M Ru(phen)₂dppz²⁺ in 0.1 M PBS pH 7.5)

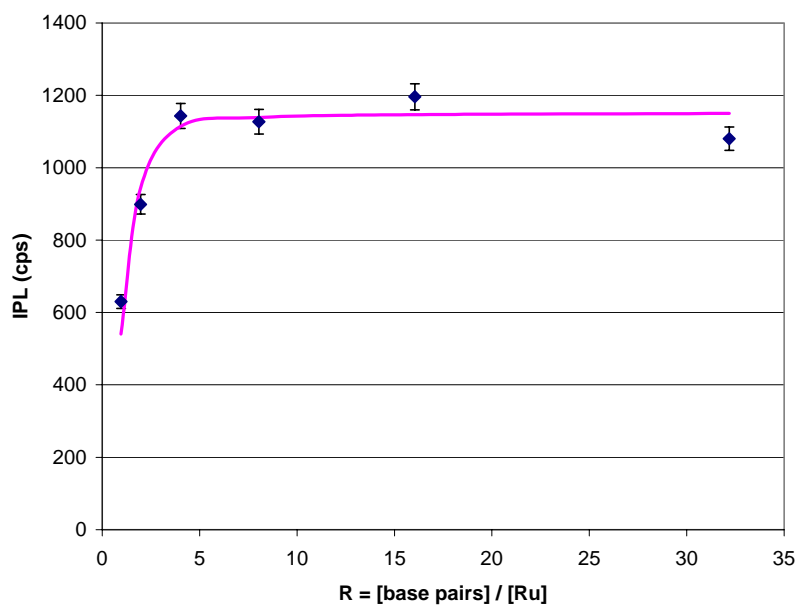


Figure 4-7. Two parameter (binding constant and binding site size) fit of fluorescence data with two different polynucleotide types.

-
- ¹ Hartshorn, R., Barton, J., *J. Am. Chem. Soc.*, **1992**, *114*, 5919-5925.
- ² Olson, E., Hu, D., Hormann, A., Honkman, A., Arkin, M., Stemp, E., Barton, J., Barbara, P., *J. Am. Chem. Soc.*, **1997**, *119*, 11458-11467.
- ³ Balzani, V., Juris, A., Barigelletti, F., Campagna, S., Belser, P., Von Zelewsky, A., *Ru(II) Polypyridine Complexes: Photophysics, Photochemistry, Electrochemistry, and Chemiluminescence*, Elsevier Science Publishers, **1988**, p. 177.
- ⁴ Barigelletti, F., Juris, A., Balzani, V., Belser, P., von Zelewsky, A., *Inorg. Chem.*, **1987**, *26*, 4115-4119
- ⁵ Balzani, V., Juris, A., Barigelletti, F., Campagna, S., Belser, P., Von Zelewsky, A., *Ru(II) Polypyridine Complexes: Photophysics, Photochemistry, Electrochemistry, and Chemiluminescence*, Elsevier Science Publishers, **1988**, p. 135.
- ⁶ Liu, Y., Bhouai, A., Degtyareva, N., Lutterman, D., Dunbar, K., Turro, C., *J. Am. Chem. Soc.*, **2005**, *127*, 10796-10797.
- ⁷ Parker, C.A., *Photoluminescence of Solutions*, Elsevier Publishing, **1968**, p. 20.
- ⁸ Olofsson, J., Wilhelmsson, L., Lincoln, P., *J. Am. Chem. Soc.*, **2004**, *126*, 15458-15465.
- ⁹ Harris, D., *J. Chem. Ed.*, **1998**, *75*, 119-121

Chapter 5 ECL of the Unbound Complex

Characteristics of the ECL

ECL of the unbound complex with a co-reactant proceeded much like other ruthenium complexes of this type by producing light once both the complex and co-reactant (tripropylamine or oxalate) were oxidized (Figure 5-1). The first broad wave of faradaic current seen in Figure 5-1 was the oxidation of TPrA or oxalate and did not produce light which is indicative of the typical co-reactant mechanism.¹ Once the oxidation peak of the complex appeared, light was generated. As was discussed in Chapter 3, this peak was difficult to see due to the poor solubility of the complex in water. Another feature particular to this method of light generation was the peak structure of the PMT current which looks very much like a diffusion controlled, irreversible current response. This emphasized the semi-infinite, planar diffusional nature of how the reactants come in contact with one another to produce the excited state in an ECL experiment.²

To get a feel for how intense the ECL was compared to complexes in the family, data was obtained for $\text{Ru}(\text{bpy})_3^{2+}$ and $\text{Ru}(\text{phen})_3^{2+}$ and shown Figure 5-2. Though $\text{Ru}(\text{phen})_2\text{dppz}^{2+}$ is a poor ECL compound compared to its homoleptic cousins, its PL in water was non-existent, which indicated its ECL efficiency is quite good. That is, since the ECL efficiency is the product of the PL quantum yield and electrochemically produced excited state efficiency,³ differences in the intensity of $\text{Ru}(\text{phen})_2\text{dppz}^{2+}$ ECL to

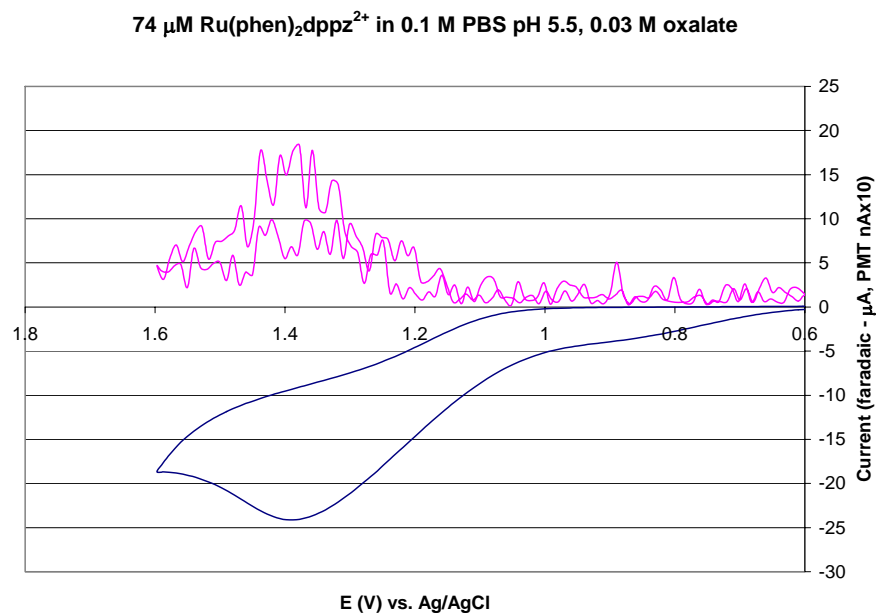
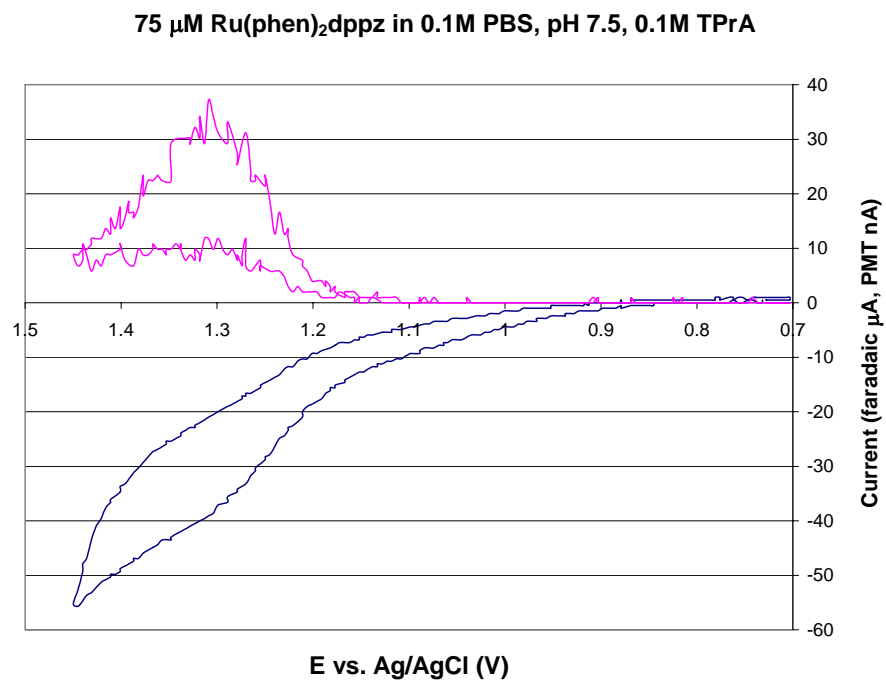


Figure 5-1. The ECL intensity of equimolar amounts of complex with two different co-reactants at a Pt disk electrode. Note the intensity with oxalate has been multiplied by 10. Scan rate was 200 mV/s.

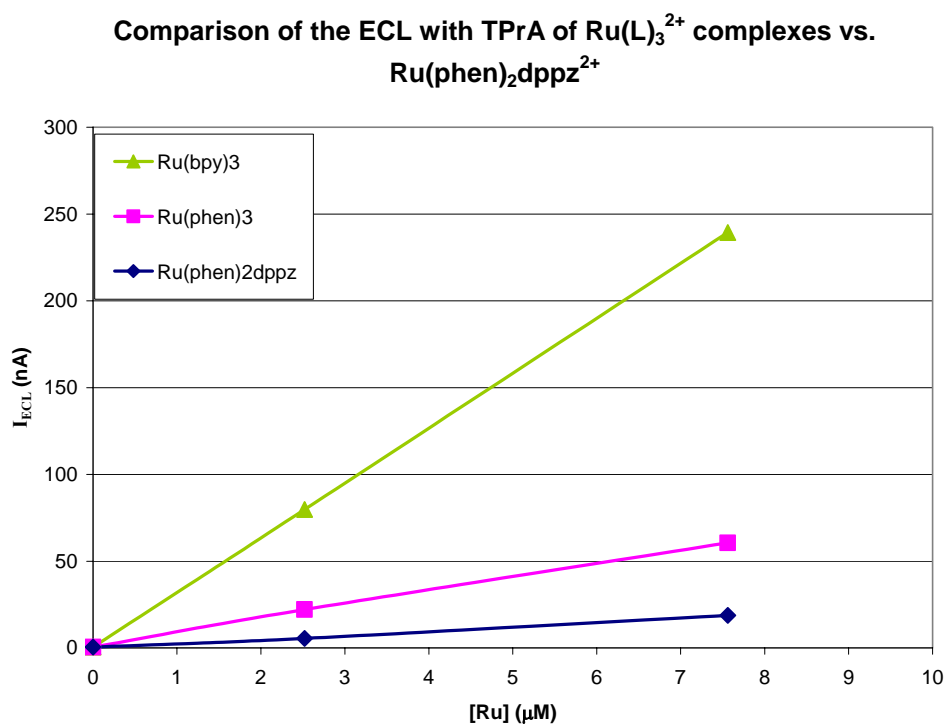


Figure 5-2. Comparison of the ECL of common ruthenium based complexes and $\text{Ru}(\text{phen})_2\text{dppz}^{2+}$. Reaction conditions were 0.1 M PBS and tripropylamine, pH 7.5, at a Pt disk electrode.

these other compounds can be attributed to differences of their quantum yields in water. A more rigorous treatment of this aspect will be found in Chapter 6.

The spectrum of light produced in the TPrA system is shown in Figure 5-3 and was similar to the PL spectrum seen in acetonitrile as shown in Chapter 4 and thus the two represent the same emitting state. While the peak was somewhat broader in the spectrum derived from the ECL experiment, this is not atypical since a wider slit width is generally used in ECL experiments due to smaller amounts of light production. The peak intensity of light generated by ECL for $\text{Ru}(\text{phen})_2\text{dppz}^{2+}$ plotted linearly vs. concentration from 1 to 100 μM with an average statistical deviation of 5% at each point as shown in Figure 5-4. This indicated the expected pseudo first order process since the TPrA concentration was held in large excess *vis a vis* the complex.

These findings beg the question: why would the electrogenerated-chemically produced excited state generate light so much more effectively than the light induced one? The consensus is that light emission from $\text{Ru}(\text{phen})_2\text{dppz}^{2+*}$ comes from the π^* orbital localized on the phenazine nitrogens. These are the bridging nitrogens extending from the back of the phenanthroline moiety. The energy of these orbitals is lowered to a dark or non-emissive state in water by specific hydrogen bonding to both of these nitrogens. This was shown schematically in Figure 1-2. The quenching process in water has been studied extensively by the Lincoln and Barton groups, and they have shown the hydrogen bonded dark state is accessed via the excited state not the ground state since the phenazine nitrogens are not basic enough in the ground state to hydrogen bond with water. Thus the quenching occurs as a step-wise process that occurs only after the phenazine-localized excited state is produced.

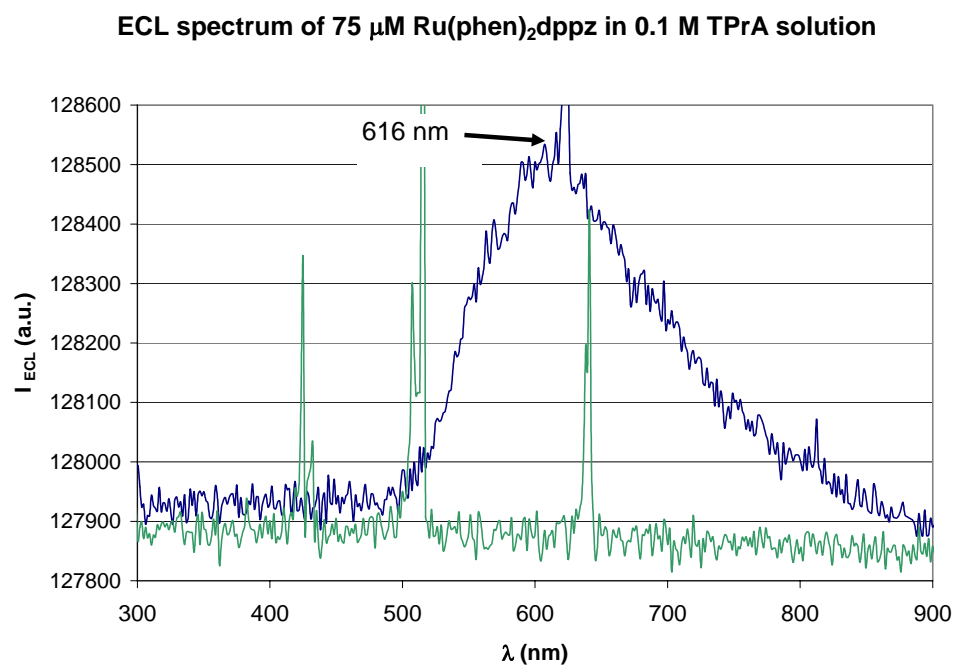


Figure 5-3. The ECL spectrum of Ru(phen)₂dppz(BF₄)₂ with tripropylamine as co-reactant in phosphate buffer, pH 7.5. The response with no tripropylamine (green) has been included as the blank. The noise spikes are gamma ray background.

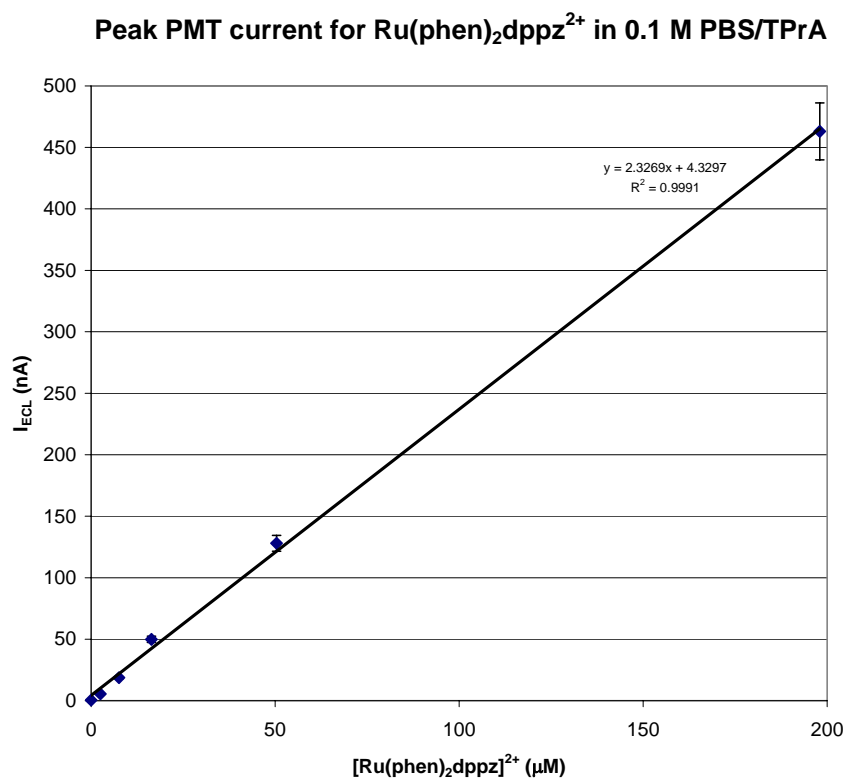


Figure 5-4. A calibration curve of the peak ECL intensity of $\text{Ru}(\text{phen})_2\text{dppz}(\text{BF}_4)_2$ in the indicated solvent conditions. The peak PMT current produced was taken from triplicate measurements (run in separate solutions) of a single anodic sweep as seen in Figure 5-1. The electrode was polished with 0.5 micron alumina slurry and sonicated in ethanol for 5 minutes between each run. The Pt electrode had an area of 0.013 cm².

As has been established by spectroscopic studies⁴ and computational work,⁵ $\text{Ru}(\text{phen})_2\text{dppz}^{2+}$ emits around 620 nm by PL when in aprotic solvents and intercalated into a polynucleotide chain where hydrogen bonding is interrupted or blocked. Furthermore, $\text{Ru}(\text{phen})_2\text{dppz}^{2+}$ also emits around 620 nm by ECL in pure buffer with TPrA or buffer/TPrA with acetonitrile, but is more intense in the mixed solvent where hydrogen bonding would occur less frequently. In ref 6, it is shown that the PL of $\text{Ru}(\text{phen})_2\text{dppz}^{2+}$ in water was excruciatingly small and occurred around 800 nm. Therefore, since the ECL emission in water was at 620 nm, the ECL originated from two possibilities: (1) the impurity discussed in Chapter 4 or (2) a process in the ECL mechanism that disrupts hydrogen bonding on a time scale long enough for emission to occur first.

ECL and the Impurity

Once it became apparent there was an impurity remaining from the synthesis, an immediate question arose as to the source of the ECL light produced. Even though there is good evidence the impurity is small, this is not an unreasonable question since ECL with $\text{Ru}(\text{bpy})_3^{2+}$ has been shown as low as 10 nanomolar.⁶ The spectroscopic results from Chapter 4 showed the light switch effect, which meant the target complex is present in good concentration, however, ECL from $\text{Ru}(\text{phen})_2\text{dppz}^{2+}$ had never been studied and the light switch behavior that makes this complex interesting says the excited state in water should be quenched. ECL from analogous ruthenium complexes usually shows PL and ECL to originate from the same excited state⁷ so very little ECL of the free complex was expected. While certainly showing the lowest light intensity of the group, the dppz analogue is still roughly a third as intense of trisphen at

equimolar concentrations. However, a rough estimate of the impurity is thought to be 1% based on the discussion and data in Chapter 4.

A more direct approach to answer the question compared the ECL response of Ru(phen)_3^{2+} at a concentration of 1% of $\text{Ru(phen)}_2\text{dppz}^{2+}$ in similar co-reactant conditions. This experiment provided the answer as to which species was responsible for the light produced. Figure 5-5 shows this experimental comparison. Buffer solution and tripropylamine concentrations were the same in each separate experiment.

As evidenced, only about 10% of the light produced could be attributed to a 1% trisphen impurity – the rest must be from the dppz modified complex.

Additionally, since the light generated by ECL and PL are from the same state, light produced by $\text{Ru(phen)}_2\text{dppz}^{2+}$ would increase in intensity when going to a mixed solvent that has less water since water is a quencher.⁸ This is borne out by the results of $\text{Ru(phen)}_2\text{dppz}^{2+}$ ECL in acetonitrile:water studies. When comparing Figure 5-1 to Figure 5-7 there was an almost ten fold increase in ECL intensity in a acetonitrile:water mixture even though the complex and co-reactant concentrations were less. That kind of solvent would have an opposite effect on a Ru(phen)_3^{2+} system, as evidenced in Figure 5-6. Photoluminescence for equimolar amounts of trisphen was less in acetonitrile than in an aqueous environment. Finally, trisphen emission, as shown in Chapter 4, occurs at 595 nm but ECL of our $\text{Ru(phen)}_2\text{dppz}^{2+}$ was shown to occur at 617 nm in Figure 5-3. Thus, trisphen emission can only be a minor component of the light seen in the ECL experiment.

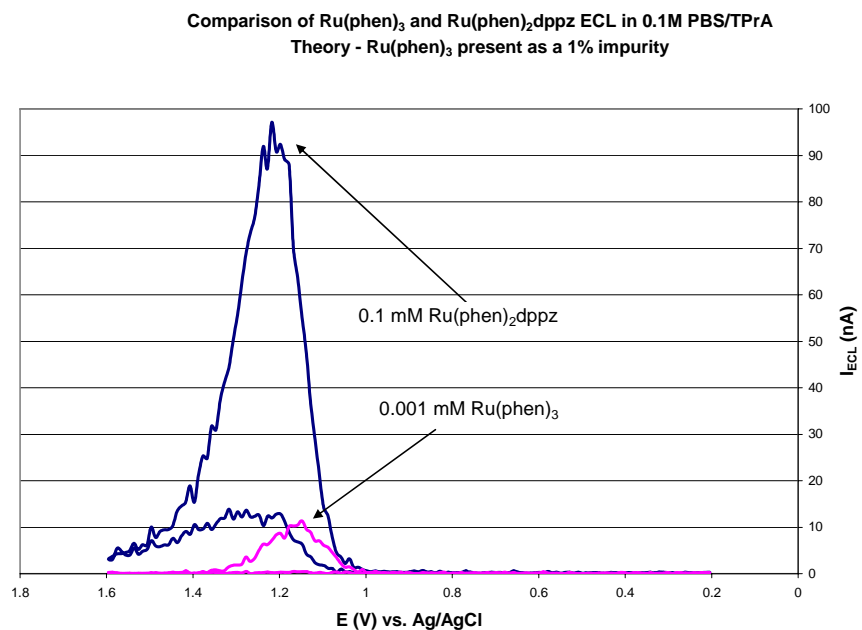


Figure 5-5. Two separate ECL experiments run under the same conditions. The blue trace is the lab-synthesized 0.1 mM Ru(phen)₂dppz(BF₄)₂ and the magenta trace is commercial trisphen ECL at 1% of the concentration. This shows conclusively that even a 1% trisphen impurity can only account for 10% of the light produced and thus the rest must come from the dppz modified complex.

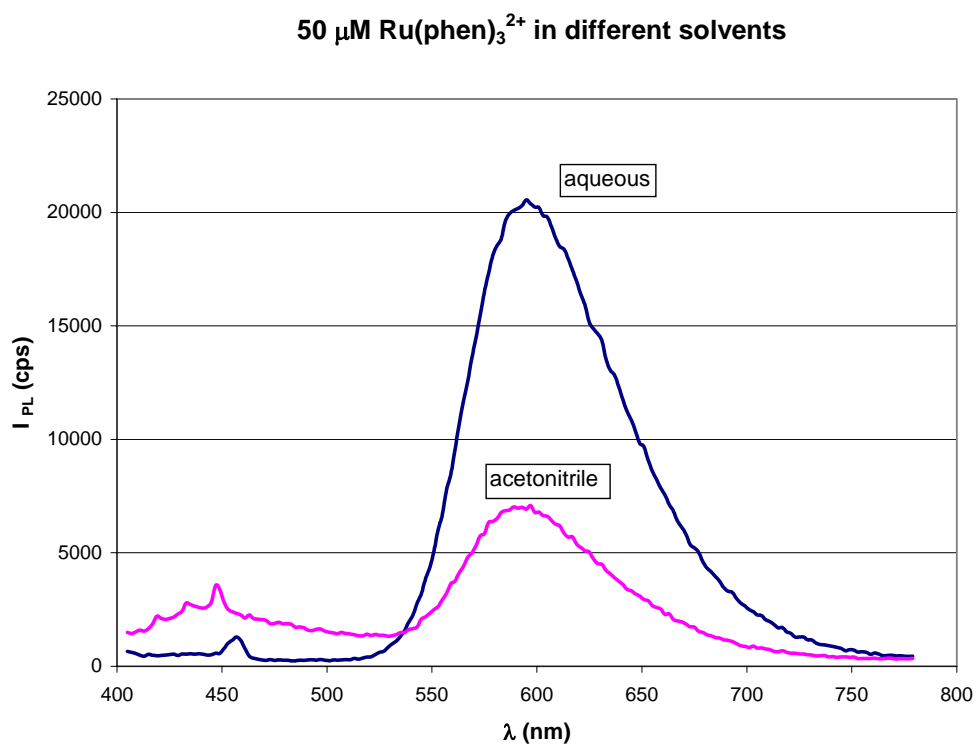


Figure 5-6. The fluorescence of equimolar solutions of commercial trisphen in the indicated solvents. Interestingly, this complex emits more intensely in water.

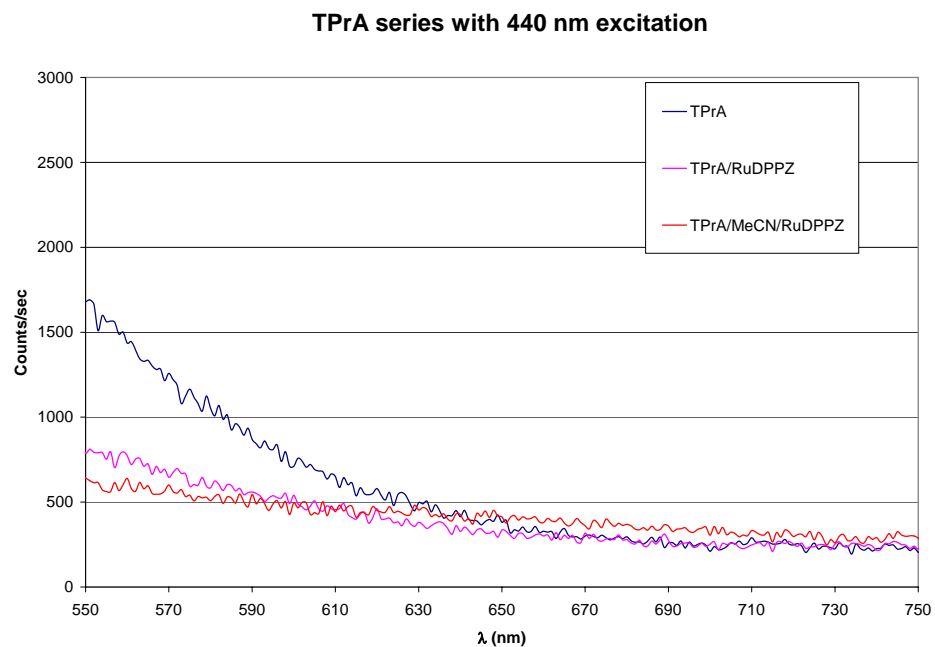


Figure 5-7. Fluorescence in water of various component related to the study. Note that merely adding tripropylamine to the solvent does not induce the light switch effect.

The Role of Tripropylamine

That leaves the ECL-specific mechanism as the likely answer as to why this compound showed significant ECL in water but not PL. To unravel why there is such a marked difference in the light made in the two different kinds of experiments, a comparison of the two must be undertaken, and in their difference the answer found. First of all, the ECL experiment has TPrA present – a very nonpolar molecule. Initially, one might think non-specific interactions of TPrA in the solvent shell around the complex may interfere with hydrogen bonding to an extent and allow light to be made as is the case with acetonitrile. However, PL experiments in the same PBS/TPrA solution as in the ECL experiment showed the same quenching. In fact, tripropylamine is itself a quencher. Figure 5-8 shows a Stern-Volmer plot of $\text{Ru}(\text{phen})_2\text{dppz}^{2+}$ fluorescence in acetonitrile with varying amounts of the co-reactant. A linear plot revealed the K_{SV} to be 48.5 M^{-1} . When compared to proton donor quenchers studied by Barton⁹, TPrA has a quenching constant about half that of 2-nitrophenol and 2-chlorophenol at $2.8 \times 10^8 \text{ M}^{-1}\text{s}^{-1}$ when using a lifetime in acetonitrile of 170 ns. Barton ruled out quenching of $\text{Ru}(\text{phen})_2\text{dppz}^{2+*}$ via electron transfer and energy transfer quenching mechanisms by conducting control studies with compounds of similar energy levels and redox properties, but which were not proton donors. These included p-dimethoxybenzene, chlorobenzene, 2-chlorobenzene, and others. None were quenchers. Interestingly, saccharin was the only amine studied and it had a quenching constant of 8.2×10^8 . There was also no correlation between pKa and quenching ability over the range of organic proton donors studied (4.8 to 11.7 – TPrA is 10.6 from ref 10). Thus, TPrA is an average quencher and may be added to the list of proton donors that quench the excited state of $\text{Ru}(\text{phen})_2\text{dppz}^{2+}$ in acetonitrile.

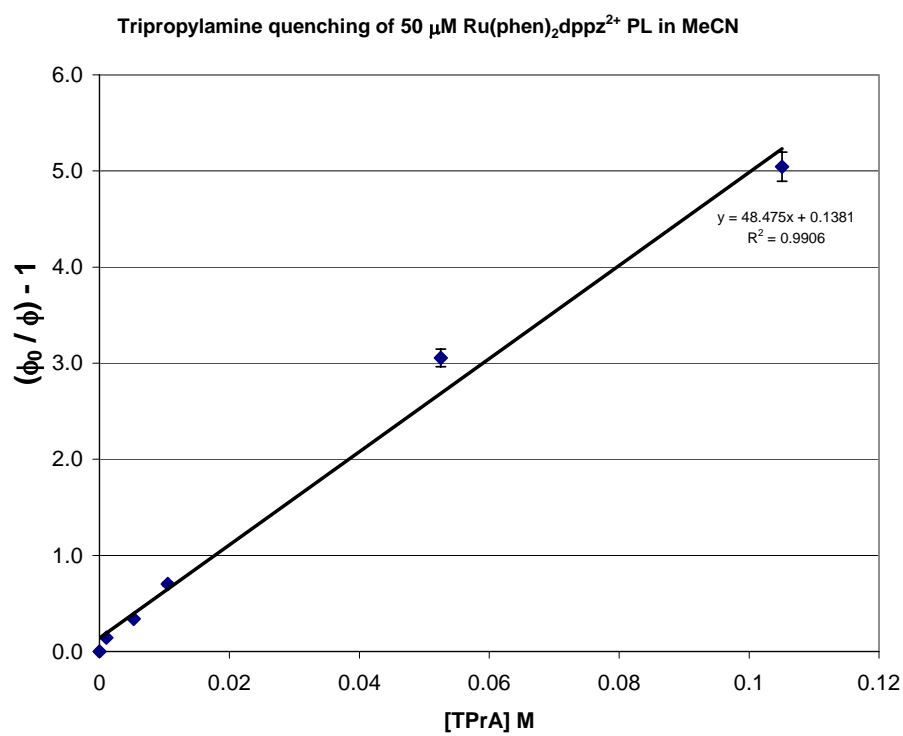


Figure 5-8. Stern-Volmer plot showing quenching of the fluorescence of $\text{Ru}(\text{phen})_2\text{dppz}(\text{BF}_4)_2$ by tripropylamine.

However, it is not TPrA that accomplishes the electron transfer responsible for the excited state in $\text{Ru}(\text{phen})_2\text{dppz}^{2+*}$, rather the TPrA radical which has already ejected a proton. In fact, once the electron transfer to the complex takes place, the product is the cation, TPrA^+ . Since the phenazine nitrogens are basic enough in the excited state to hydrogen bond, then perhaps electrostatic attraction with the cation disrupts hydrogen bonding long enough for emission. Certainly, the molecule is inside the solvent shell in order to accomplish electron transfer; otherwise, the PL experiments with TPrA in the buffer would have shown some light switch effect. According to Barbara in ref 8, the timescale for emission from the non-hydrogen bonded state (the one responsible for emission at 620 nm) is 3 ps while the time required to convert to the dark state is 10 ps. Thus the interruption only has to last a few picoseconds for emission to occur.

Oxalate Results

The idea of tripropylamine leading to $\text{Ru}(\text{phen})_2\text{dppz}^{2+}$ emission in water due to electrostatic interactions while acting as the electron transfer agent is bolstered by the oxalate results. As Carter found, the light produced when using tripropylamine (TPrA) as a co-reactant was greater than when using oxalate.¹⁰ In fact, the TPrA produced 6.5 times more light with $\text{Ru}(\text{phen})_2\text{dppz}^{2+}$ than oxalate when the two sets of data were normalized to co-reactant concentration, and the pH optimized for each system. This is, however, a much larger difference than the roughly 20% Carter saw when comparing the ECL of trisphen bound to calf thymus DNA when using each of the two co-reactants. In his experiment, the difference in light production between the co-reactants is attributed to electrostatic effects of the reacting species.

In the case of oxalate, the reactant is the carbon dioxide anion radical (Eq. 1-2)¹¹ whereas TPrA is an uncharged radical (Eq. 1-7).¹² The Carter comparison was being made for intercalated trisphen, where the negatively charged phosphate backbone of the helix has a significant effect due to its proximity to the bound complex. In the case of oxalate and $\text{Ru(phen)}_2\text{dppz}^{2+}$, electrostatic repulsion between the anion and the higher electron density found on the phenazine nitrogens would repel the electron transfer product away and allow hydrogen bonding to occur. This makes the dark state accessible inside the timescale of emission. Contrast this with the positively charged product (TPrA+) in the TPrA experiment. It would show some electrostatic attraction to the ligand post electron transfer, and would therefore interrupt hydrogen bonding to the excited state.

Thus, in the specific case of $\text{Ru(phen)}_2\text{dppz}^{2+}$ ECL with tripropylamine, even though the excited state produced by ECL was the same as in the PL experiment as evidenced by the emission wavelength, the environment around the complex was different. This gave rise to emission in water that was not seen in the PL experiment due to the unique nature of the ECL experiment. Specifically, that aspect of the experiment that required the close proximity needed for electron transfer, which led to a different outcome based on the electron transfer agent.

-
- ¹ Zu, Y., Bard, A., *Anal Chem.*, **2000**, *72*, 3223-3232.
- ² Bard, A., Faulkner, L., *Electrochemical Methods*, John Wiley & Sons, New York, NY, **2001**; p. 237.
- ³ Knight, A., Greenway, G., *Analyst*, **1994**, *119*, 879-890.
- ⁴ Hiort, C., Lincoln, P., Norden, B., *J. Am. Chem. Soc.*, **1993**, *115*, 3448-3454.
- ⁵ Fantacci, S., De Angelis, F., Sgamellotti, A., Marrone, A., Re, N., *J. Am. Chem. Soc.*, **2005**, *127*, 14144-14145.
- ⁶ Miao, W., Choi, J., Bard, A., *J. Am. Chem. Soc.*, **2002**, *124*, 14478-14485.
- ⁷ Knight and Greenway.
- ⁸ Olson, E.J.C.; Hu, D.; Hormann, A.; Honkman, A., Arkin, M., Stemp, E., Barton, J., Barbara, P., *J. Am. Chem. Soc.*, **1997**, *119*, 11458-11467.
- ⁹ Turro, C., Bossmann, S., Jenkins, Y., Barton, J., Turro, N., *J. Am. Chem. Soc.*, **1995**, *117*, 9026-9032.
- ¹⁰ Carter, M., Bard, A., *Bioconjugate Chem.*, **1990**, *1*, 257-263.
- ¹¹ Kanoufi, F., Bard, A., *J. Phys. Chem. B*, **1999**, *103*, 10469-10480.
- ¹² Kanoufi, F., Zu, Y., Bard, A., *J. Phys. Chem. B*, **2001**, *105*, 210-216.

Chapter 6 ECL with Polynucleotides

From the beginning of this project, the central question was would $\text{Ru}(\text{phen})_2\text{dppz}^{2+}$ exhibit light switch behavior in ECL as it does in PL. Upon observing the ECL described in Chapter 5, very large amounts of light would be required upon intercalation to be able to label the complex a light switch when using ECL. Also, diffusional effects upon intercalation and the subsequent degradation of ECL as Carter showed were known to be a possibility. Initial experiments demonstrated that the measures taken to improve reproducibility in light measurements with the free complex were not sufficient when adding either calf thymus DNA or the 20-mer poly dA-dT. At times, deviations of 100% were seen from one trial to the next. Also, after numerous efforts failed, a flow cell and a technique called PAD were employed

Pulsed Amperometric Detection (PAD)

This technique was pioneered over two decades ago to reliably make electrochemical measurements of organic molecules of interest, like sugars, since they tend to foul electrodes on oxidation.¹ In fact, the technique was eventually employed as a detector at the end of chromatography columns. The details of the technique are described in Chapter 2, and the plot of current vs. time of a PAD experiment is shown in Figure 6-1. The key part of the technique that led to such improvements in reproducibility was the extreme steps in potential. On the positive side, was a step to oxygen evolution by oxidizing water followed immediately by an extended step to hydrogen evolution by water reduction. The steps clean organic oxidation products off

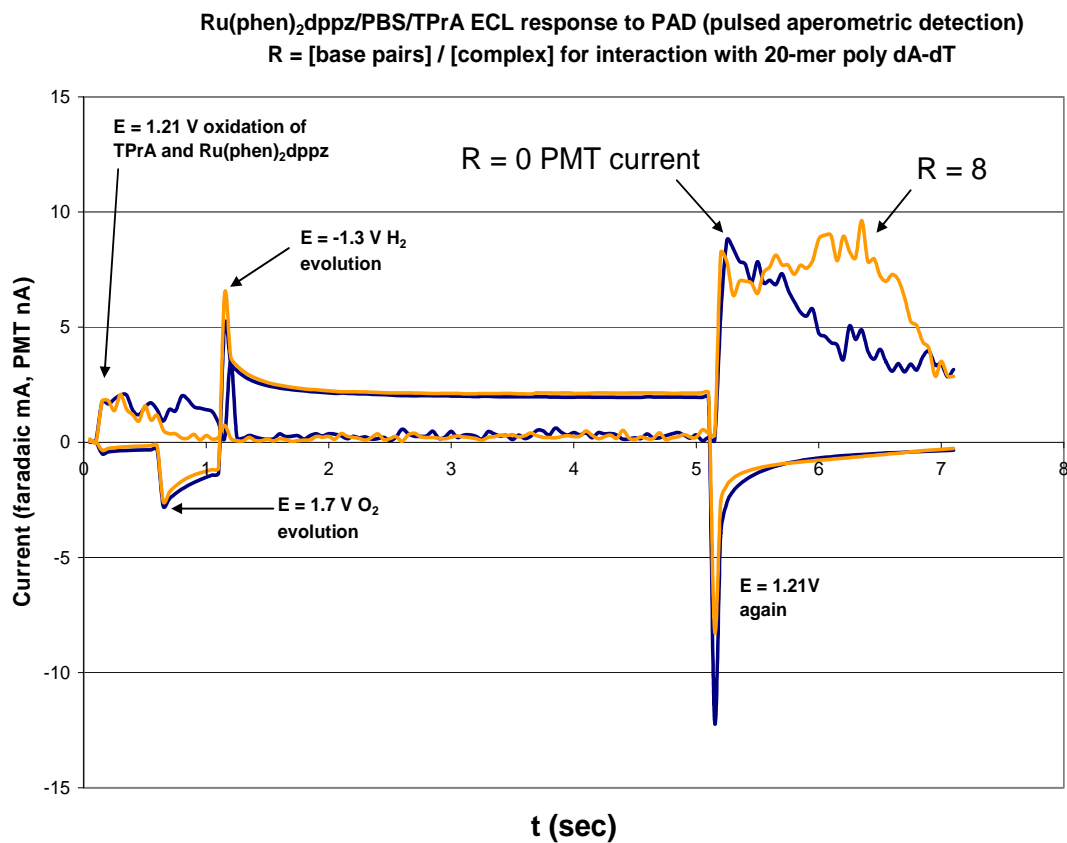


Figure 6-1. Faradaic and photomultiplier response using pulsed amperometric detection (PAD) for ECL of Ru(phen)₂dppz(BF₄)₂ with tripropylamine. The blue trace is without polynucleotide present and the orange trace is after addition of 20-mer poly dA-dT. R = [base pairs] / [Ru].

the electrode surface without mechanical manipulation, such as polishing, that changes the electrode's roughness. While our use of the technique here sampled the analytical signal at a different point than the original work described in ref 1, the potential profile proved a reliable way to prepare the electrode surface the same way each time. The deviations in peak light detected fell to around 5% for the 20-mer experiments and 17% for CT DNA.

Use of EDTA Buffer

Due to its common use as a buffer in biologically based assays, ECL was initially studied in a buffer of EDTA (ethylenediaminetetraacetic acid) and Tris (tris(hydroxymethyl)amino methane). Using the concentrations recommended by the manufacturer for a calf thymus DNA solution (0.1 M EDTA, 10 mM Tris), the pH was 5.5. While this was optimum for oxalate as a co-reactant,² it resulted in only 20% of the maximum light yielded with tripropylamine.³ However, the ECL intensity in this buffer was much less than that shown in Figure 6-1. Though a better ECL performer than oxalate, the Tris results were, in fact an order of magnitude less than what would be expected based solely on not optimizing the pH, and the complex of interest certainly did not show a light enhancement upon intercalation.

In an effort to unravel the poor ECL performance of $\text{Ru}(\text{phen})_2\text{dppz}^{2+}$ /DNA in EDTA/Tris buffer, a series of ECL experiments using the PAD profile were performed with the much better understood $\text{Ru}(\text{bpy})_3^{2+}$ and no DNA. Since Tris is also an amine like TPrA, the first experiment used it alone with $\text{Ru}(\text{bpy})_3^{2+}$, and it proved to be a weak co-reactant. Interestingly, light was not produced until stepping the potential to 1.7 V vs. Ag/AgCl, showing Tris was not oxidized prior to the metal complex like TPrA. Attempts to observe its oxidation via cyclic

ECL of $\text{Ru}(\text{phen})_2\text{dppz}^{2+}$ in 0.1 M EDTA, 10 mM Tris, 0.13 M TPrA
 (0.1 M PBS/TPrA data added for comparison)

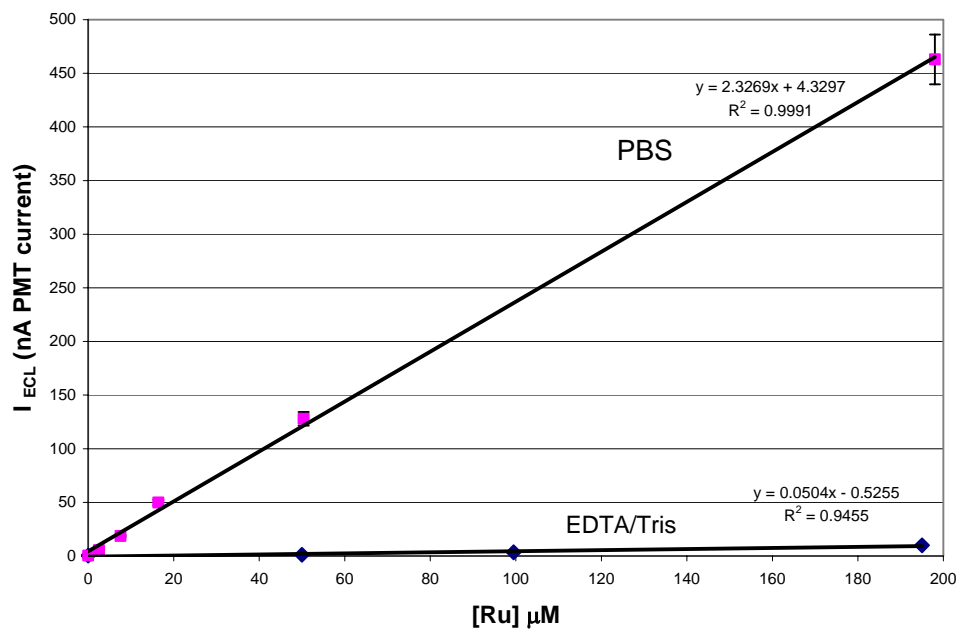


Figure 6-2. A comparison of ECL intensity in an EDTA/Tris buffer compared to phosphate buffer, showing the effective quenching of ECL. Both are at pH 7.5.

voltammetry only showed a single, broad, featureless wave. Upon addition of tripropylamine, the typically strong ECL response was seen as a kinetically fast spike at the switch from the first oxidation step to the far negative potential and after the second oxidation step. The light production at the negative potential was also seen in the Tris only experiment but was kinetically much slower. Both of these indicated annihilation of the Ru (I) and (III) species typical of non-aqueous investigations. Incidentally, the light generated in this experiment was almost three times more intense than an equivalent experiment in phosphate buffer. This indicated that a combination of the two amines stabilizes the Ru (III) species. Finally, addition of EDTA showed rapid initial light production that was promptly quenched. This occurred at both the negative pulse and the final positive pulse. All data is shown in Figure 6-3.

Since EDTA has been used previously as a sacrificial electron donor in photochemical experiments, it might act accordingly in the ECL quenching mechanism.⁴ However, EDTA was oxidized before $\text{Ru}(\text{bpy})_3^{2+}$ (0.4 V and 1.29 V vs. SCE respectively)²⁴, so there was a possibility the quenching was due to an interaction with the co-reactant, TPrA, instead. Efforts to find previous work with EDTA quenching of $\text{Ru}(\text{bpy})_3^{2+}$ PL proved fruitless, so a simple fluorescence quenching experiment was undertaken. A Stern-Volmer plot showed no discernible trend that would indicate a standard bi-molecular quenching of the metal complex, leaving interaction with the co-reactant the only possibility left. Consequently, use of the EDTA/Tris buffer was discontinued, and the phosphate buffer (PBS) used for all other aqueous electrochemical experiments in this work.

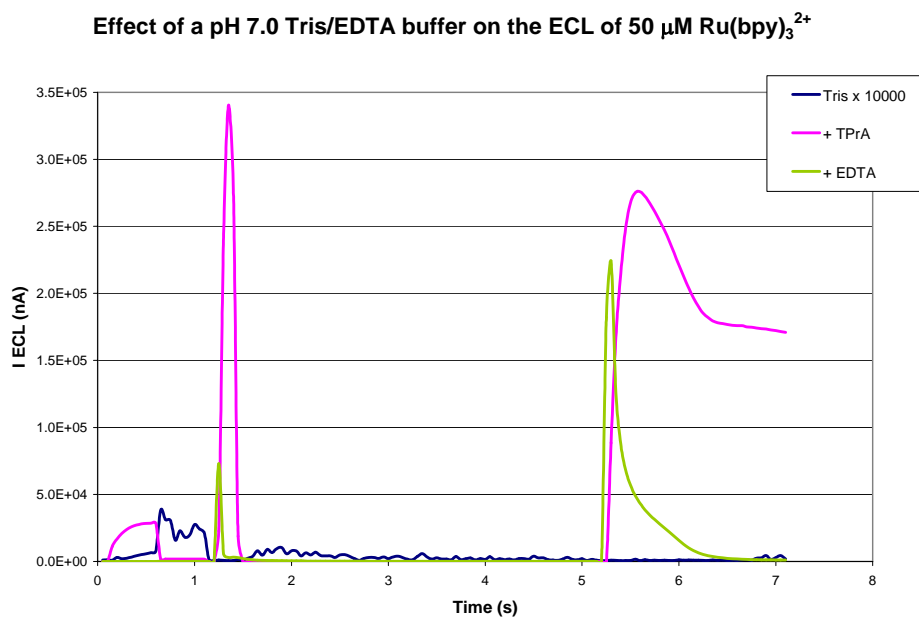


Figure 6-3. Using the PAD profile to unravel the effects of the EDTA/Tris buffer on ECL performance. The blue trace is $\text{Ru}(\text{phen})_2\text{dppz}(\text{BF}_4)_2$ with Tris only, the magenta trace after tripropylamine addition, and the green trace upon further addition of EDTA.

Fitting ECL with Polynucleotides Data

Efforts to model the system as have been published previously⁵ proved more complex, since light is enhanced upon intercalation which is not the case for the other compounds studied. The successful strategy proved to be using the PL data to obtain the binding constants and binding site size as discussed in Chapter 4 and using published values for quantum yield. With this information in hand, ECL efficiencies were determined for Ru(phen)₂dppz²⁺ intercalated into the two different types of polynucleotides, calf thymus DNA and 20-mer poly dA-dT.

Since Ru(phen)₂dppz²⁺ shows appreciable ECL without DNA present, the approach to fit this data was modified to a normalized equation as follows:

$$I(R) = D_f C_f \phi_{f, PL} \phi_{f, ecl} + D_b C_b \phi_{b, PL} \phi_{b, ecl} \quad \text{Eq. 6-1}$$

But

$$I(0) = C_t \phi_{f, ecl} \quad \text{Eq. 6-2}$$

so

$$I(R) / I(0) = (1 - \chi b) + \chi b D_f \phi_{b, PL} \phi_{b, ecl} / D_b \phi_{f, PL} \phi_{f, ecl} \quad \text{Eq. 6-3}$$

Where $D_{f,b}$ are the free and bound diffusion coefficients and the ECL efficiencies are explicitly written separately from the quantum yields.⁶ D_f was derived from the acetonitrile experiments and Eq. 7-2, so it will be a decent estimate. The D_b values used were those determined voltammetrically by Thorp, though the CT DNA value will vary since we did not sonicate it prior to use.⁷ χb is the mole fraction of bound complex and was determined using Eq. 4-2 and the previously determined K_b 's.

Figure 6-4 shows the ratio of light produced with poly dA-dT and CT DNA to light without any polynucleotide present along with the best fits using Eq. 6-3 and Excel[®] again. The

significant enhancement of light upon intercalation was evident when compared with the data of $\text{Ru}(\text{phen})_3^{2+}$ ECL (which behaved similar to $\text{Os}(\text{bpy})_3^{2+}$) discussed in ref 5. In those experiments, the light produced decreased non-linearly upon DNA addition with the steepest portion occurring at the beginning. To obtain the best fit for this data, estimates were used for the ECL efficiencies, and Solver[®] was told to minimize the squares of the vertical deviations (as in the PL data) by varying these efficiencies. Interestingly, the free efficiency was near 100% as was the case with $\text{Ru}(\text{bpy})_3^{2+}$ shown in ref 6.

However, the bound ECL efficiencies of $\text{Ru}(\text{phen})_2\text{dppz}^{2+}$ were quite poor with the 20-mer poly dA-dT and CT DNA being 7% and $\ll 1\%$ respectively. While the 20-mer ECL data fit well with the binding site size derived from the PL data, the CT DNA data did not. Initial fits allowing only the efficiencies to vary gave poor results. When the binding site size was allowed to change as well, the shown fit was obtained though the site size changed dramatically from 2 to 44. This was indicative of the diffusional nature of the ECL experiment over the PL dynamics and the large polymer characteristics of CT DNA over the 20-mer. Thus, polynucleotide binding must have a negative effect on the ECL of the complex, since it is known the PL efficiency goes up tremendously upon intercalation of the $\text{Ru}(\text{phen})_2\text{dppz}^{2+}$.

This negative effect was due to two primary effects, the first of which was diffusion. The CT DNA used in this study was not sonicated into smaller fragments so it is easy to see its diffusion coefficient will be at least an order of magnitude less based on molecular weight alone. Additionally, Nunez et al.⁸ have shown that DNA has significant conformational changes when intercalated. Since it tends to curl up into a ball, this could conceivably slow the rate of diffusion of the TPrA radicals getting to intercalation sites on the interior. This idea was bolstered by the improved results when using 20-mer where the polynucleotide remained almost rigid.⁶ Thus,

while the emission efficiency was improved by intercalation, other dynamics were in play in the ECL experiment that precluded a light switch effect in ECL upon intercalation. However, given the light switch improvement in emission was $> 10^3$ as shown in Chapter 4, a one order of magnitude decrease in diffusion alone did not account for the lack of ECL intensity improvement. The next chapters will attempt to explain the additional phenomenon that is taking place which precluded an ECL light switch.

**ECL of 1 μ M Ru(phen)₂dppz²⁺ in 0.1 M PBS, 25mM TPrA, pH 7.5
with CT DNA and 20-mer poly dA-dT**

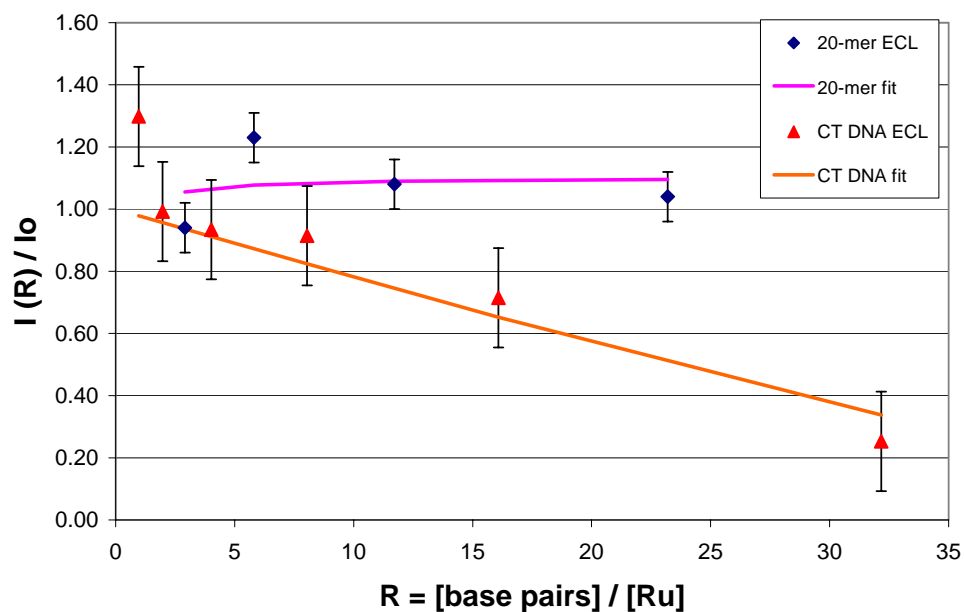


Figure 6-4. Two parameter fitting (ECL efficiency bound and free) of the ECL data with increasing base pair to Ru ratios. While the use of 20-mer improved the performance over calf thymus, neither show the light switch effect seen in PL experiments.

-
- ¹ (a) Johnson, D., LaCourse, W., *Anal. Chem.*, **1990**, 62, 589A – 597A. (b) Hughes, S., Meschi, P., Johnson, D., *Anal. Chim. Acta*, **1981**, 132, 1-10.
- ² Rubenstein, I., Bard, A., *J. Am. Chem. Soc.*, **1981**, 103, 512-516.
- ³ Garcia-Campana, A., Baeyens, G., *Chemiluminescence in Analytical Chemistry*, Marcel Dekker, New York, **2001**, p. 221.
- ⁴ Fukushima, M., Tatsumi, K., Tanaka, S., Nakamura, H., *J. Environ. Sci. Tech.*, **1998**, 32, 3948-3953.
- ⁵ (a) Carter, M., Bard, A., *Bioconj Chem*, **1990**, 2, 257-263. (b) Rodriguez, M., Bard, A., *Anal. Chem*, **1990**, 62, 2658-2662.
- ⁶ Kanoufi, F., Zu, Y., Bard, A., *J. Phys. Chem. B*, **2001**, 105, 210-216.
- ⁷ Welch, T., Corbett, A., Thorp, H., *J. Phys. Chem.*, **1995**, 99, 11757-11763.
- ⁸ Mihailovic, A., Vladescu, I., McCauley, M., Ly, E., Williams, M., Spain, E., Nunez, M., *Langmuir*, **2006**, 22, 4699-4709.

Chapter 7 SECM

As discussed in the last chapter, the effects of $\text{Ru(phen)}_2\text{dppz}^{2+}$ being intercalated into DNA do not account completely for the poor ECL efficiency demonstrated by the complex. The balance of the negative effect must lie in the deactivation of the excited state, $\text{Ru(phen)}_2\text{dppz}^{2+*}$. Intercalation alone is not the answer since the complex has enhanced emission when intercalated into DNA. However, in the ECL experiment, the pathway to the excited state goes through the oxidized Ru(III) state (Eq. 1-2 and 1-3) which is not the case in the PL experiment. The study of electron transfer up and down the helix has demonstrated that intercalated metal complexes may act as oxidizing agents of nucleotide bases (NB), so this was considered the most likely answer.¹

² The difference between the 20-mer poly dA-dT data and the calf thymus experiments also supports this because CT DNA has GC base pairs as well AT, and guanine has a much lower oxidation potential than A or T.³ This makes for a stronger driving force for the reaction:



where NB_{ox} is the oxidized nucleotide base in the helix.

Since $\text{Ru(phen)}_2\text{dppz}^{2+}$ oxidizes more positive than Ru(bpy)_3^{2+} as shown in Table 3-1 and is much less soluble in water, background processes – primarily water oxidation - precluded obtaining meaningful cyclic voltammograms as Thorp showed in ref 2 to verify this argument. To overcome this limitation, scanning electrochemical microscopy (SECM) was used to determine if adenosine/thymine were reducing $\text{Ru(phen)}_2\text{dppz}^{3+}$ back to the divalent species before the TPrA radical could generate the excited state.

Strategy

As discussed in Chapter 1, SECM may be used to probe a homogeneous following reaction of an electro-oxidized or reduced species by observing the feedback current at progressively smaller tip-substrate separations. This was the strategy to probe $\text{Ru(phen)}_2\text{dppz}^{2+}$ behavior in water – especially since tip current would not be directly observable due to the background water oxidation current overshadowing the current from the low complex concentration. It was hoped that the substrate potential could be positioned such that background processes were negligible and tip generated Ru(III) complex could be seen at the substrate by reducing it back to Ru(II) . In order to approach the substrate without adding additional chemical components to the solution, oxygen reduction at the Pt ultramicroelectrode (UME) tip (-0.2 V vs. Ag/AgCl worked best) was used. The concern was that adding an additional electroactive species might complicate measurements with DNA due to the possible interaction with the helix. Once the approach distance was determined, small steps were taken to move in as close as possible. Of note, quiet times (time when the electrodes was set to the desired potential, but no measurement was made) of six minutes or more were required to allow the background on the substrate to decay to the nA level. This minimized distortion of the negative feedback approach curve (Figure 7-1).

However, as can also be seen in Figure 7-1, some approaches fit well to theory and some did not. This was due to the inability of the Pt UME to reduce oxygen at steady state for the long periods of time required to conduct a good approach, which is usually done at $< 1\text{ }\mu\text{m/s}$. The issue of Pt stability *vis a vis* the oxygen reduction reaction (ORR) is very familiar to those who study fuel cells since the ORR is one of the half reactions in

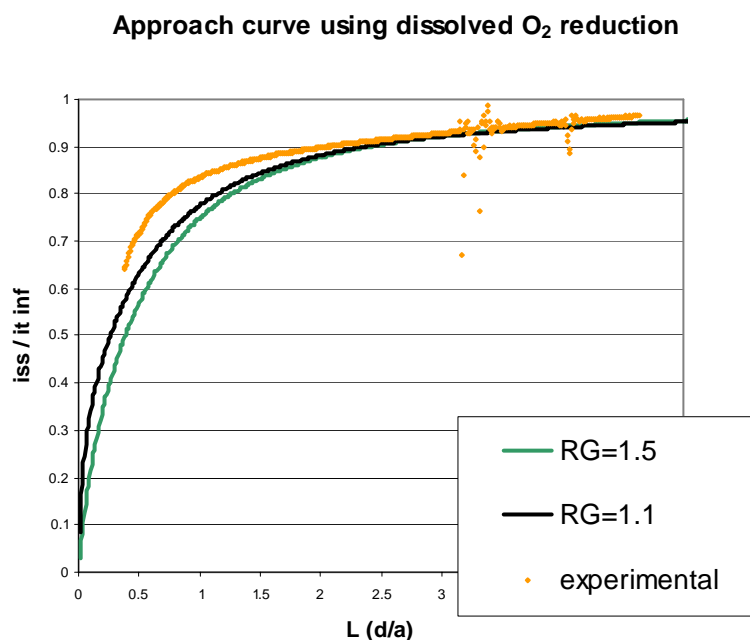


Figure 7-1. Poor (top) and good (bottom) negative feedback approach curve using dissolved oxygen reduction as the tip-generated electrode reaction. The orange traces are the steady state tip current and the other traces are various theoretical responses based on the RG of the tip.

the typical hydrogen fuel cell. Over time, even ambient amounts of CO₂ tend to poison Pt based ORR catalysts.⁴ The kinetics of this are poorly understood, and the performance of Pt is not optimum at room temperature where our SECM experiments were performed.⁵

Alternately we conducted slow controlled approaches using potentials for the complex's oxidation/reduction to conduct a positive feedback experiment until contact was made. This ensured the distance between the tip and substrate was verified without damaging the tip. Once in place, the substrate was held at a potential where the background water reduction was small, and reduction of the tip generated Ru(III) species back to Ru(II) was possible. This mode is known as tip generation, substrate collection (TGSC).

The cleanest substrate collection data in air saturated solutions came when the substrate potential was positioned at 0.35 V vs. Ag/AgCl, which showed only a 1.5 nA background current. However, it was desirable to use a potential closer to the E^0 of Ru(phen)₂dppz³⁺ reduction to ensure no other redox reactions might be taking place and contributing to the current. Degassing the solution with Ar was required to allow using a substrate potential of 1.0 V and still be able to obtain a reasonably low background. This was because greatly reducing the oxygen content precluded the background formation of PtO which begins in earnest generally around 0.8 V vs. Ag/AgCl. Generally, the collection efficiency of the substrate in a TGSC experiment with intervening reaction was in excess of 90%,⁶ at L values < 2. Thus the substrate current should accurately reflect the current of the redox active species made at the tip, even though background processes (like water oxidation – significant at the E^0 of the complex) at the tip preclude detecting this current directly.

Normalization of the Current

As mentioned in Chapter 1, standard SECM analysis requires knowledge of the tip current for normalization of the data. However, the solubility of the complex was not sufficiently large in water to allow its current to be seen above the water oxidation, so that value must be calculated. To do so, the steady state current at a UME disk is given by⁷:

$$I_{ss} = 4nFDCa \quad \text{Eq. 7-2}$$

where n is the number of electrons in the electrochemical step, F is Faraday's constant, D is the diffusion coefficient, C is the concentration in mol/cm³, and a is the tip radius in cm. Since a scan rate study in water was not possible due to the poor solubility of the complex, the diffusion coefficient was only measured in acetonitrile (Chapter 3). However, using the Einstein-Stokes equation, an aqueous diffusion coefficient may be estimated. That equation says:

$$D = kT/6\pi\eta_0R \quad \text{Eq. 7-3}$$

where k is the Boltzman constant, T the temperature, η_0 the viscosity and R the gas constant.

Taking a ratio of the diffusion coefficient of the complex in water to that in acetonitrile (MeCN), all the constants reduce to unity and the equation becomes:

$$D_{H_2O} = D_{MeCN} (\eta_{MeCN} / \eta_{H_2O}) \quad \text{Eq. 7-4}$$

D_{MeCN} was determined experimentally in Chapter 3, and the two viscosities are available from the CRC Handbook so D_{H_2O} is 3.5×10^{-6} cm²/s. Therefore, with the electrode used, the tip current of Ru(phen)₂dppz²⁺ expected at a large distance from the substrate in this experiment should be 0.385 nA for the free complex.

Free Complex Results

The TGSC experiment shown in Figure 7-2 showed the $E_{1/2}$ to be 1.23 V vs. Ag/AgCl in the buffered solution; this was a bit of data unattainable via the various other methods employed and was about 100 mV negative of the value in acetonitrile. Of note, the magnitude of the anodic background current varied with the substrate potential and tip separation as seen in Figure 7-2. The more positive the substrate potential, the larger the background Pt oxidation current became. However, if multiple sweeps were conducted, while the magnitude of the collected $\text{Ru(phen)}_2\text{dppz}^{3+}$ current was consistent, the background would fall to acceptable values indicating the potential step ($t^{1/2}$ decay) nature of the substrate response caused by dissolved oxygen. Additionally, the approach of the tip would block the diffusion of oxygen to the substrate thus diminishing the anodic substrate response.

Current vs. distance data showed significant, negative deviation from the case of no following reaction in both air saturated and degassed experiments (Figure 7-3). The plot shows the substrate current as a function of distance from the substrate. Note each axis was normalized as discussed in Chapter 1, i.e. the current to the tip current at large separation and the distance to the tip radius. Overlaid on this data was the established curve for tip current in a positive feedback with no following reaction experiment for comparison. The poor collection efficiency inside $L = 2$ indicated that the Ru(III) species was undergoing a reaction prior to reaching the substrate even in the absence of DNA.

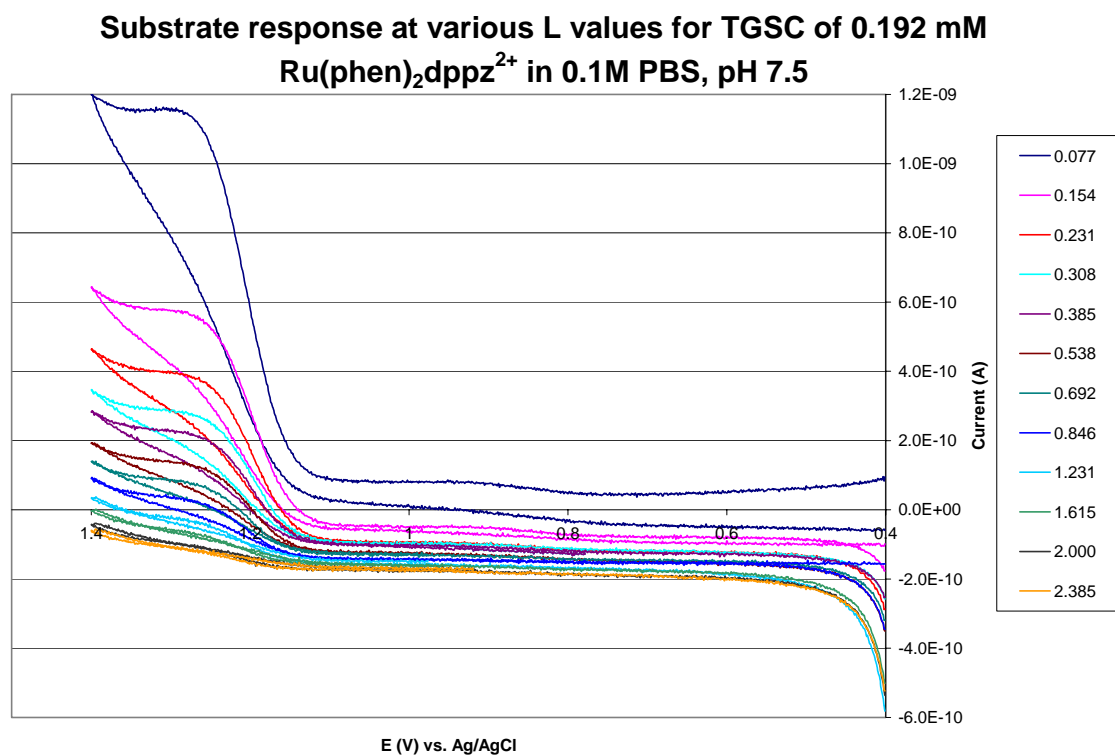


Figure 7-2. Uncorrected Pt substrate current at various L values for the 26 μm Pt tip. Conditions were air saturated, those indicated, and the substrate held at 0.35 V. Note the displacement of the baseline based on distance and the tailing off cathodic background current at the beginning of the sweep. Sweeps shown are the third of three consecutive and represent the reproducible data.

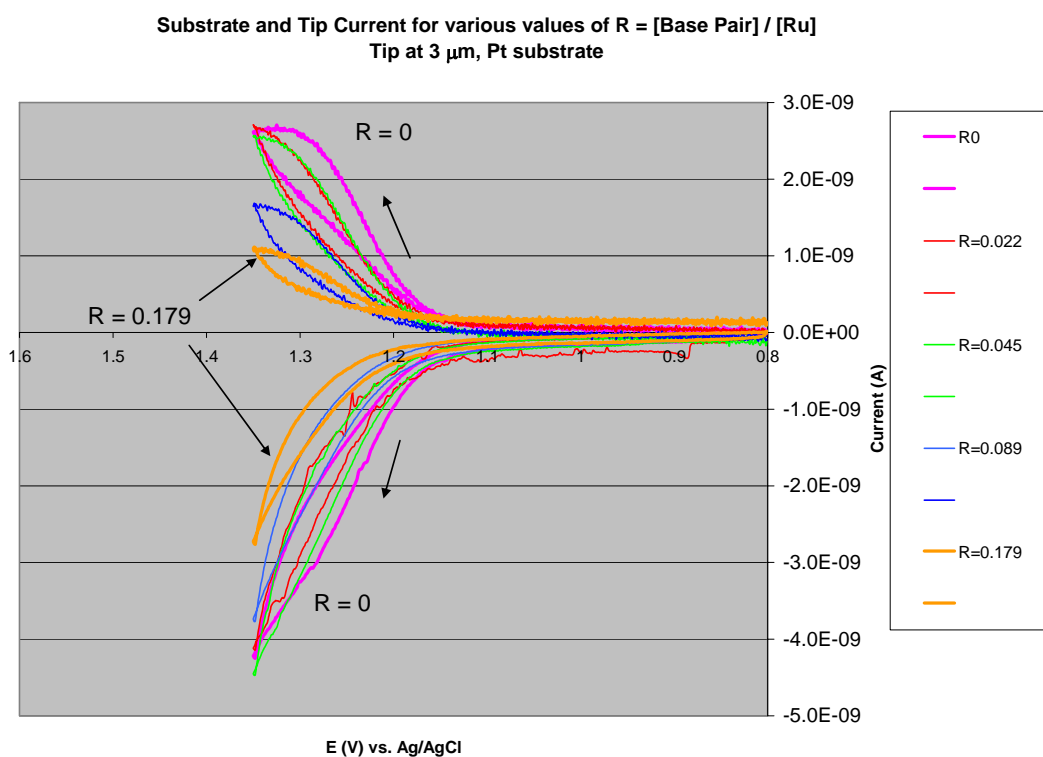
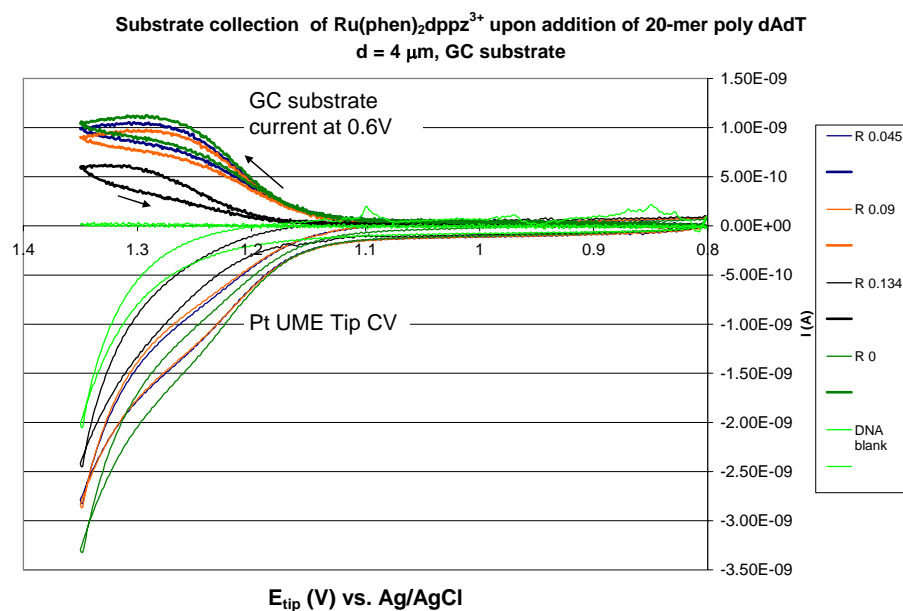


Figure 7-3. $0.115 \text{ mM } \text{Ru}(\text{phen})_2\text{dppz}^{3+/2+}$ tip and substrate behaviour at a $26 \mu\text{m}$ diameter Pt UME tip above 1 cm glassy carbon (top) and 1 mm Pt disk (bottom) substrates. The tip was brought to the distance indicated and additions of 20-mer dAdT were made resulting in the R values indicated. Background oxidative current was subtracted.

Since the results in degassed solution were very close to those obtained in air saturated solution, the reaction was either with water or the Ru(III) was patently unstable. However, the electrochemistry shown in Chapter 1 in a different, airless solvent ruled out the latter. Thus, a redox reaction with water or a water oxidation product must be taking place.

The case for a direct reaction with water by oxidized ruthenium complexes has some precedent. Most of those studied are oxo-bridged ruthenium dimers,^{8,9} but some homonuclear cases have been reported.^{10,11} The homonuclear Ru complexes cited are oxidized by Ce(IV) instead of at an electrode, so data from an electrochemical scheme was scarce. In all cases there was an open site at the Ru center that allowed for multiple electron transfers. This is important since the oxidation of water is a four electron process,



Thus, when the Ru(III) version of the complex was produced, either a bridged species formed or one of the ligand sites was modified. Evidence for either scheme was not available in the current data. Whatever the event occurring, a following reaction was evident, and one possibility for this was a catalytic reaction where Ru(II) would be regenerated. This is explored further in the next chapter.

Addition of DNA

Subsequently, small volumes of 20-mer poly dA-dT were added to the SECM cell with Ru(phen)₂dppz²⁺ already present, and any effects on the substrate current were observed. The wait time was 10 minutes after all additions to allow the polynucleotide time to diffuse into the gap and the complex to intercalate. In multiple experiments, at both Pt and GC substrates, the

addition of the 20-mer caused significant loss of collected Ru(III). As Figure 7-3 and 7-4 show, even at small R values, the amount of Ru(III) surviving diffusion down to the substrate was significantly lowered by the presence of nucleotides.

While there was a small amount of dilution upon addition of the 20-mer aliquots, the volumes amounted to only 6% over the initial range of R values studied. Since the current is directly proportional to the concentration (Eq. 7-1), that would result in a reduction in current of the same magnitude. The same can be said for the diffusion coefficient. The 20-mer dA-dT had a diffusion coefficient about 60% less than the complex, but at the maximum R value shown, only about 10-15% of the complex was intercalated and therefore exhibited this diffusion coefficient. The rest was free complex. Therefore, the overall current should show very little impact due to intercalated complex if that were the only issue at work. However, the reduction in current is 60% indicating another unidentified process is taking place.

Given the difficulty in making light measurements with DNA, it was considered that the electrode surface was being fouled by organic oxidation products. Noting the tip current in Figure 7-4 was decreasing in concert with the substrate response; this could be an alternate explanation. Additional experiments up to saturating amounts of 20-mer ($R = 10.1$) were attempted to observe the feedback response with the entire amount of complex intercalated. In these experiments, an electrode cleaning step was added similar to the PAD profile of Chapter 6. A step to -1.3 V vs. Ag/AgCl was done for 20 seconds just prior to performing the cyclic voltammetry. The results were the same. The collection efficiency became negligible at R values > 3 .

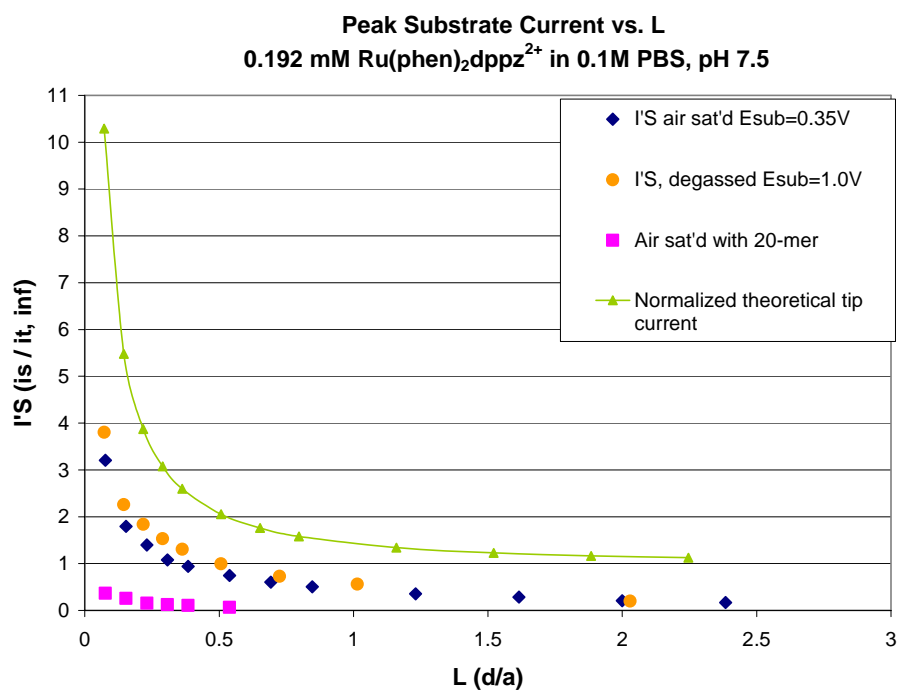


Figure 7-4. Substrate current response of a tip-generation, substrate collection (TGSC) experiment in both air saturated and degassed solutions. The current is normalized to the calculated tip current at far distances e.g. $i_{t, \infty}$ and denoted $I'S$. Both are similar results although the background current is less in the degassed experiment allowing positioning of the substrate potential closer to the E^o to confirm the substrate is collecting the species of interest.

Kinetic Estimates

Using the method for estimating the kinetics of an intervening process in an SECM experiment as outlined in the introduction, the rate constant of the following reaction may be determined by realizing that the time to diffuse across the gap between the tip and substrate (t_{diff}) is given by¹²

$$t_{\text{diff}} \sim d^2 / 2D \quad \text{Eq. 7-6}$$

A pseudo first order rate law assuming water is the catalyst and thus present in great excess would be

$$\text{rate} = k_{\text{fol}} [\text{Ru(III)}] \quad \text{Eq. 7-7}$$

Since the following reaction is in competition with the substrate for Ru(III), the rate constant in Eq. 1-7 may be estimated by

$$k_{\text{fol}} = 1 / t_{\text{diff}} \quad \text{Eq. 7-8}$$

and the time for Ru(III) to diffuse across the gap represents a time faster than that required to take part in the reaction. So, to enter Eq. 7-6, we look for a distance where the substrate starts to significantly collect Ru(III). Inspection of Figure 7-3 shows that this occurred for the results without added 20-mer poly dA-dT beginning at $L = 0.4$. Since this experiment used a $13.8 \mu\text{m}$ radius tip, that L value corresponds to a tip/substrate separation of $5.5 \mu\text{m}$ and, via Eq's 7-7 and 7-8, k_{fol} may be estimated as 24 s^{-1} . The process with DNA is more complicated, since the substrate response represents current from both intercalated and free complex and less than saturating amounts of 20-mer were added. However, an estimate of the total effect may be done in the same manner. Given that less than significant collection was occurring even at $L = 0.1$, a

lower estimate of that process was 360 s^{-1} . Further, if the pseudo first order process is converted to a second order rate equation (since the 20-mer is not present in great excess), then:

$$k_{\text{fol}} = k'_{\text{fol}} [\text{dA-dT}] \quad \text{Eq. 7-9}$$

and k'_{fol} is estimated at $\sim 10^6 \text{ M}^{-1}\text{s}^{-1}$. This may seem large compared to Thorp's value for $\text{Ru}(\text{bpy})_3^{2+}$ with the guanine present in calf thymus DNA of $7 \times 10^5 \text{ M}^{-1}\text{s}^{-1}$.¹³ However, there is a distinct difference in that study compared to the current study with $\text{Ru}(\text{phen})_2\text{dppz}^{2+}$. $\text{Ru}(\text{bpy})_3^{2+}$ is not an intercalator but rather electrostatically binds to the phosphate backbone. This requires the electron transfer between the base and the complex to occur at greater distances and therefore a slower rate. Since $\text{Ru}(\text{phen})_2\text{dppz}^{2+}$ literally inserts the dppz ligand in between base pairs, the proximity of reactants should translate into a larger rate constant for the electron transfer.

The significant drop in both tip and substrate current was reasonably due to additional scavenging of the Ru^{3+} by the 20-mer. The aqueous redox potentials of adenine and thymine have been interpolated as 1.28 V and 1.26 V vs. NHE at pH 7.5 based on a table published by Faraggi et al.¹⁴ Converting these to potentials vs. Ag/AgCl, values for both bases were around 1 V, well negative of the 1.24 V for $\text{Ru}(\text{phen})_2\text{dppz}^{3+}$ reported earlier in the chapter. Thus, the bases were at least thermodynamically amenable to oxidation by the complex.

The additional reduction in collected current could occur due to additional binding of the complex. Electrostatic interactions at low R values have also been reported by Hiort et al.¹⁵ Any amount of additional complex binding would subsequently result in slower diffusion and therefore show reduced collected current due to less tip current. The magnitude of this was, however, not defined. In the end, it was not possible to separate these two potential effects that account for the significantly reduced substrate collection current in this experiment.

Ru(III) and Ru(II) Binding Differences

Also noted in Figure 7-4, was that the half wave potential was shifted more positive as DNA was added. A blank trial with DNA but no complex was run in both experiments to ensure no electrochemistry of the 20-mer poly dA-dT was occurring and is shown in the glassy carbon experiment in Figure 7-4. Since these blanks confirm no adenosine or thymine electrochemical oxidation, the shift in half-wave potential was due to intercalation of the complex. Bard and Carter have used this information to estimate of the ratio of binding constants for the Ru(II) and Ru(III) species.¹⁶ While the complete extent of binding difference was unknown due to no collection seen at saturation levels of the 20-mer, a positive trend in the half wave potential was obvious. A minimum figure was available based on the data taken and the following:

$$E_b^{\circ} - E_f^{\circ} = 0.059 \log (K_{\text{Ru(II)}} / K_{\text{Ru(III)}}) \quad \text{Eq. 7-10}$$

which is simply an application of the Nernst equation. Using information from Figure 7-4, where the average $\Delta E_{1/2}$ is +30 mV from the free complex to the bound complex, the Ru(II) was bound 3x more strongly than Ru(III) at a minimum. These results were not surprising given the similar conclusions of previously studied, analogous complexes. Bard and then Thorp interpreted the results as indicative of a strong interaction between the complex and the hydrophobic core of the DNA helix. The inference was that increasing the charge state of the complex decreases the binding in cases where the complex binds primarily via hydrophobic interactions.

-
- ¹ Yoo, J., Delaney, E., Stemp, D., Barton, J., *J. Am. Chem. Soc.*, **2003**, *125*, 6640-6641
- ² Sistare, M., Holmberg, R., Thorp, H., *J. Phys. Chem. B*, **1999**, *103*, 10718-10728
- ³ Faraggi, M., Broitman, F., Trent, J., Klapper, M., *J. Phys. Chem.*, **1996**, *100*, 14751-14761.
- ⁴ Kinoshita, K., *Electrochemical Oxygen Technology*, John Wiley & Sons, New York, 1992, p. 186.
- ⁵ Ibid, p. 33.
- ⁶ Bard, A., Mirkin, M., *Scanning Electrochemical Microscopy*, Marcel Dekker, New York, **2001**, p. 6.
- ⁷ Bard & Faulkner, pg. 174.
- ⁸ Okamoto, K., Miyawaki, J., Nagai, K., Matsumura, D., Nojima, A., Yokoyama, T., Kondoh, H., Ohta, T., *Inorg. Chem.*, **2003**, *42*, 8682-8689.
- ⁹ Yamada, H., Koike, T., Hurst, J., *J. Am. Chem. Soc.* **2001**, *123*, 12775-12780
- ¹⁰ Yagi, M., Sukegawa, N., Kaneko, M., *J. Phys. Chem. B.*, **2000**, *104*, 4111-4114
- ¹¹ Zong, R., Thummel, R., *J. Am. Chem. Soc.* **2005**, *127*, 12802-12803
- ¹² Bard and Mirkin, p. 10.
- ¹³ Johnston, D., Thorp, H., *J. Phys. Chem.*, **1996**, *100*, 13837-13843.
- ¹⁴ Faraggi, M., Broitman, F., Trent, J., Klapper, M., *J. Phys. Chem.* **1996**, *100*, 14751-14761.
- ¹⁵ Hiort, C., Lincoln, P., Norden, B., *J. Am. Chem. Soc.*, **1993**, *115*, 3448-3454
- ¹⁶ (a) Carter, M., Bard, A., *J. Am. Chem. Soc.*, **1987**, *109*, 7528-7530. (b) Carter, M., Rodriguez, M., Bard, A., *J. Am. Chem. Soc.* **1989**, *111*, 8901-8911.

Chapter 8 Digital Simulation

The SECM literature is replete with examples of validation of the theoretical model using digital simulation. If the simulation agrees well with actual experimental data, the model and simulation are thought to be accurate representations of the experiment, and therefore useful in modeling future systems. The listed references cover several different examples. To use the notation for coupled reactions introduced in Chapter 1, the ECE, and DISP1 reactions are treated in this manner¹ as are the EC_i and EC_{2i} pathways.² The efforts toward elucidating the behavior of $Ru(phen)_2dppz^{3+/2+}$ in water done in Chapter 7 would suggest it follows the EC' or catalytic pathway which has not been reported previously in an SECM environment, though theoretical EC' work for a UME tip has been done.³ In an effort to better understand the complex's behavior, digital simulation of the EC' mechanism was attempted.

Multiphysics

Since the last paper of this type was completed, a powerful, multi-faceted software package, COMSOL Multiphysics, has been authored.⁴ It couples a number mathematical algorithms for solving differential equations with a multidimensional, user defined, graphical representation of the experimental arrangement. The symmetry of the SECM experiment lends itself well to a two dimensional rendering, which keeps the computational requirements reasonable. This also keeps the rendering recognizable as the environment of the electrodes in question. Figure 8-1 shows a simulated 25 micron diameter tip with an RG of 2 (conical region lower left), separated from the substrate (top boundary) by 100 microns.

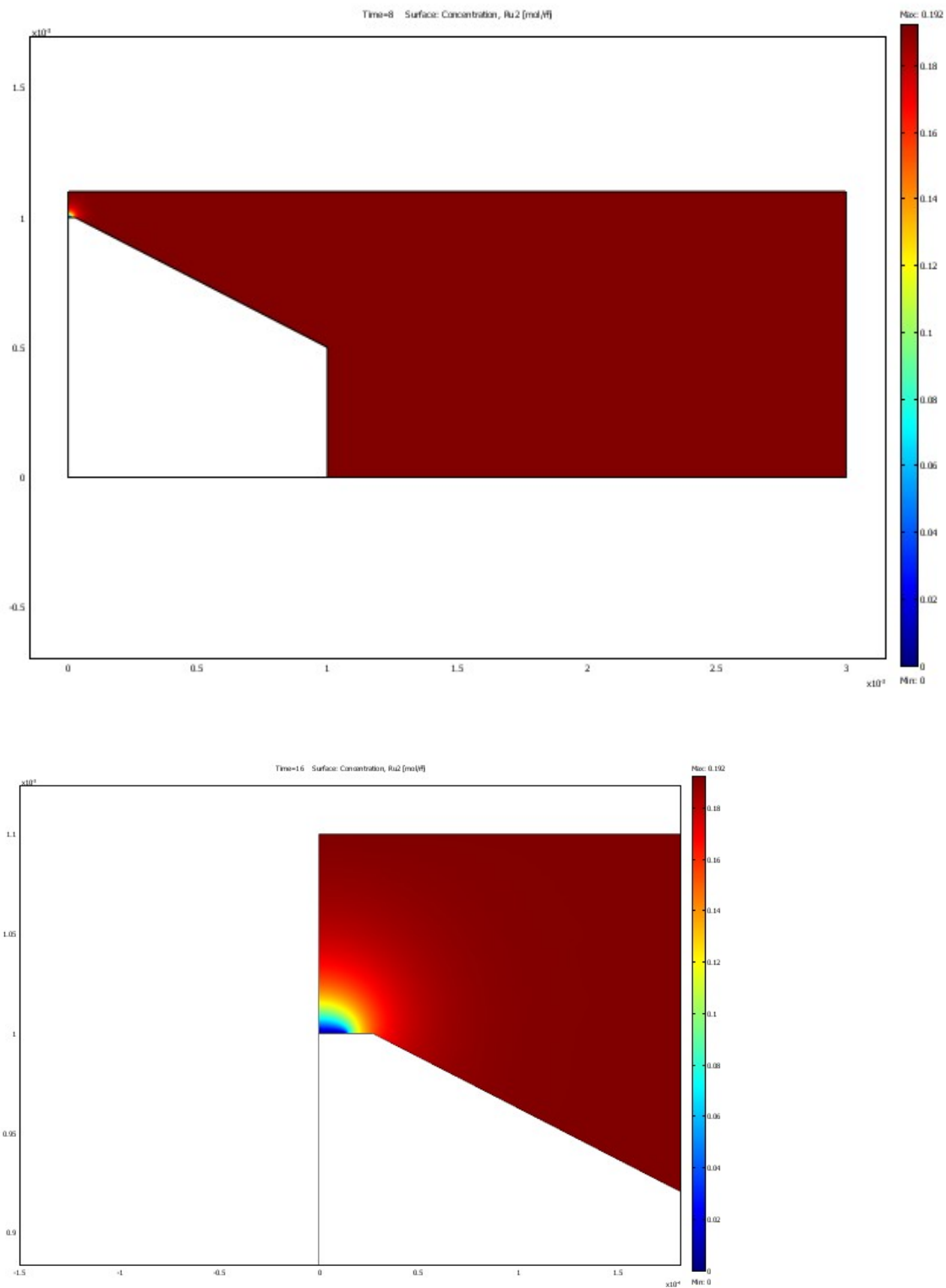


Figure 8-1. Graphical display of the concentration profile of Ru^{2+} during an SECM experiment. The legend at right connects color to concentration value.

The top boundary may be made insulating or electroactive to simulate either substrate situation in the SECM experiment. The separation may also be easily changed with sub-micron resolution if desired. The program parameters used are included in Appendix B.

Boundary Conditions

The proposed pathway for the Ru(II) complex's reaction with water would be:



where X is present in large concentration leading to a pseudo first order kinetic treatment.⁵

Defining the relevant flux equations at the appropriate boundary simulates a diffusion controlled electrode process, and the program then applies a differential equation solver to obtain for the concentration profile. For Eq. 8-1, the electrode oxidation reaction, the inward flux of Ru^{2+} to the tip is defined as:

$$(k_{\text{ft}} * [\text{Ru}^{2+}]) - (k_{\text{bt}} * [\text{Ru}^{3+}]) \quad \text{Eq. 8-4}$$

where k_{ft} is the rate constant for the forward reaction at the tip. The flux of Ru^{3+} away from the tip is simply the negative of the above expression. The rate constant is further defined as:

$$k_{\text{ft}} = k^0 * \exp(-\alpha f \eta) \quad \text{Eq. 8-5}$$

where k^0 is the heterogeneous electron transfer rate constant, α as the 'transfer coefficient' that arises in the Butler-Volmer treatment of electrode kinetics,⁶ f is the inverse of RT/F which is 38.92 V^{-1} at room temperature, and $\eta = E - E^0$ for the electrode process in question. Similarly, k_{bt} is the rate constant for the back reaction and is:

$$k_{\text{bt}} = k^0 * \exp[(1-\alpha)f\eta] \quad \text{Eq. 8-6}$$

Current is derived by integrating the solution to the temporal and two dimensional spatial concentration profiles for the species of interest at the appropriate boundary (either the tip or substrate), i.e.:

$$i = nFA \int [Ru^{2+/3+}](x,t) \quad \text{Eq. 8-7}$$

The flux and current at the substrate use the same equation. A voltammogram is generated by using a time dependent solver and making the tip potential a function of time:

$$E_t(t) = E_i + vt \quad \text{Eq. 8-8}$$

where E_i is the initial potential, v the scan rate in V/s, and t the elapsed time of the sweep.

Voltammetric Results

Since the program had significant difficulties in smoothly solving the temporal concentration profiles when making the sweep reverse as in actual cyclic voltammograms, only the sweep out was simulated. Further, as seen in Figure 8-2, there are still problems with slight discontinuities, and efforts to fix this with finer mesh values only ran into computer memory limitations. So, a simple chronoamperometric response was obtained by simulating a step to 1.4 V and taking the steady state current after 8 s. The agreement between the two treatments was within 10 picoamps.

To better evaluate the basic simulation of an experiment with an ultramicroelectrode acting as an SECM tip, the simulation was run with actual experimentally derived and controlled parameters, i.e. the concentration and diffusion coefficient of $Ru(phen)_2dppz^{2+}$ and the calibrated electrode dimensions used in Chapter 7. The comparison at large substrate separation (100

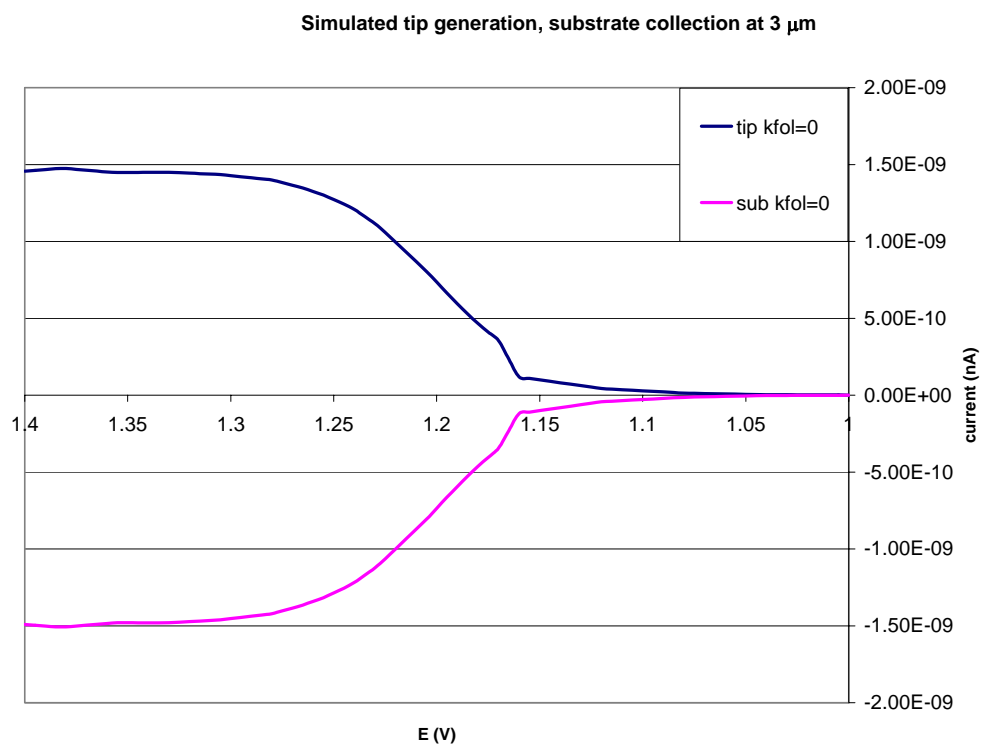


Figure 8-2. A COMSOL Multiphysics® generated SECM cyclic voltammetry TGSC experiment. The blue trace is the tip CV for an electroactive species whose $E^{\circ'}$ is 1.2 V and the magenta trace is the substrate response while poised at 1V. While the steady state current values generated agree well with previously established theory and practice, the ability to produce a smooth voltammogram varied with substrate-tip separation.

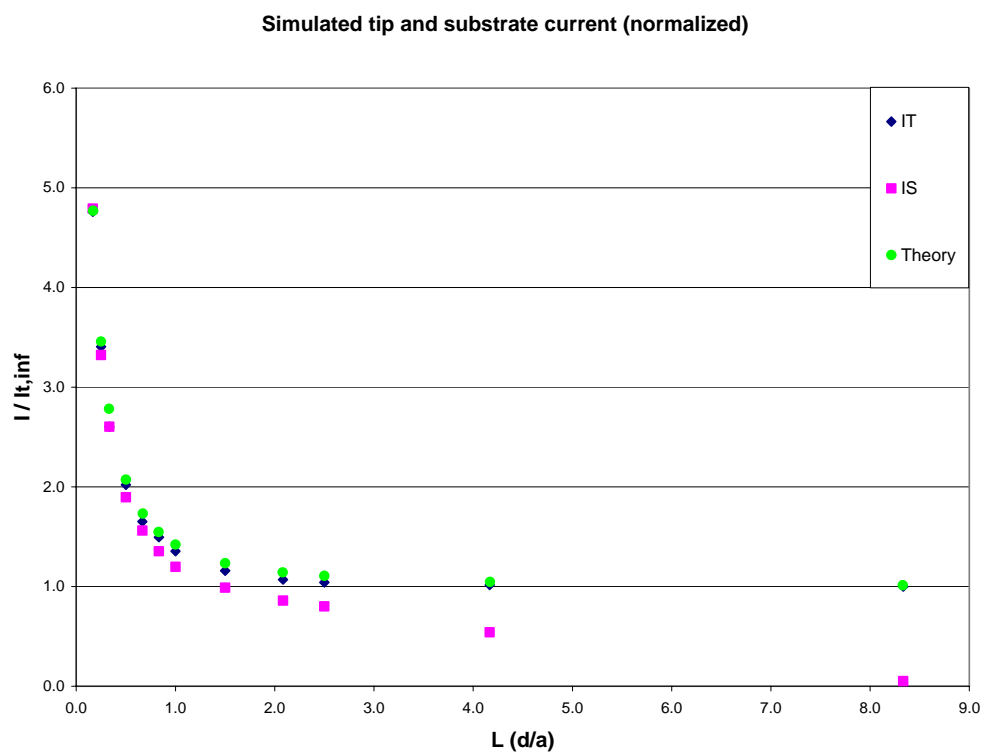


Figure 8-3. Simulated steady state tip and substrate current normalized to the tip current at far distance from the substrate ($i_{t,\infty}$). The points labeled ‘Theory’ come from Eq. 8-9.

microns) was favorable with the simulation generating 0.382 nA vs. the calculated value of 0.356 nA using Eq. 7-1; a disagreement of only 6.4%.

Approach Curves

Next, an approach curve was generated by obtaining the simulated tip current at various L values and compared with the well-established theory found in Bard and Mirkin (Figure 8-3). For an RG of 2, the points are generated via:

$$A + B/L + C \exp(D/L) \quad \text{Eq. 8-9}$$

where A = 0.6687, B = 0.6974, C = 0.3218, and D = -1.745. The tip values are quite close, and the substrate values approach 100% collection efficiency as L drops below 2 as expected.⁷

EC' Modeling

With confidence the simulation could reproduce the familiar behavior of an SECM experiment in the positive feedback or TGSC mode, results were obtained by adding a following, pseudo first order, catalytic reaction given by equation 8-2, generating working curves for various rate constants of that reaction. The rate equations in solution are given by:

$$\partial[\text{Ru}^{3+}]/dt = -k_{\text{fol}} [\text{Ru}^{3+}] \quad \text{Eq. 8-10}$$

and since it is catalytic,

$$\partial[\text{Ru}^{2+}]/dt = k_{\text{fol}} [\text{Ru}^{2+}] \quad \text{Eq. 8-11}$$

The initial results, using the CV model, are shown in Figure 8-4 as plots of tip and substrate current vs. the tip potential with the substrate potential at 1.0 V. However, there was significant perturbation of the substrate response at this potential. Note there was an initial anodic current that decayed and was subsequently overlaid by the cathodic current.

This can only be construed as oxidation of Ru(II) at the substrate as well as the tip. While surprising to see initially, recall the model uses well established equilibrium kinetics as described above – i.e. a forward and back heterogeneous electron transfer reaction at the electrode surface. Even though 1 V is 200 mV negative of the E° designed for the simulation and results in reduction of Ru(III) produced at the tip, once Ru(III) diffuses the distance from tip to substrate, the back, oxidation reaction of Ru(II) was a small but finite quantity. It would be the only response seen until Ru(III) arrives from the tip. Large perturbations were seen at large k_{fol} since most Ru(III) produced at the tip was quickly reverted back to Ru(II), so the same catalytic response seen at the tip also occurred at the substrate - only more pronounced since the substrate was a much larger electrode surface.

To verify the initial anodic response was due to the substrate potential, a series of substrate currents were recorded at varying substrate potentials as shown in Figure 8-5. Note the anodic pulse disappeared by 0.6 V, emphasizing the exponential behavior seen in Eqs. 8-5 and 8-6. To alleviate this, the responses were re-recorded and switched to chronoamperometric simulations from CV at the lower substrate potential. The result was no anodic pulse and the expected trend. These are shown in Figure 8-6.

Additionally, since the tip and substrate potentials were moved so far from the E° , very fast heterogeneous electrode kinetics resulted, and the simulation was simplified even further. In the limiting, very fast electrode kinetics case, past simulation has merely set the boundary condition of the electrode surfaces such that no starting material exists there. For example, since Ru(II) is being converted to Ru(III) at the tip, the boundary condition there may be set as:

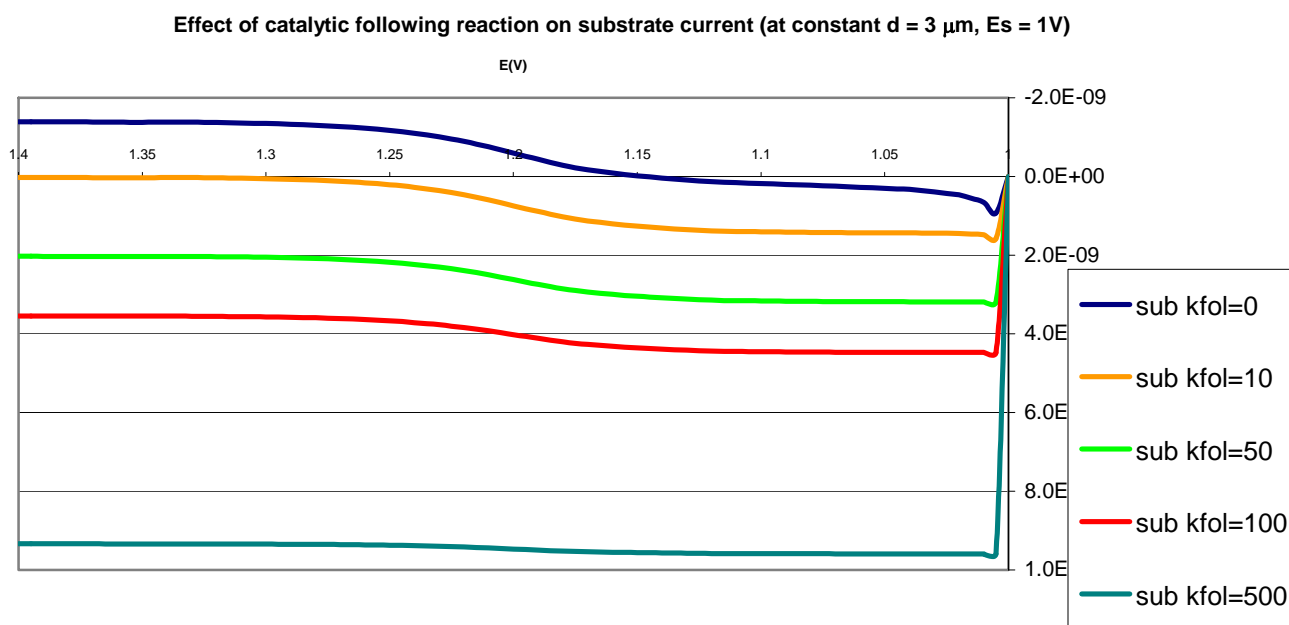
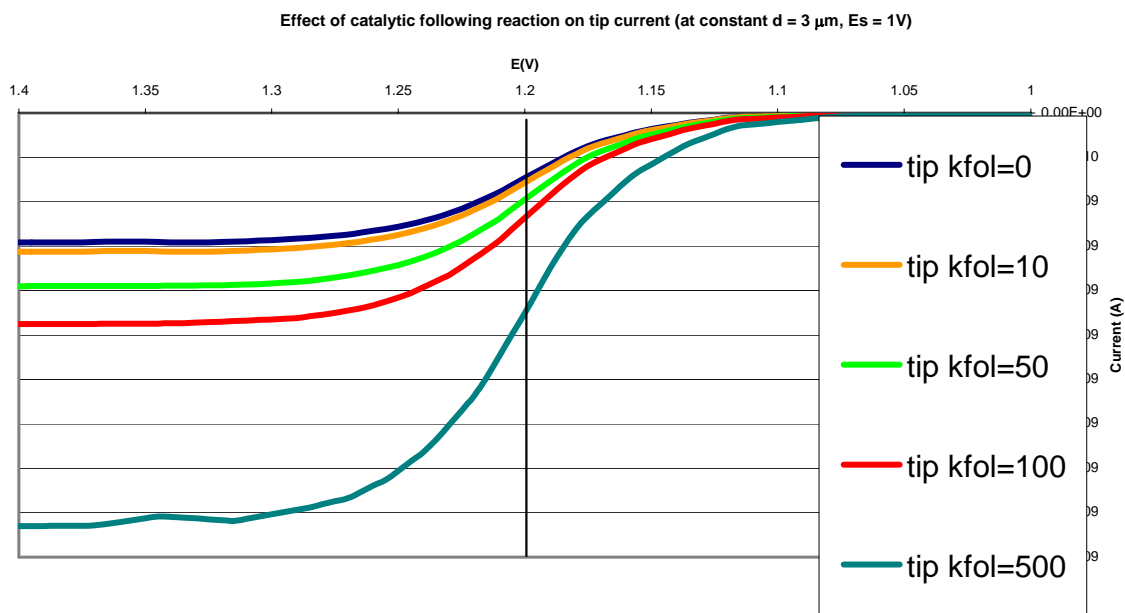


Figure 8-4. Simulated tip and substrate current at $3 \mu\text{m}$ separation with the substrate potential set at 1.0 V . The tip current is catalytically enhanced at faster following reaction rate constants. Note the anodic current at the substrate due to the significant back reaction rate at the given potential (Eq. 8-6). At fast, following reaction rate constants (k_{fol}), this current is also catalyzed and becomes the significant contributor to substrate response. Scan rate is 50 mV/s .

$$\text{For } z_t = 0, \text{ and } 0 \leq r_t \leq a, [\text{Ru(II)}] = 0 \quad \text{Eq. 8-12}$$

where z_t is the distance perpendicular to the tip electrode surface, r_t is any point on the tip electrode extending radially from the center towards its edge, and a is the radius. Similarly for the substrate:

$$\text{For } z_s = 0, \text{ and } 0 \leq r_s \leq a, [\text{Ru(III)}] = 0 \quad \text{Eq. 8-13}$$

The difference in current produced by this approach and that using electrode kinetics was negligible.

Next, with the small aberrations worked out, the catalytic following reaction was inserted into the simulation and sample currents are shown in Figure 8-7. The results were quite interesting. As the following reaction rate constant increased, the amount of Ru(II) regenerated increased and therefore drove the current up. This effect is termed catalytic to distinguish it from the term feedback which is used when the returning Ru(II) is generated by the substrate i.e. a homogenous process vs. a heterogeneous process. Figure 8-8 shows the collection efficiency with increasing k_{fol} . Note how repeatedly smaller amounts of Ru(III) diffused across the gap and this resulted in smaller substrate currents. Alternately, the distance for the substrate feedback to overcome the following reaction interception of Ru(III) was closer and closer as k_{fol} increased. This was the expected effect before the simulations were run. It was less clear how the response would compare to the unperturbed situation once inside this close distance. Figure 8-9 answers that question, showing that any following reaction decreased the feedback at all distances. This, of course ignores tunneling between the electrodes. While this might seem reasonable upon

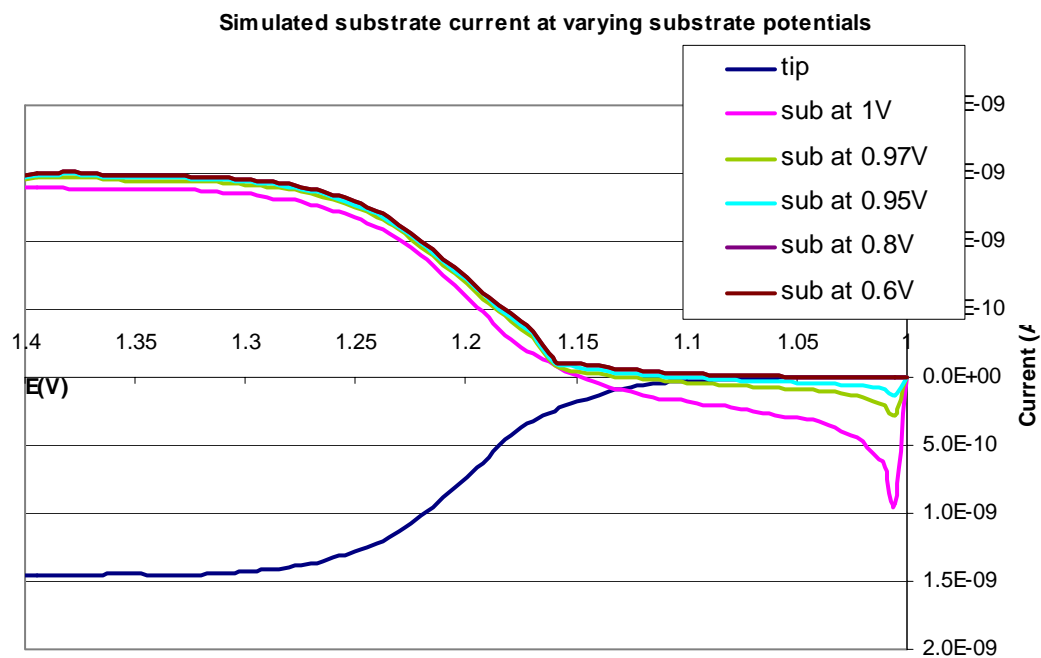


Figure 8-5. Simulated substrate responses at progressively smaller substrate potentials. Note the diminishing anodic pulse at early times. The tip current is shown for reference and shows the near unity collection efficiency at the 3 μm distance. Scan rate is 50 mV/s.

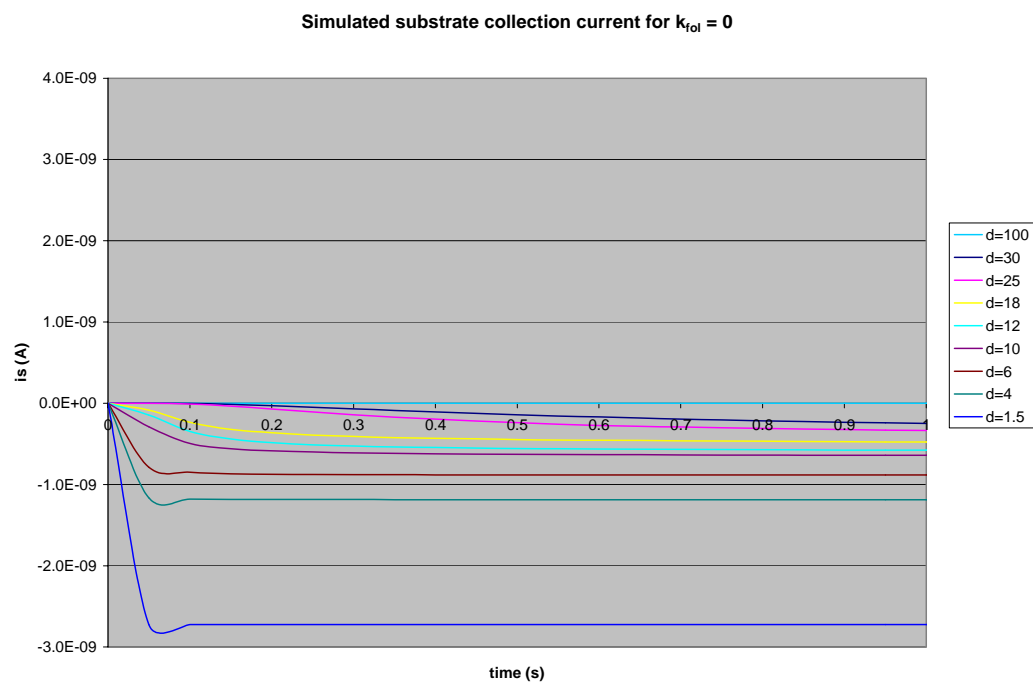
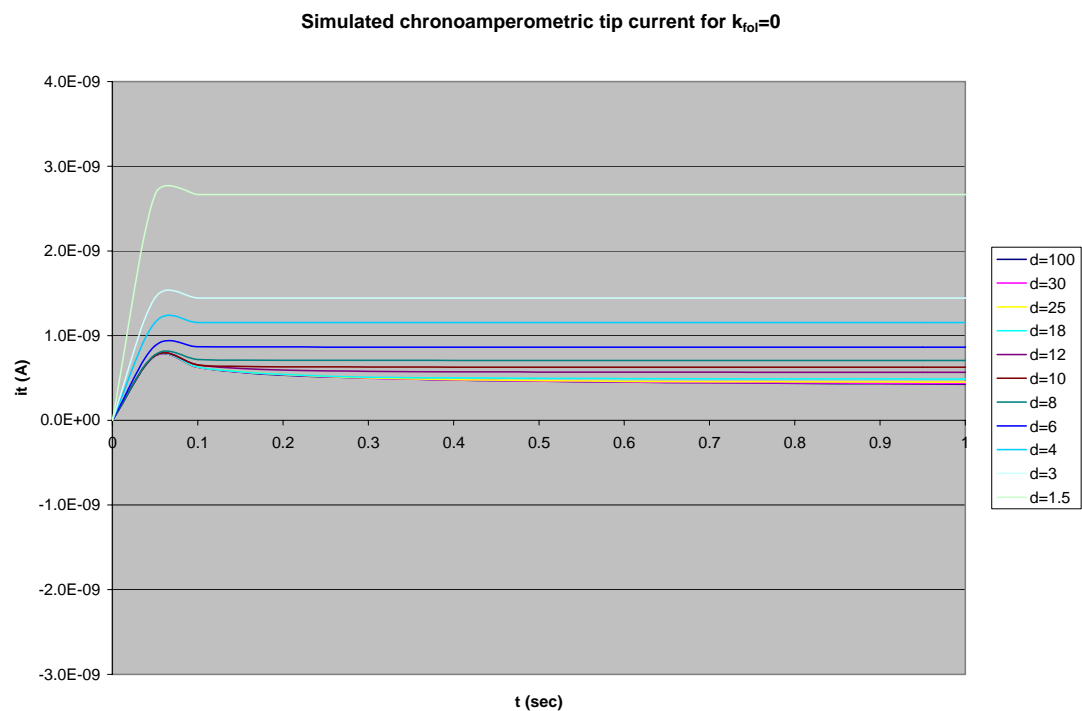


Figure 8-6. Simulated substrate and tip currents with the substrate potential moved negative to 0.6 V. While the steady state tip current magnitudes are unchanged from Figure 8-4, note the anodic pulse is absent.

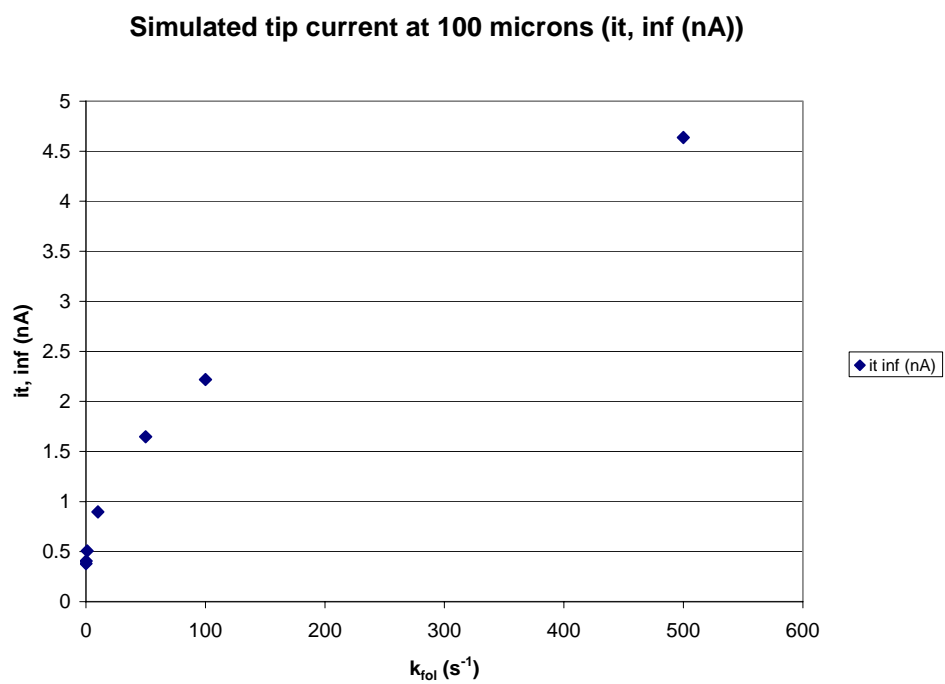


Figure 8-7. Simulated tip current at large tip-substrate separation ($i_{t,\infty}$) showing the catalytic effect of the following reaction.

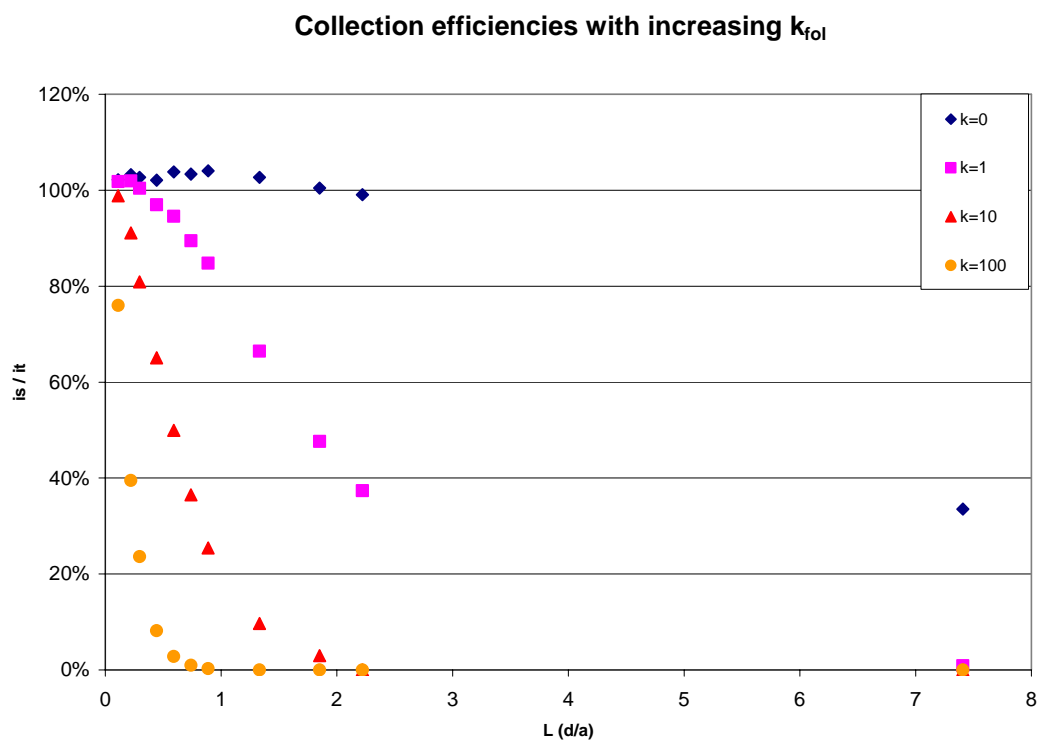


Figure 8-8. The effect of the following reaction on collection efficiency at the substrate. As the reaction proceeds at faster rates, less Ru^{3+} survives the trip to the substrate for conversion back to Ru^{2+} for a given distance. For each k_{fol} , there is a distance at which this is overcome, but it is closer as the rate increases.

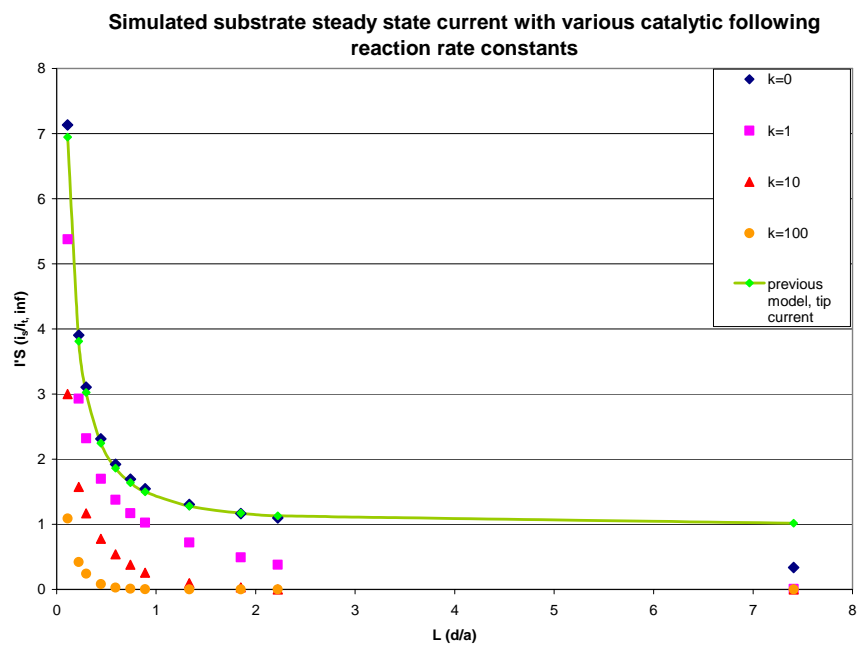
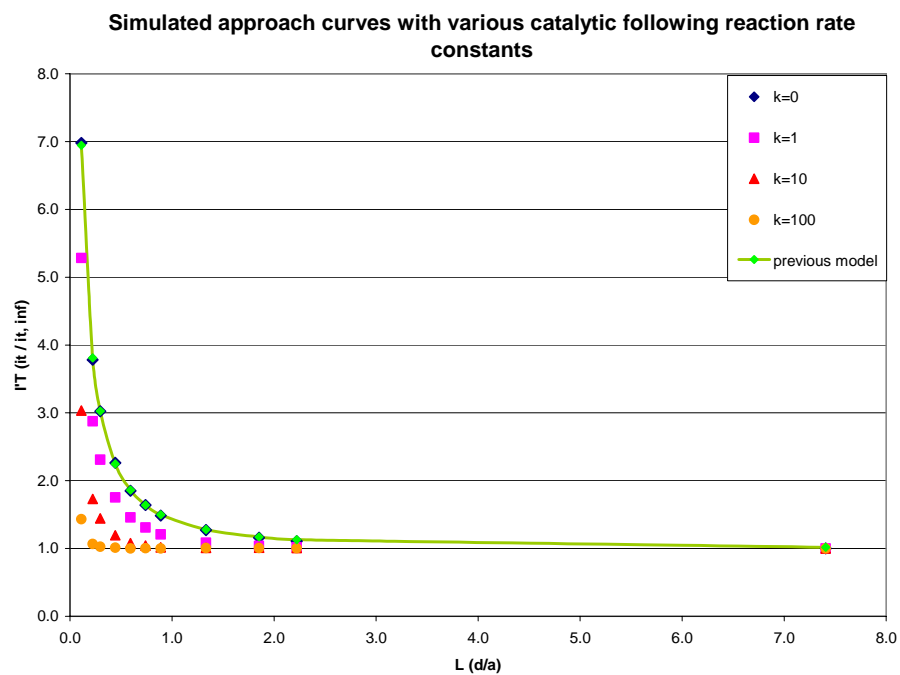


Figure 8-9. Simulated normalized current vs. distance data for the tip (top) and substrate for various k_{fol} . For comparison, the unperturbed, normalized tip current curve from the previous model is shown.

introspection for the substrate, it was surprising for the tip which would be receiving Ru(III) from two sources.

Evaluating Multiphysics Using Known EC_i Data

To make a quick inspection of Multiphysics' behavior, a non-catalytic (EC_i), pseudo first order following reaction was used, and the response compared to results already published for this situation.⁸ The results are shown in Figure 8-10. The plot shows normalized tip current vs. L compared to the previously derived tip current with no following reaction. As was shown before, a negative perturbation was realized as the tip approached the substrate, but the species in the feedback loop was whisked away by the following reaction. Eventually, the tip got close enough to the substrate, and positive feedback through diffusion occurred faster than the following reaction, but the magnitude was less than the unperturbed situation. Also included is a plot using Mirkin's kinetic parameter κ .⁹ This is a dimensionless derived quantity written as:

$$\kappa = k_{fol} d^2 / D \quad \text{Eq. 8-14}$$

It was also empirically shown that:

$$\kappa = 5.608 + 9.347\exp(-7.527/CE) - 7.616\exp(-0.307/CE) \quad \text{Eq. 8-15}$$

where CE is the collection efficiency of the substrate (i_s / i_t). The bottom plot of Figure 8-10 shows Eq. 1-15 as the solid lines for various following reaction rate constants, and the points are derived from Eq. 1-14. As can be seen, the agreement was excellent

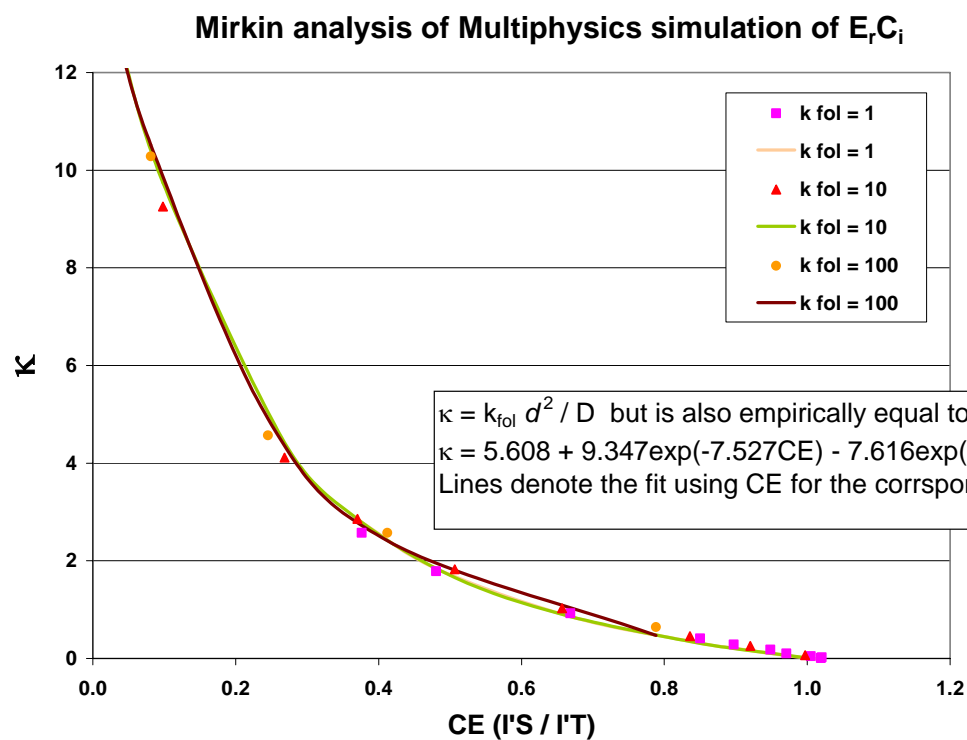
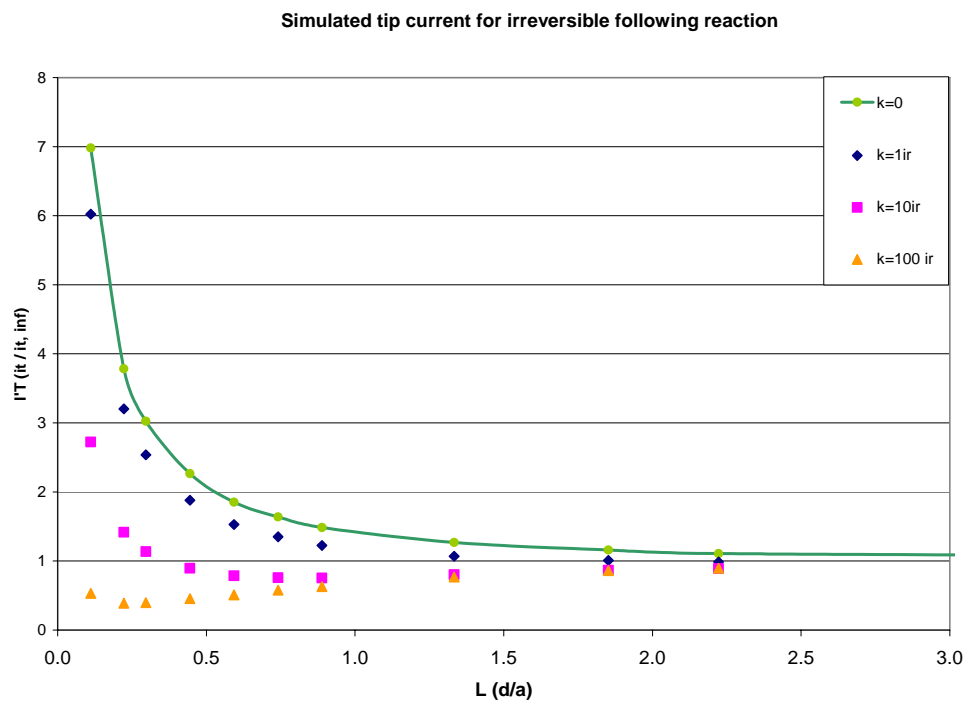


Figure 8-10. Comparison of current model to results for an E_rC_i mechanism to previously published and validated by experimental data by Unwin et al., using Mirkin's dimensionless kinetic parameter κ .

showing Multiphysics was able to model this mechanism, thus improving the confidence in the results for the pseudo first order EC' mechanism.

Fitting of Experimental Data to EC' Predictions

Finally, a comparison of the simulated EC' data to the experimental data of Chapter 7 is shown in Figure 8-11. It shows the simulation compared reasonably well with the experimental data. What is difficult is determining whether the mechanism is EC' or EC_i. Figure 8-12 shows a comparison of predicted substrate and tip responses for the same rate constants but the two different mechanisms. The differences are significant only at small tip/substrate separation. In fact, for the substrate, k values $< 100 \text{ s}^{-1}$ do not generate curve deviations greater than experimental error which is unfortunate since it was hoped to identify the following reaction mechanism for $\text{Ru(phen)}_2\text{dppz}^{2+}$.

Additionally, when reviewing the estimates for rate constants (24 s^{-1} and 360 s^{-1}) for the situation with and without the 20-mer oligomer respectively, the simulation showed rate constants around 10 and one in excess of 100 which compares nicely. However, the situation with DNA is not a first order process since the oligomer is present in fairly small quantities. As was stated in the preceding chapter, when performing the simple time to diffuse calculation, that rate constant did represent the entirety of the process, and therefore provided a reasonable estimate. A second order EC' process is explored both experimentally and through simulation in the next chapter.

Experimental and Simulated substrate collection data for psuedo first order EC'

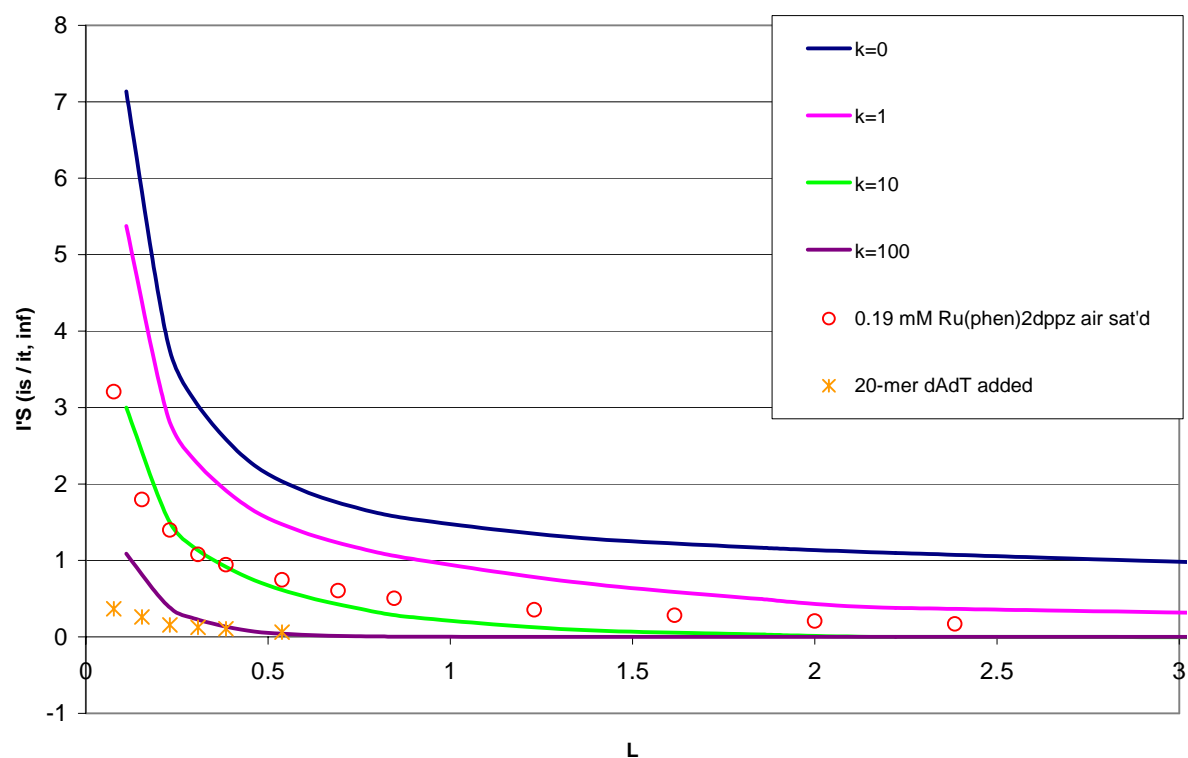
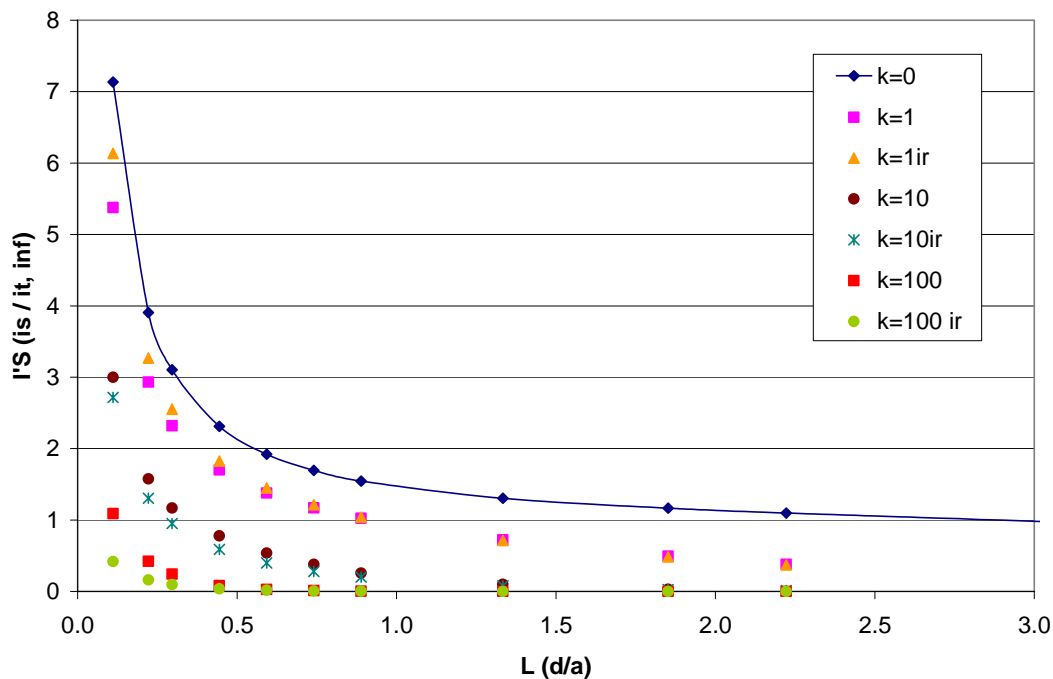


Figure 8-11. Fitting of experimental data to Multiphysics' pseudo first order EC' predictions of normalized substrate current. The data of the free complex agrees well with a rate constant of 10 s^{-1} . The data with 20-mer poly dA-dT added shows a rate constant for that process in excess of 100 s^{-1} .

Simulated substrate current comparing EC' and EC_i mechanisms



Simulated tip current comparing EC' and EC mechanisms

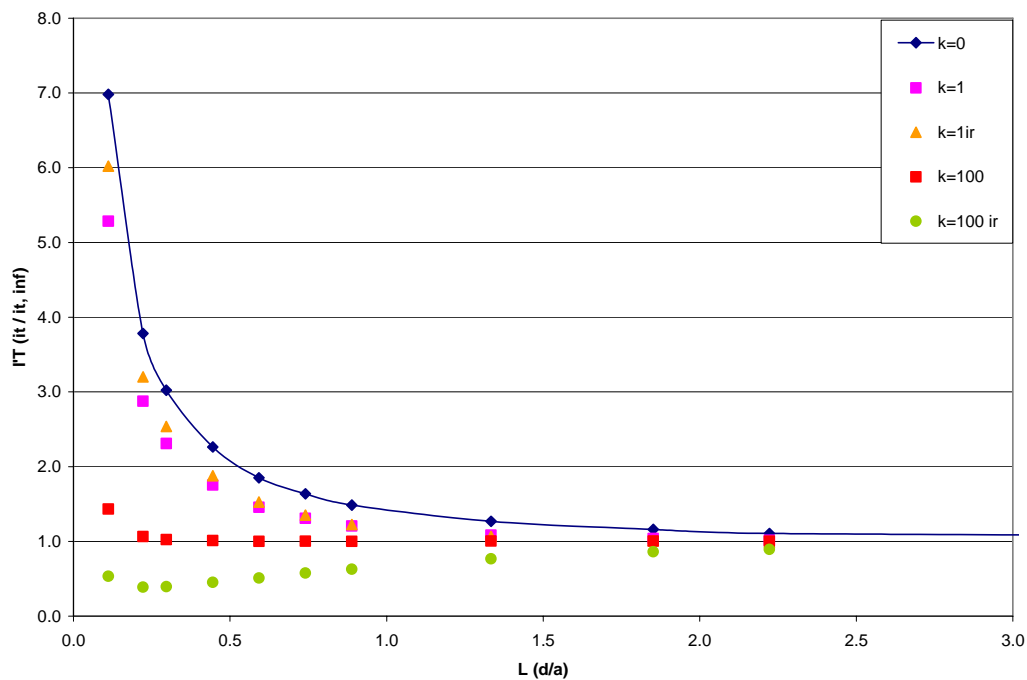


Figure 8-12. A comparison of Multiphysics' predictions for the substrate (top) and tip (bottom) responses for both EC' and EC_i (denoted 'ir') following reaction mechanisms. For the substrate, there is very little difference except at very small tip/substrate separations.

¹ (a) Bard, A., Mirkin, M., Unwin, P., Wipf, D., *J. Phys. Chem.*, **1992**, 96, 1861-1868. (b) Demaille, C., Unwin, P. R., Bard, A., *J. Phys. Chem.*, **1996**, 100, 14137-14143. (c) Martin, R., Unwin, P., *J. Chem. Soc., Faraday Trans.*, **1998**, 94, 753-759.

² (a) Unwin, P., Bard, A., *J. Phys. Chem.*, **1991**, 95, 7814-7824. (b) Zhou, F., Unwin, P., Bard, A., *J. Phys. Chem.*, **1992**, 96, 4917-4924.

³ Rajendran, L., Sanaranarayanan, M., *J. Phys. Chem. B*, **1999**, 103, 1518-1524.

⁴ <http://www.comsol.com/products/multiphysics/>

⁵ <http://www.iupac.org/goldbook/O04322.pdf>

⁶ Bard, A., Faulkner, L., *Electrochemical Methods: Fundamentals and Applications*, 2nd ed., John Wiley & Sons, New York, **2001**, pp. 95-98.

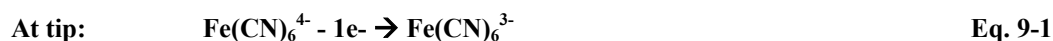
⁷ Bard, A., Mirkin, M., *Scanning Electrochemical Microscopy*, Marcel Dekker, New York, **2001**, p. 6.

⁸ Unwin, P., Bard, A., *J. Phys. Chem.*, **1991**, 95, 7814-7824.

⁹ Treichel, D., Mirkin, M., Bard, A., *J. Phys. Chem.*, **1994**, 98, 5751-5757.

Chapter 9 Simulation Validation

After the work done in Chapter 8 comparing the predictions from Multiphysics to previous, simpler mechanistic systems, a final step was required to complete the validation. This final step was a comparison of Multiphysics' predictions to a known EC' system. Due to its simplicity and aqueous environment, a system of ferrocyanide, $\text{Fe}(\text{CN})_6^{4-}$, with the amino acid cysteine was chosen.¹ This system involves the electrochemical oxidation of the cyanide complex of Fe(II) (ferrous) complex to Fe(III) (ferric). Two ferric complexes then oxidize cysteine to cystine which then dimerizes irreversibly. Additionally, the ferrous/ferric electrode reaction (0.27 V vs. Ag/AgCl) occurs outside the potential window for significant cysteine oxidation (0.8 V vs. SCE)² at the electrode as shown in Figure 9-1, so there should be no significant current from that reaction obscuring the catalytic current of the complex. Also, the reduction of cysteine occurs around 0 V vs. NHE (-0.2 V vs. Ag/AgCl) depending on pH and electrode material³, so the substrate may be held at a potential positive enough to avoid significant rates for that reaction as well. This allowed for an SECM scheme as follows:



It is important to note this system is a bit different than the work in Chapter 8, since it is a second order system. That is, the rate law for the regeneration of Fe^{2+} is:

$$\text{Rate} = k_{EC'} [\text{Fe}(\text{CN})_6^{3-}] [\text{Cys}] \quad \text{Eq. 9-4}$$

Thus, the rate may be varied by varying the cysteine concentration. For this work, based on data from ref 1, the rates used ranged from 0.8 to 5.8 mM/s since the reported rate constant at pH 10 is $8 \times 10^3 \text{ M}^{-1}\text{s}^{-1}$.

Voltammetry

Initially, cyclic voltammograms were conducted with just the complex, and the electroactive radius of the electrode was verified via Eq. 7-2. This radius was modeled into Multiphysics as shown in Chapter 8, and predictions of steady state tip currents at large tip/substrate separations ($> 360 \text{ }\mu\text{m}$) obtained. This distance was deemed adequate based on Eq. 8-9 which predicts a normalized tip current of 1.00 beyond this distance when there is no following reaction. The simulation was repeated for various solutions of constant Fe(II) concentration and increasing cysteine concentration. Then, solutions of the same composition as those simulated were tested, and the steady state currents obtained by both cyclic voltammogram and chronoamperometry (single potential step). The CVs were conducted from 0.1 to 0.45 V vs. Ag/AgCl, 50 mV/s, and the step experiment was done for 8 s at 0.45 V.

It was quickly discovered that, though several hundred mV away from the oxidation and reduction waves, cysteine absorption occurred on the tip electrode surface. This was evidenced by both reproducibility problems and the experimental catalyzed ferrocyanide current falling short of values predicted by Multiphysics when using published data for the second order rate constant. Thus, a method of preparing the electrode prior to voltammetry was required to obtain reliable data. A cleaning step to -1.3 V vs. Ag/AgCl for 20 seconds worked well. This produced both reproducible results between methods and was in good agreement with the simulations as shown in Figure 9-2.

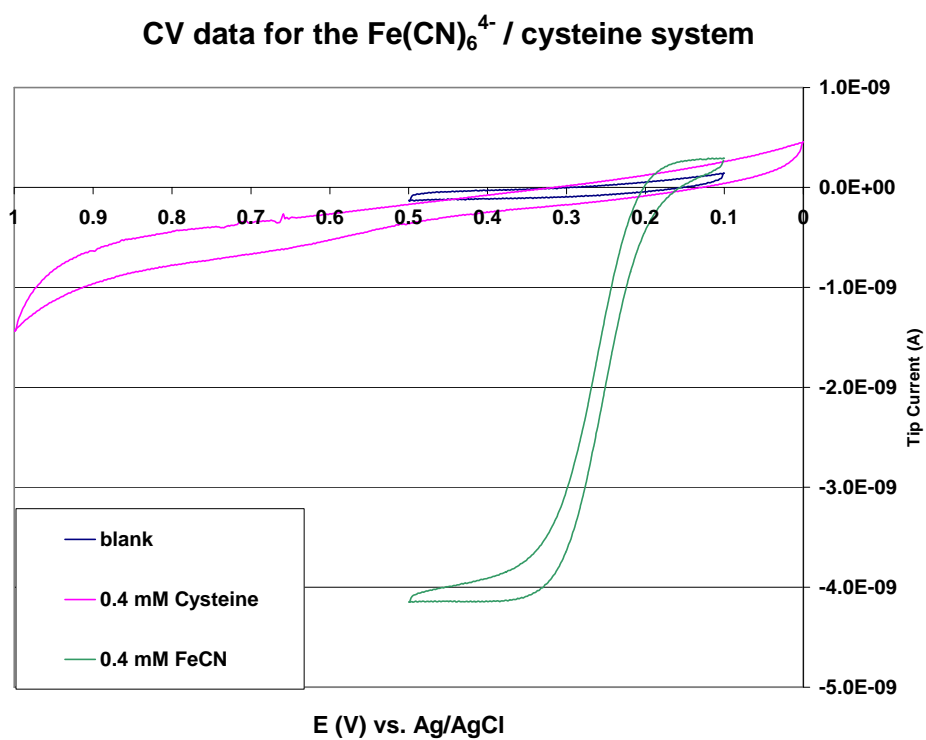


Figure 9-1. Cyclic voltammograms for the various components in the ferrocyanide/cysteine system in a 0.1 M borate, 0.5M KCl buffer at pH 10. Scan rate was 50 mV/s.

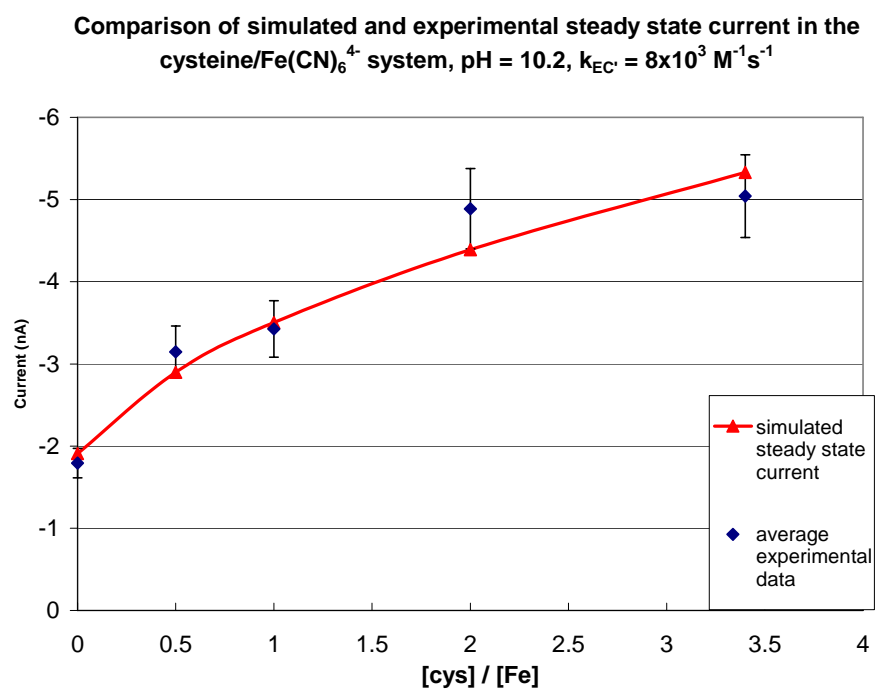


Figure 9-2. A comparison of Multiphysics' simulation of steady state UME tip current and experimental results. The experimental current values are an average of CV and chronoamperometry.

Experimental and Predicted EC' Approach Curves

Next, approach curves with just the ferrocyanide were obtained and fit well to theory for a tip with an RG of 1.5 as shown in Figure 9-3. The collection efficiency also fit well to theory as shown in the bottom plot of Figure 9-3. However, as was previously discussed, electrode fouling was a problem after spending several minutes producing steady state current once cysteine was added. As with the voltammetric data, it yielded approach curves that did not agree well with theory. To solve this problem, an approach was made to substrate contact with just the ferrocyanide to determine how close the tip could be placed. Then the tip was slowly retracted to 30 μm , the cell rinsed, and the solution changed to the equimolar solution. Multiple steps were made back to the substrate, and a CV taken at each distance to obtain the steady state current. Between moves, the cleaning step to -1.3 V was performed, and the data in Figure 9-4 was derived. Replicates were obtained by backing out and repeating the step-wise approach. Reproducibility and agreement was good in the triplicate measurements shown.

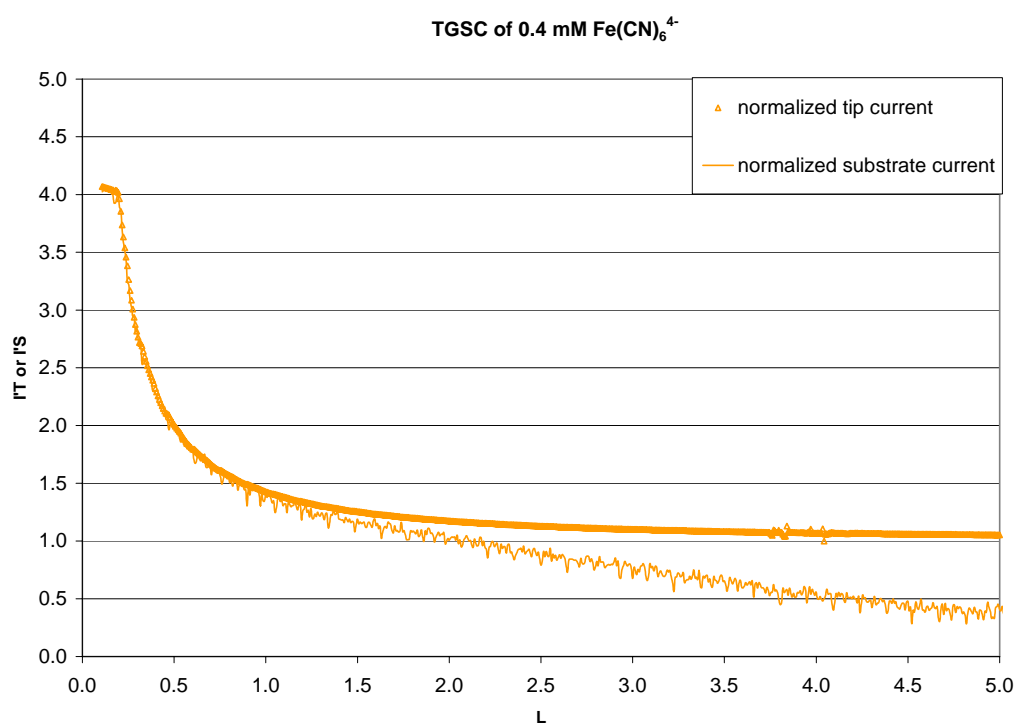
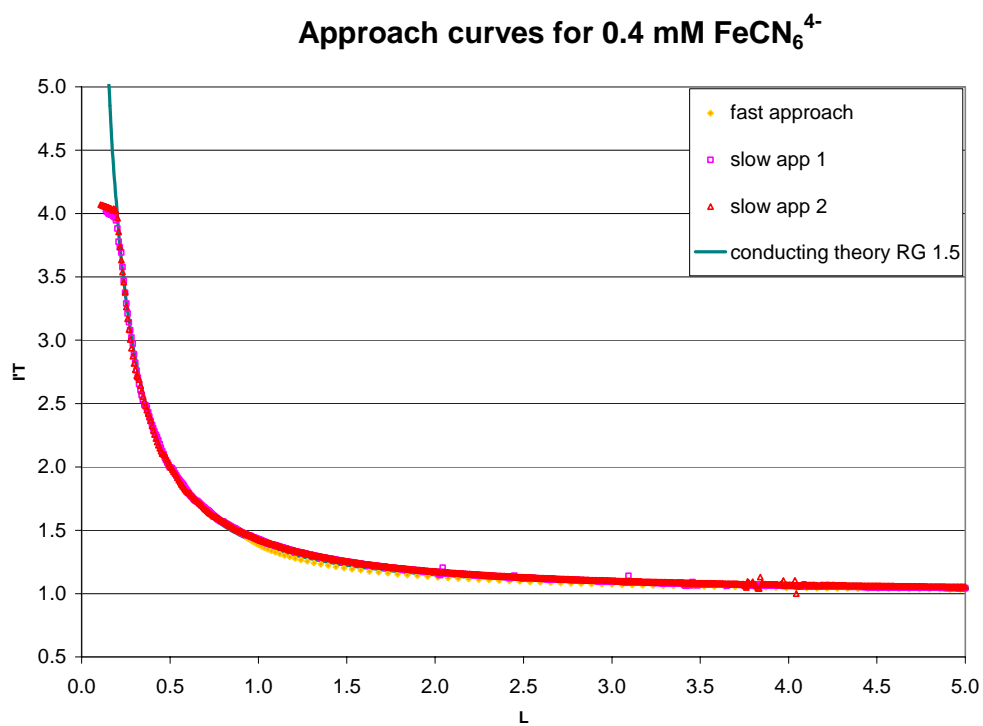


Figure 9-3. Typical tip and substrate responses using the ferro/ferrocyanide couple in a TGSC approach. Approach speed was 0.5 $\mu\text{m/s}$.

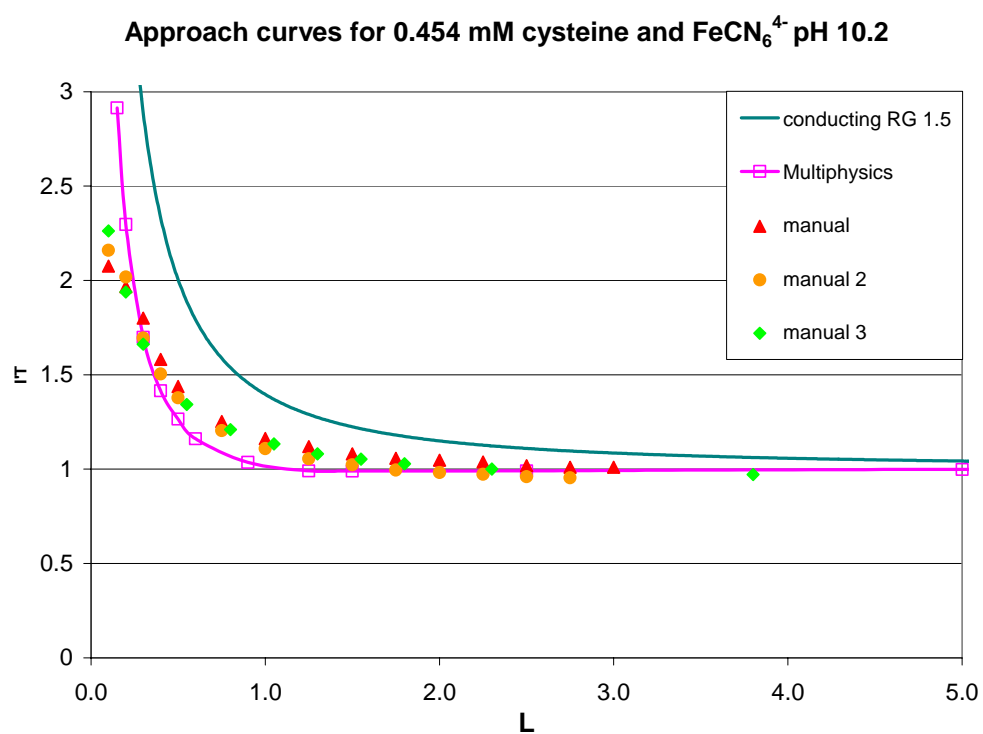


Figure 9-4. Experimental and simulated approach data under the conditions indicated. The rate constant for the second order reaction used the published value at the indicated pH of $8000 \text{ M}^{-1}\text{s}^{-1}$.

¹ Nekrassova, O., Allen, G., Lawrence, N., Jiang, L., Jones, G., Compton, R., *Electroanalysis*, **2002**, *14*, 1464-1469.

² Guo, R., Li, Z., Liu, T., *Coll. Poly. Sci.*, **2004**, *283*, 243-249.

³ Moehl, T., El Halim, A., Tributsch, H., *J. Appl. Electrochem.*, **2006**, *36*, 1341-1346.

Chapter 10 Conclusion

The photoluminescence of $\text{Ru}(\text{phen})_2\text{dppz}^{2+}$ had been studied well prior to the beginning of this work. However, very little electrochemistry and no ECL of this compound had been published. We set out to explore these aspects both as the free complex and intercalated into DNA. While not all aspects of this work were surprising, all have proved to be very interesting.

First, the non-aqueous electrochemistry is straightforward in oxidation and first reduction with potentials of 1.33 V \pm 0.1% vs. SCE (1.57 V vs. NHE) and the E_{red} -0.993 V \pm 0.1% vs. SCE (- 0.753 V vs. NHE). Diffusion coefficients average around $7 \times 10^{-6} \text{ cm}^2/\text{s}$ in acetonitrile and half that in water. Subsequent reduction waves exhibited the same surface absorption as its parent, trisphen, upon reversal. The dppz ligand reduces the energy of the LUMO but still leaves the complex energy sufficient for ECL. Due to the complex's poor solubility ($< 1\text{mM}$), conventional, aqueous electrochemistry is not clearly visible above background water oxidation at a biologically relevant pH.

Since we synthesized the complex in-house, several techniques were used to verify that the product is the target complex and is present in good purity. UV-visible absorption in aqueous buffer showed the previously published bands with extinction coefficients slightly lower than that shown in non-aqueous solvents. Non-aqueous photoluminescence shows a bright orange emitter at 617 nm as is typical of the family and the peak is red shifted from the parent as the electrochemistry would predict. Aqueous PL demonstrated the light-switch effect also at 617 nm upon addition of calf thymus DNA and 20-mer poly dA-dT with binding constants $> 10^6$. However, close inspection showed trace amounts of trisphen present in the mix based on the

peak position before DNA addition. Mass spectrometry verified the trisphen and supports the conclusion that it composes < 1% of the synthetic product.

The aqueous, tripropylamine assisted ECL, while much less intense than others in the family, is significant especially in light of the fact that $\text{Ru(phen)}_2\text{dppz}^{2+*}$ is thoroughly quenched in water when produced via photons. The possibility that trisphen is responsible for the ECL is ruled out since the spectrum of light produced by the synthesized product is red shifted from trisphen (596 nm) to 617 nm like the PL results in acetonitrile. Again, its similarity to the other Ru complexes is consistent in that the ECL spectrum is identical to the PL spectrum. Additionally, the ECL intensity of trisphen at a concentration of 1% of the synthesized product in the same conditions results in 90% less light. The occurrence of ECL in a solvent where PL is quenched indicates that the ECL process interferes with the solvent effect. The uniqueness of the TPrA situation does not end there, however, because when oxalate is used as a co-reactant the ECL is very poor. This may be explained by differences in electrostatic interactions of the electron transfer agents which differ greatly when comparing TPrA to oxalate. The former is uncharged and the latter is anionic.

While the addition of CT DNA and 20-mer poly dA-dT does not decrease the ECL of the complex to the same extent as with trisphen and Os(bpy)_3^{2+} , no light switch behavior is observed. Intercalation lowers the diffusion coefficient which greatly decreases production of the excited state; however, the magnitude of the low ECL efficiency when intercalated, 7% for 20-mer, <1% for CT DNA, cannot be described by diffusion alone. This is demonstrated by the results with 20-mer poly dA-dT which has a diffusion coefficient almost 60% that of the free complex. However, fitting of this data does show the ECL efficiency of the free complex to be on par (near unity) with Ru(bpy)_3^{2+} and Ru(phen)_3^{2+} . Reproducibility was very difficult in

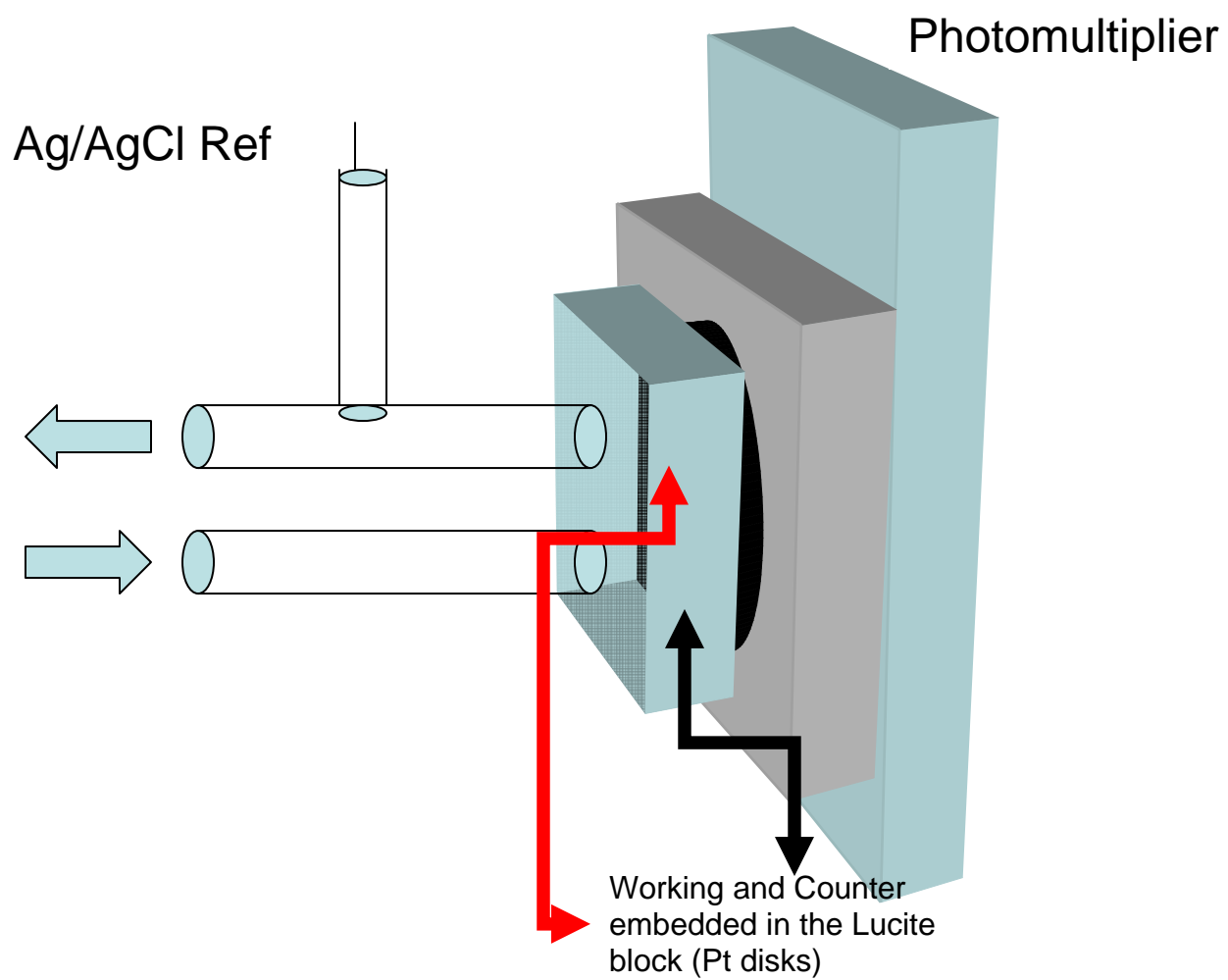
these experiments due to electrode fouling by the DNA and a potential step program called pulsed amperometric detection (PAD) was used to obtain good results.

Scanning electrochemical microscopy was used in an effort to probe the possibility that adenosine or thymine reduce $\text{Ru(phen)}_2\text{dppz}^{3+}$ as guanine has been shown to do with Ru(bpy)_3^{3+} . Since the solubility of the complex is so poor and the potential so positive, only the collected substrate current is visible above the background. When this data was normalized, a following reaction of the free Ru(III) complex was subsequently discovered, though the exact nature and mechanism is still unclear. The software program Multiphysics was used to model the data as an EC' mechanism and the data fit well when using a pseudo first order rate constant of 10 s^{-1} . However, when this simulation is compared to a simulation of the substrate data of an EC_i mechanism, the differences between the two fall within experimental error. Thus substrate current alone is not enough to discern between the two mechanisms. Still, the half wave potential is determined to be 1.21 V vs. Ag/AgCl at a biologically relevant pH in this manner when the other methods had failed. This is the first use of SECM to see processes at the substrate that were not visible at the tip. Additionally, the modeling of the EC' mechanism by digital simulation had not been done previously and the ferrocyanide/cysteine system was successfully used to validate it.

Finally, addition of 20-mer poly dA-dT to the SECM experiment reduced the collected substrate current to background at non-saturating ($R < 12$) amounts. The shift in the half wave potential of Ru(II)/Ru(III) in this experiment showed the Ru(II) to be more strongly intercalated by at least a factor of three. Given the electrode fouling seen in earlier experiments, using a modification of the PAD profile with the SECM software to conduct experiments up to saturating amounts of 20-mer did not improve the collection efficiency. Thus, due to the

previous Pt electrode fouling discussed above, we are unable to definitively say the greatly reduced collection efficiency is due to a following reaction or experimental shortcomings. However, if the data is presumed to show a following reaction with the DNA bases, then the second order rate constant is $> 10^6 \text{ M}^{-1}\text{s}^{-1}$ which is an order of magnitude larger than previously shown for the $\text{Ru}(\text{bpy})_3^{3+}$ /guanine system. This makes sense, though, because $\text{Ru}(\text{phen})_2\text{dppz}^{2+/3+}$ is intercalated as opposed to $\text{Ru}(\text{bpy})_3^{3+}$ which is merely electrostatically bound to the phosphate backbone of the helix.

Appendix A



Appendix B

COMSOL® Multiphysics configuration

SECM Mk2Mod0

1. Table of Contents

- Title - SECM Mk2Mod0
- Table of Contents
- Model Properties
- Constants
- Geometry
- Geom1
- Integration Coupling Variables
- Solver Settings
- Variables

2. Model Properties

| Property | Value |
|----------------|------------------------|
| Model name | SECM Mk2Mod0 |
| Author | Rob Calhoun |
| Company | |
| Department | UT Chemistry |
| Reference | |
| URL | |
| Saved date | Dec 8, 2006 4:52:06 PM |
| Creation date | Dec 7, 2006 1:32:53 PM |
| COMSOL version | COMSOL 3.2.0.304 |

File name: E:\Final dissertation model\Mk2Mod0\Mk2Mod0.mph

Application modes and modules used in this model:

- Geom1 (Axial symmetry (2D))
 - Diffusion (Chemical Engineering Module)

2.1. Model description

Simulates a 13.5 micron (radius) SECM tip over a 1mm electroactive substrate. A following reaction has also been added.

2.2. Model Result

Is a little high compared to previous theory at tip distances inside 2 microns. At memory limits of finer mesh size, this doesn't go away.

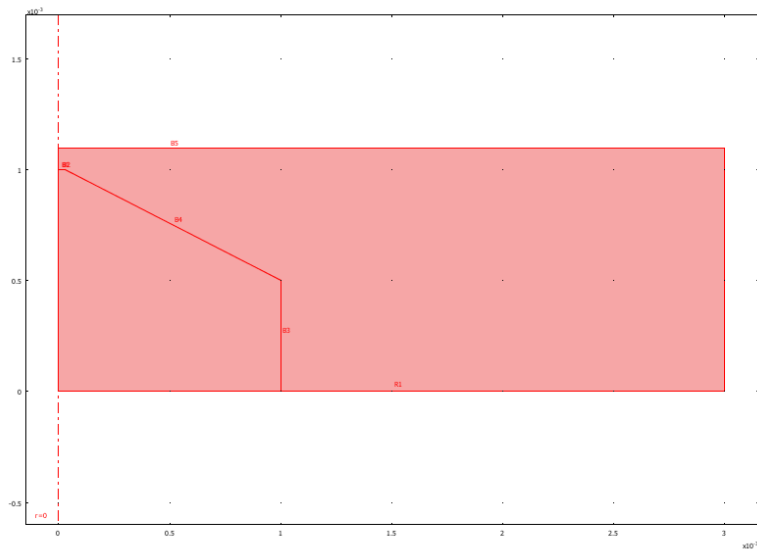
3. Constants

| Name | Expression | Value | Description |
|------|---|------------|----------------------------|
| D2 | 3.5e-10 | 3.5e-10 | Diffusion coefficients |
| D3 | 3.5e-10 | 3.5e-10 | |
| n | 1 | 1 | number of electrons in rxn |
| F | 96485 | 96485 | Faraday |
| kot | 0.01 | 0.01 | hetero rate const tip |
| f | 38.92 | 38.92 | F/RT at Room temp |
| Eo | 1.2 | 1.2 | Ru2+ --> Ru3+ |
| Et | 1.4 | 1.4 | Tip potential |
| nt | Et-Eo | 0.2 | tip overpotential |
| alfa | 0.5 | 0.5 | transfer coefficient |
| kft | $kot \cdot \exp(-alfa \cdot f \cdot nt)$ | 2.04045e-4 | reduction rate at tip |
| kbt | $kot \cdot \exp((1-alfa) \cdot f \cdot nt)$ | 0.490088 | oxidation at tip |
| Es | 1 | 1 | substrate potential |
| ns | Es-Eo | -0.2 | substrate overpotential |
| kfs | $kos \cdot \exp(-alfa \cdot f \cdot ns)$ | 0.490088 | reduction rate at sub |
| kbs | $kos \cdot \exp((1-alfa) \cdot f \cdot ns)$ | 2.04045e-4 | oxidation at sub |
| kos | 0.01 | 0.01 | hetero rate const sub |
| kfol | 1 | 1 | homogeneous rate constant |

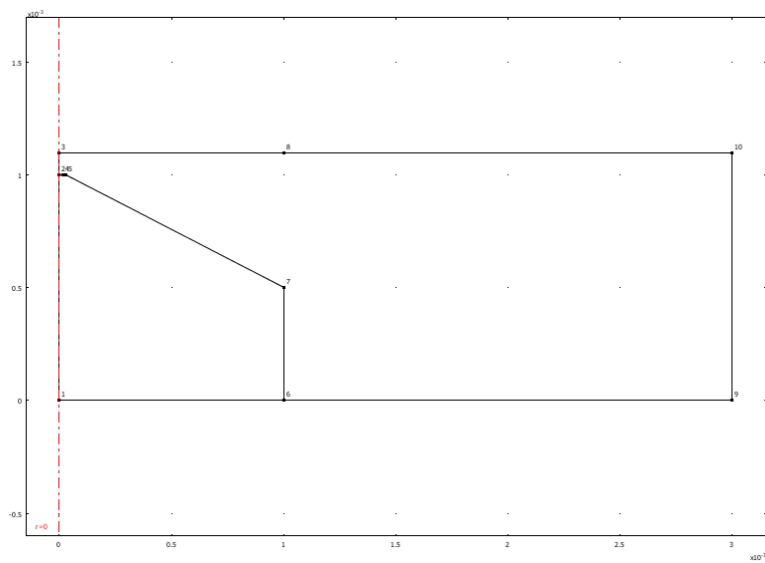
4. Geometry

Number of geometries: 1

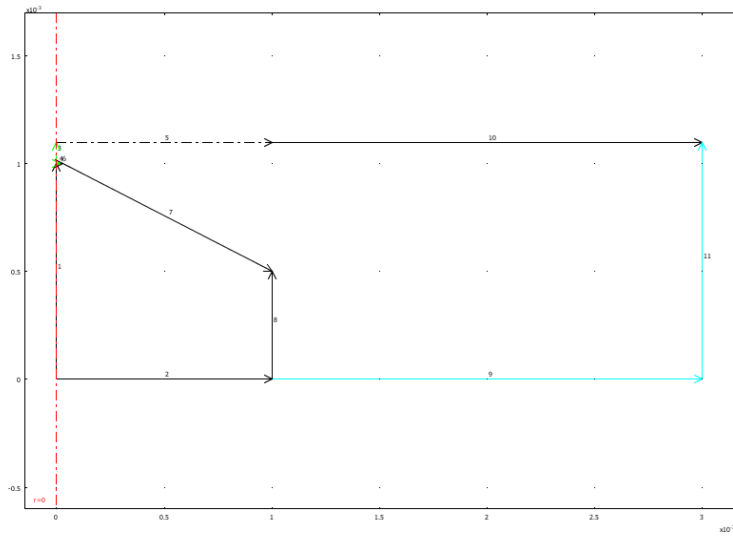
4.1. Geom1



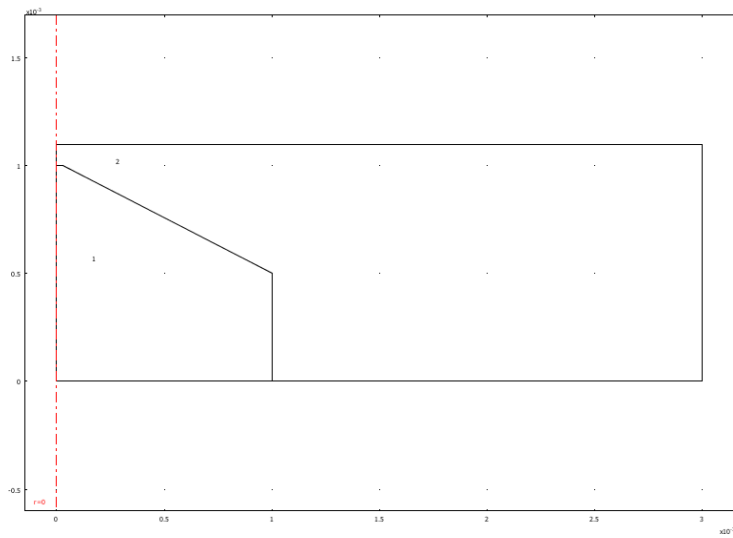
4.1.1. Point mode



4.1.2. Boundary mode



4.1.3. Subdomain mode



5. Geom1

Space dimensions: Axial symmetry (2D)

Independent variables: r, phi, z

5.1. Application Mode: Diffusion (chdi)

Application mode type: Diffusion (Chemical Engineering Module)

Application mode name: chdi

5.1.1. Application Mode Properties

| Property | Value |
|------------------------|----------------------|
| Default element type | Lagrange - Quadratic |
| Analysis type | Stationary |
| Equilibrium assumption | Off |
| Frame | Frame (ref) |
| Weak constraints | Off |

5.1.2. Variables

Dependent variables: Ru2, Ru3

Shape functions: shlag(2,'Ru2'), shlag(2,'Ru3')

Interior boundaries not active

5.1.3. Boundary Settings

| Boundary | | 3 | 4 |
|-------------------------|--|---------------------|---|
| Type | | Axial symmetry | Flux |
| Inward flux (N) | mol/(m ² .s) | {0;0} | {'-((kbt*Ru2)-(kft*Ru3))';'-((kbt*Ru2)-(kft*Ru3))'} |
| Bulk concentration (cb) | mol/m ³ | {0;0} | {0.192;0} |
| Concentration (c0) | mol/m ³ | {0;0} | {0;0.192} |
| Boundary | 5 | 6-8, 10 | 9, 11 |
| Type | Flux | Insulation/Symmetry | Concentration |
| Inward flux (N) | {'((kfs*Ru3)-(kbs*Ru2))';'-((kfs*Ru3)-(kbs*Ru2))'} | {0;0} | {0;0} |
| Bulk | {0.192;0} | {0;0} | {0;0} |

| | | | |
|--------------------|-------|-------|-----------|
| concentration (cb) | | | |
| Concentration (c0) | {0;0} | {0;0} | {0.192;0} |

5.1.4. Subdomain Settings

| | | |
|---------------------------|-------------------------|--------------------------|
| Subdomain | | 2 |
| Diffusion coefficient (D) | m ² /s | {'D2';'D3'} |
| Reaction rate (R) | mol/(m ³ ·s) | {'kfol*Ru3';'-kfol*Ru3'} |

6. Integration Coupling Variables

6.1. Geom1

6.1.1. Source Boundary: 4

| Name | Value |
|-------------------|--------------------|
| Variable name | current |
| Expression | n*F*2*pi*r*D2*Ru2z |
| Order | 4 |
| Global | No |
| Destination Point | 4 (Geom1) |

7. Solver Settings

Solve using a script: off

| | |
|--------------------|----------------|
| Analysis type | Stationary |
| Auto select solver | On |
| Solver | Time dependent |
| Solution form | Automatic |
| Symmetric | Off |
| Adaption | Off |

7.1. Direct (UMFPACK)

Solver type: Linear system solver

| Parameter | Value |
|--------------------------|-------|
| Pivot threshold | 0.1 |
| Memory allocation factor | 0.7 |

7.2. Time Stepping

| Parameter | Value |
|--------------------------|-----------------|
| Times | 0:0.05:8 |
| Relative tolerance | 0.01 |
| Absolute tolerance | 0.0010 |
| Times to store in output | Specified times |

| | |
|--|-------------------|
| Time steps taken by solver | Free |
| Manual tuning of step size | Off |
| Initial time step | 0.0010 |
| Maximum time step | 1.0 |
| Maximum BDF order | 5 |
| Singular mass matrix | Maybe |
| Consistent initialization of DAE systems | Backward Euler |
| Error estimation strategy | Include algebraic |
| Allow complex numbers | Off |

7.3. Advanced

| Parameter | Value |
|--|-------------|
| Constraint handling method | Elimination |
| Null-space function | Automatic |
| Assembly block size | 5000 |
| Use Hermitian transpose of constraint matrix | Off |
| Use complex functions with real input | Off |
| Stop if error due to undefined operation | On |
| Type of scaling | Automatic |
| Manual scaling | |
| Row equilibration | On |
| Manual control of reassembly | Off |
| Load constant | On |
| Constraint constant | On |
| Mass constant | On |
| Damping (mass) constant | On |
| Jacobian constant | On |
| Constraint Jacobian constant | On |

8. Variables

8.1. Boundary

| Name | Description | Expression |
|-----------------|----------------------------|------------|
| ndflux_Ru2_chdi | Normal diffusive flux, Ru2 | |
| ndflux_Ru3_chdi | Normal diffusive flux, Ru3 | |

8.2. Subdomain

| Name | Description | Expression |
|------------------|--|------------|
| grad_Ru2_r_chdi | Concentration gradient, Ru2, r component | |
| dflux_Ru2_r_chdi | Diffusive flux, Ru2, r component | |
| grad_Ru2_z_chdi | Concentration gradient, Ru2, z component | |
| dflux_Ru2_z_chdi | Diffusive flux, Ru2, z component | |
| grad_Ru2_chdi | Concentration gradient, Ru2 | |

| | | |
|------------------|--|--|
| dflux_Ru2_chdi | Diffusive flux, Ru2 | |
| grad_Ru3_r_chdi | Concentration gradient, Ru3, r component | |
| dflux_Ru3_r_chdi | Diffusive flux, Ru3, r component | |
| grad_Ru3_z_chdi | Concentration gradient, Ru3, z component | |
| dflux_Ru3_z_chdi | Diffusive flux, Ru3, z component | |
| grad_Ru3_chdi | Concentration gradient, Ru3 | |
| dflux_Ru3_chdi | Diffusive flux, Ru3 | |

Bibliography

- Amouyal, E.; Homsí, A.; Chambron, J.; Sauvage, J., *J. Chem. Soc. Dalton Trans.*, **1990**, 6, 1841-1844.
- Balzani, V., Juris, A., Barigelletti, F., Campagna, S., Belser, P., Von Zelewsky, A., *Ru(II) Polypyridine Complexes: Photophysics, Photochemistry, Electrochemistry, and Chemiluminescence*, Elsevier Science Publishers, **1988**.
- Bard, A. J., Faulkner, L. R., *Electrochemical Methods: Fundamentals and Applications*, 2nd ed., John Wiley & Sons, New York, **2001**.
- Bard, A. J., Mirkin, M. V., *Scanning Electrochemical Microscopy*, Marcel Dekker, New York, **2001**.
- Bard, A.J., Mirkin, M.V., Unwin, P. R., Wipf, D.O., *J. Phys. Chem.*, **1992**, 96, 1861-1868.
- Barigelletti, F., Juris, A., Balzani, V., Belser, P., von Zelewskylc, A., *Inorg. Chem.*, **1987**, 26, 4115-4119.
- Belser, J., *Hel. Chem. Acta*, **1980**, 63, 1675.
- Berthet, N., Constant, J., Demeunynck, P., Lhomme, J., *J. Med. Chem.*, **1997**, 40, 3346-3352.
- Bi, S., Liu, B., Fan, F., Bard, A. J., *J. Am. Chem. Soc.*, **2005**, 127, 3690-3691.
- Bouchie, A., *Nature Biotech.*, **2003**, 21, 958.
- Brana, M., Cacho, A., Gradillas, A., de Pascual-Teresa, B., Ramos, A., *Curr. Pharm. Des.*, **2001**, 7, 1745-1780.
- Carter, M. T., Bard, A. J., *Bioconj Chem*, **1990**, 2, 257-263.
- Carter, M., Bard, A., *J. Am. Chem. Soc.*, **1987**, 109, 7528-7530.
- Carter, M., Rodriguez, M., Bard, A., *J. Am. Chem. Soc.* **1989**, 111, 8901-8911.
- Delaney, S., Pascaly, M., Bhattacharya, K., Barton, J., *Inorg. Chem.*, **2002**, 41, 1966-1974.
- Demaille, C., Unwin, P. R., Bard, A.J., *J. Phys. Chem.*, **1996**, 100, 14137-14143.
- Dickeson, J.E.; Summers. L. A.; *Aust. J. Chem.*, **1970**, 23, 1023-1027.
- Erikila, K., Odom, D., Barton, J., *Chem. Rev.*, **1999**, 99, 2777-2795.
- Fantacci, S., De Angelis, F., Sgamellotti, A., Marrone, A., Re, N., *J. Am. Chem. Soc.*, **2005**, 127, 14144-14145.
- Faraggi, M., Broitman, F., Trent, J., Klapper, M., *J. Phys. Chem.* **1996**, 100, 14751-14761.
- Fasman, G. D., *CRC Handbook of Biochemistry and Molecular Biology*, 3rd Ed; CRC Press: Boca Raton, FL, 1975; Nucleic Acids Vol 1.
- Fitzsimons, M., Barton, J., *J. Am. Chem. Soc.*, **1997**, 119, 3379-3380

Friedman, A. E.; Chambron, J.; Sauvage, J., Turro, N.J., Barton, J.K., *J. Am. Chem. Soc.*, **1990**, *112*, 4960-4962.

Fukushima, M., Tatsumi, K., Tanaka, S., Nakamura, H., *J. Environ. Sci. Tech.*, **1998**, *32*, 3948-3953.

Garcia-Campana, A., Baeyens, G., *Chemiluminescence in Analytical Chemistry*, Marcel Dekker, New York, **2001**.

Guo, R., Li, Z., Liu, T., *Coll. Poly. Sci.*, **2004**, *283*, 243-249.

Harris, D.C., *J. Chem. Ed.*, **1998**, *75*, 119-121.

Hartshorn, R., Barton, J., *J. Am. Chem. Soc.*, **1992**, *114*, 5919-5925.

Hercules, D., Lytle, F., *J. Am. Chem. Soc.*, **1966**, *88*, 4745.

Hiort, C., Lincoln, P., Norden, B., *J. Am. Chem. Soc.*, **1993**, *115*, 3448-3454.

[http://en.wikipedia.org/wiki/Intercalation_\(chemistry\)](http://en.wikipedia.org/wiki/Intercalation_(chemistry))

<http://users.rcn.com/jkimball.ma.ultranet/BiologyPages/D/DoubleHelix.html>

<http://www.bioveris.com/technology/technology-why.htm>

http://www.blc.arizona.edu/Molecular_Graphics/DNA_Structure/DNA_Tutorial.HTML#Purine

<http://www.comsol.com/products/multiphysics/>

<http://www.iupac.org/goldbook/O04322.pdf>

Hughes, S., Meschi, P. L., Johnson, D. C., *Anal. Chim. Acta*, **1981**, *132*, 1-10.

Johnson, D. C., LaCourse, W. R., *Anal. Chem.*, **1990**, *62*, 589A – 597A.

Johnston, D., Thorp, H., *J. Phys. Chem.*, **1996**, *100*, 13837-13843.

Kanoufi, F., Bard, A. J., *J. Phys. Chem. B*, **1999**, *103*, 10469-10480.

Kanoufi, F., Zu, Y., Bard, A., *J. Phys. Chem. B*, **2001**, *105*, 210-216.

Kinoshita, K., *Electrochemical Oxygen Technology*, John Wiley & Sons, New York, **1992**.

Knight, A., Greenway, G., *Analyst*, **1994**, *119*, 879-890.

Liu, Y., Bhouai, A., Degtyareva, N., Lutterman, D. A., Dunbar, K., Turro, C., *J. Am. Chem. Soc.*, **2005**, *127*, 10796-10797.

Martin, R.D., Unwin, P. R., *J. Chem. Soc., Faraday Trans.*, **1998**, *94*, 753-759.

Martinez, R., Chacon-Garcia, L., *Curr. Med. Chem.*, **2005**, *12*, 127-151.

Maruyama, T., Takata, T., Ichinose, H., Kamiya, N., Kuma, H., Hamasaki, N., Morita, H., Goto, M., *Biotechnol. Prog.*, **2005**, *21*, 575-579.

Matsumoto, Y., Terui, N., Tanaka, S., *Environ. Sci. Tech.*, **2006**, *40*, 4240-4244.

Miao, W., Choi, J., Bard, A., *J. Am. Chem. Soc.*, **2002**, *124*, 14478-14485.

Mihailovic, A., Vladescu, I., McCauley, M., Ly, E., Williams, M. C., Spain, E. M., Nunez, M. E., *Langmuir*, **2006**, *22*, 4699-4709.

Moehl, T., El Halim, A., Tributsch, H., *J. Appl. Electrochem.*, **2006**, *36*, 1341-1346.

Muench, K., *Genetic Medicine*, Elsevier, New York, **1988**.

Murphy, J., Arkin, M., Ghatlia, N., Bossmann, S., Turro, N., Barton, J., *Proc. Natl. Acad. Sci. USA*, *91*, 5315-5319, June 1994.

Nekrassova, O., Allen, G., Lawrence, N., Jiang, L., Jones, G., Compton, R., *Electroanalysis*, **2002**, *14*, 1464-1469.

Noffsinger, J., Danielson, N., *Anal. Chem.*, **1987**, *59*, 865-868.

Okamoto, K., Miyawaki, J., Nagai, K., Matsumura, D., Nojima, A., Yokoyama, T., Kondoh, H., Ohta, T., *Inorg. Chem.*, **2003**, *42*, 8682-8689.

Olofsson, J., Wilhelmsson, L. M., Lincoln, P., *J. Am. Chem. Soc.*, **2004**, *126*, 15458-15465.

Olofsson, J.; Onfelt, B.; Lincoln, P., *J. Phys. Chem. A*, **2004**, *108*, 4291-4398.

Olson, E.J.C.; Hu, D.; Hormann, A.; Honkman, A.M.; Arkin, M.R.; Stemp, E.D.A.; Barton, J. K.; Barbara, P. F., *J. Am. Chem. Soc.*, **1997**, *119*, 11458-11467.

Onfelt, B., Lincoln, P., Norden, B., *J. Am. Chem. Soc.*, **2001**, *123*, 3630-3637.

Parker, C.A., *Photoluminescence of Solutions*, Elsevier Publishing, **1968**.

Petitjean, A., Barton, J., *J. Am. Chem. Soc.*, **2004**, *126*, 14728-14729.

Pezeshk, A., Symons, M., McClymont, J., *J. Phys. Chem.*, **1996**, *100*, 18562-18566.

Rajendran, L., Sanaranarayanan, M., *J. Phys. Chem. B*, **1999**, *103*, 1518-1524.

Rodriguez, M., Bard, A. J., *Anal. Chem.*, **1990**, *62*, 2658-2662.

Rubenstein, I., Bard, A.J., *J. Am. Chem. Soc.*, **1981**, *103*, 512-516.

Schatzschneider, U., Barton, J., *J. Am. Chem. Soc.*, **2004**, *126*, 8630-8631.

Sistare, M., Holmberg, R., Thorp, H., *J. Phys. Chem. B*, **1999**, *103*, 10718-10728.

Sprintschnik, G.; Sprintschnik, H.; Kirsch, P. P.; Whitten, D.G., *J. Am. Chem. Soc.*, **1977**, *99*, 4947-4954.

Sullivan, B. P.; Salmon, D. J.; Meyer, T.J., *Inorg. Chem.*, **1978**, *17*, 3334-3341.

Testa, A., Reinmuth, W., *Anal. Chem.*, **1961**, *33*, 1320-1324.

Tokel, N., Bard, A., *J. Am. Chem. Soc.*, **1972**, *94*, 2862-2863.

Tokel-Takvoryan, N., Hemingway, R., Bard, A., *J. Am. Chem. Soc.*, **1973**, *95*, 6582-6589.

Treichel, D., Mirkin, M., Bard, A., *J. Phys. Chem.*, **1994**, *98*, 5751-5757.

Tse, W., Boger, D., *Acc. Chem. Res.*, **2004**, *37*, 61-69.

Turro, C., Bossmann, S., Jenkins, Y., Barton, J., Turro, N., *J. Am. Chem. Soc.*, **1995**, *117*, 9026-9032.

Unwin, P.R., Bard, A.J., *J. Phys. Chem.*, **1991**, *95*, 7814-7824.

Velasco, J., *Electroanalysis*, **1991**, *3*, 261-271.

Waldemar, A., Cilento, G., *Chemical and Biological Generation of Excited States*, Academic Press Inc., 1982; p. 193.

Wang, G., Zhang, J., Murray, R., *Anal. Chem.*, **2002**, *74*, 4320-4327.

Welch, T.W., Corbett, A. H., Thorp, H. H., *J. Phys. Chem.*, **1995**, *100*, 11757-11763.

Wong, E., Gooding, J., *Anal. Chem.*, **2003**, *75*, 3845-3852.

Yagi, M., Sukegawa, N., Kaneko, M., *J. Phys. Chem. B.*, **2000**, *104*, 4111-4114.

Yamada, H., Koike, T., Hurst, J., *J. Am. Chem. Soc.* **2001**, *123*, 12775-12780.

Yoo, J., Delaney, E., Stemp, D., Barton, J., *J. Am. Chem. Soc.*, **2003**, *125*, 6640-6641.

Zhou, F., Unwin, P.R., Bard, A.J., *J. Phys. Chem.*, **1992**, *96*, 4917-4924.

Zong, R., Thummel, R., *J. Am. Chem. Soc.* **2005**, *127*, 12802-12803

Zoski, C., *Electroanalysis*, **2002**, *14*, 1041-1051.

Zu, Y., Bard, A.J., *Anal. Chem.*, **2000**, *72*, 3223-3232.

Vita

Commander Robert L. Calhoun, USN, was an honor graduate of El Dorado High School, El Dorado, Arkansas in 1983. He graduated from the United States Naval Academy, Annapolis, MD, with distinction in 1987 and earned a Bachelor of Science degree in Chemistry.

Upon commissioning as an Ensign, CDR Calhoun proceeded to the Navy's flight school in Pensacola, FL, and earned his wings as a Naval Aviator in 1988 at Naval Air Station Corpus Christi, TX. After serving two years as a flight instructor in the T-34C 'Turbomenter', he proceeded to Patrol Squadron THIRTY for training in the P-3C 'Orion'. His operational flying tours were in Patrol Squadrons EIGHT and TWENTY-SIX, both in Brunswick, ME. Non-flying tours were as a catapult officer aboard USS *Dwight D. Eisenhower*, CVN-69, and as Director, Tactical Support Center, Keflavik, Iceland.

Between tours on 'Ike' and with the Tridents of VP-26, he earned a Master of Science degree in physical chemistry from Auburn University, Alabama, under the direction of Dr. Jimmy Mills. This was funded by the Navy's Civilian Institutions program and published work on photo-reductions of chlorofluorocarbons using titanium dioxide in the *Journal of Physical Chemistry A and B*.

During his tour in Iceland, CDR Calhoun was chosen to enter the Navy's Permanent Military Professor program, which has funded his Ph.D. studies in electroanalytical chemistry at the University of Texas, Austin, TX. Upon successful completion of degree requirements, he will be appointed an associate professor of

chemistry at the United States Naval Academy where he will continue to serve until retirement from the Navy.

Permanent Address: 906 Tanglewood Dr., Leander, TX 78641

This dissertation was typed by the author